Politecnico di Milano

Department of Aerospace Science and Technology
Master of Science in Space Engineering

Ballistic Capture Sets and orbits evolution under variations of the capture epoch

Author:
Emiliano La Paglia
ID 919866

Supervisor:
Prof. Francesco Topputo
Co-advisor:
Gianmario Merisio

Academic Year 2020/2021

Abstract

Master of Science in Space Engineering

Ballistic Capture Sets and orbits evolution under variations of the capture epoch

by Emiliano La Paglia

Over the last decades a new wave in space exploration has risen: small satellites such as CubeSats are more and more opening the possibility to smaller companies to reach the orbital environment. Within the Horizon 2020 programme the EXTREMA project ongoing at Politecnico di Milano aims at proving that miniaturized satellites are fully capable of autonomously navigating the deep-space environment. In particular, the main structure of the mission is divided into three main pillars, one of which focuses on the ballistic capture phenomenon and how it can be exploited to achieve low-energy and low-cost injection into the martian gravitational field. Such pillar has been at the basis of this thesis: the ballistic Capture Sets and orbits evolution under the variation of the capture epoch has been extensively investigated. Robustness and sensitivity of target arrival date and spacecraft state at its first close encounter with the red planet have been assessed.

Sommario

Master of Science in Space Engineering

Ballistic Capture Sets and orbits evolution under variations of the capture epoch

by Emiliano La Paglia

Nelle ultime decadi una nuova modalità nell'esplorare lo spazio ha guadagnato popolarità: piccoli satelliti come i CubeSats stanno sempre più aprendo la possibilità a piccole compagnie di navigare nello spazio. All'interno del programma Horizon 2020 il progetto EXTREMA in corso al Politecnico di Milano si pone lo scopo di dimostrare che questi satelliti miniaturizzati siano in grado di navigare lo spazio profondo in maniera completamente autonoma. In particolare, lo scheletro di questa missione è diviso in tre pilastri principali, uno dei quali affronta il tema della cattura graviatazionale e di come questa possa essere sfruttata per raggiungere a basso costo il campo gravitazionale marziano. Questo pilastro rappresenta il punto di partenza di questa tesi: l'evoluzione dei Capture Sets e delle relative orbite è stato ampiamente studiato all'interno di un modello ad alta fedeltà. Sono infatti state oggetto di investigazione la robustezza e la sensitività della data di arrivo selezionata e dello stato del satellite al suo primo passaggio ravvicinato del pianeta rosso.

Acknowledgments

L'aver raggiunto questo obbiettivo non rappresenta solo un momento di gioia e soddisfazione, ma anche di gratitudine verso coloro che mi hanno guidato e accompagnato durante il cammino verso questo giorno. Il primo ringraziamento va al Politecnico di Milano presso il quale si conclude oggi questo capitolo della mia vita, non solo di crescita accademica ma anche e soprattutto personale. Voglio inoltre ringraziare il Prof. Francesco Topputo e Gianmario Merisio per la guida, la disponibilità e l'aiuto che mi hanno fornito durante lo svolgimento della mia tesi di laurea.

Il ringraziamento più grande va alla mia famiglia. Ringrazio i miei genitori per aver reso possibile il raggiungimento di questo traguardo. Li ringrazio per il sostegno economico e soprattutto morale che è servito a portare a termine questo percorso. Li ringrazio per aver sopportato i miei sbalzi di umore da giorni di tranquillità a giorni di stress incontenibile. Li ringrazio per avermi lasciato monopolizzare il soggiorno negli ultimi due anni, dovendo rinunciare al comfort di guardare la televisione seduti sul divano di casa.
Un doveroso ed enorme ringraziamento va poi a mio fratello Ivano, che nonostante gli impegni prima accademici e poi lavorativi ha sempre trovato un po' di tempo per darmi retta ed aiutarmi a superare i mille ostacoli che si sono presentati durante questo percorso. Lo ringrazio per i suoi preziosi consigli e per la sua enorme pazienza.

Voglio poi ringraziare i miei amici di Decadentismo Alcolico con cui ho condiviso una marea di momenti divertenti ed indimenticabili. Ore ed ore di risate e ricordi che non si dimenticano facilmente. Ringrazio Catta per i mille consigli che mi ha offerto nel corso di quasi dodici anni, lo ringrazio per aver sopportato i miei sfoghi pomeridiani discussi al computer e per avermi consigliato e supportato nei momenti difficili. Ringrazio Rufus per il suo supporto psicologico durante questi anni passati all'università. L'aver avuto qualcuno con cui condividere gli insulti quotidiani ai codici di Matlab che non funzionavano è stato molto confortante. Ringrazio Robbi per l'essere una fonte inesauribile di materiale comico che mi porterò come ricordo per sempre. Ringrazio Marze per i mille meme e per la sua dispobilità nel cercare di organizzare gite in montagna. Ringrazio Bomba per le serate passate da lui, per le grigliate e per le risate (la vacanza di Barcellona ed il coltello dello chef non sono cose che si possono dimenticare). Ringrazio Gabri per le serate passate a dire idiozie e per i passaggi in macchina di ritorno da queste. Ringrazio Murghi per l'aver coniato il nome di questo strampalato gruppo di individui che si ritrovano spesso a bere insieme e a dire stupidaggini. Ringrazio infine Sean e Kiro che, nonostate le volte in cui risciamo a vederci siano poche, trovano sempre il modo di aggiungere valore alle serate condivise.

Un ultimo ringraziamento va infine ai compagni di corso con cui ho condiviso questo percorso accademico, persone con cui ho condiviso la quotidianità delle lezioni e gli scleri degli esami.

Milano, 7/10/2021

Emiliano

Contents

List of Figures

List of Tables

List of Symbols

A	—	Effective area
a	—	Semi-major axis
C_R	—	Reflectivity coefficient
c	—	Speed of light
e	—	Eccentricity
f	—	True anomaly
H	—	Kepler energy
i	—	Inclination
LU	—	Length unit
L_S	—	Luminosity of the Sun
MU	—	Gravity Unit
m	—	Mass
R	—	Mean equatorial radius of the target celestial body
R_{SOI}	—	Radius of the Sphere of Influence
TU	—	Time Unit
U_{NSG}	—	Non-Spherical Gravity field potential function
VU	—	Velocity Unit
λ	—	Geographic longitude
μ	—	Mass parameter
μ_i	—	Gravitational constant of the generic i-th celestial body
Φ	—	State Transition Matrix
ϕ	—	Geocentric latitude
φ	—	Flow map
Ω	—	Right ascension of the ascending node
ω	—	Argument of periapsis
$\mathcal{C}$	—	Capture Set
$\mathcal{D}$	—	Acrobatic Set
$\mathcal{E}$	—	Escape Set
$\mathcal{G}$	—	Generic Set
$\mathcal{I}$	—	Impact Set
$\mathcal{J}$	—	Inject Set
$\mathcal{K}$	—	Crash Set
$\mathcal{L}$	—	Land Set
$\mathcal{M}$	—	Moon Crash Set
$\mathcal{R}$	—	Region of interest
$\mathcal{R}_\mathcal{C}$	—	Capture Ratio
$\mathcal{S}$	—	Stability Index
$\overline{\mathcal{S}}$	—	Regularity Coefficient
$\tilde{\mathcal{S}}$	—	Normalized Stability Index

$\mathcal{W}$	—	Weakly Stable Set
$\mathcal{X}$	—	Unstable Set
$\mathbf{a}$	—	Acceleration vector
$\mathbf{a}_{SRP}$	—	Solar Radiation Pressure acceleration
$\mathbf{f}$	—	Velocity map
$\mathbf{r}$	—	Position vector
$\mathbf{v}$	—	Velocity vector
$\mathbf{x}$	—	State vector
$\mathbf{0}_{n\times n}$	—	Null matrix of size n
$\mathbf{I}_{n\times n}$	—	Identity matrix of size n
$\mathbf{Q}_{f\rightarrow i}$	—	Target-fixed to inertial reference frame transformation matrix

List of Abbreviations

2D	—	Two-dimensional
3D	—	Three-dimensional
CG	—	Cauchy-Green
CR3BP	—	Circular Restricted 3-Body Problem
DU	—	Dimensionless Unit
EME2000	—	Earth Mean Equator and Equinox of J2000
EPHE	—	Full Ephemerides Model
ER3BP	—	Elliptic Restricted 3-Body Problem
ESA	—	European Space Agency
GRAIL	—	Gravity Recovery and Interior Laboratory
GRATIS	—	GRAvity TIdal Slide toolbox
IC	—	Initial Condition
ICRF	—	International Celestial Reference Frame
LCS	—	Lagrangian Coherent Structure
MATLAB	—	Matrix Laboratory
MJD2000	—	Modified Julian Day since J2000
NASA	—	National Aeronautics and Space Administration
NSG	—	Non-Spherical Gravity
ODE	—	Ordinary Differential Equation
RPF	—	Roto-Pulsating Frame
RTN@t_0	—	Radial-Tangential-Normal frame at epoch t_0
SI	—	International System of Units (Systéme International d'unités)
SOI	—	Sphere of Influence
SRP	—	Solar Radiation Pressure
STM	—	State Transition Matrix
TDB	—	Barycentric Dynamic Time (Temps Dynamique Baricentrique)
VSVO	—	Variable Stepsize Variable Order
WSB	—	Weak Stability Boundary

Chapter 1

Introduction

In astrodynamics, the trajectory design process aims at finding a solution that satisfies a given set of constraints whilst optimizing one or more parameters. The objective is often defined as the minimization of the cost associated with the mission at hand, which translates into the minimization of the propellant mass required for the trajectory.
In the early stages of space exploration, trajectories were designed accounting for the use of high-thrust engines able to provide quasi-instantaneous changes in velocity - and therefore also in orbit. Over the last few decades instead, new approaches have been developed: low-energy transfers have started to rise as a viable option for interplanetary trajectories. Amongst this last category, it is possible to find the phenomenon of the ballistic capture, sometimes referred to as gravitational capture.

1.1 Historical Context

In 1991, Japan placed two satellites in Earth orbit: Hagoromo, which was supposed to achieve lunar orbit, and Hiten. During the journey to the Moon, contacts with Hagoromo were lost and without any knowledge on the state of the spacecraft, the Japanese decided to send Hiten to the Moon. However, Hiten was designed to serve as a relay satellite for communications between Hagoromo and the Earth, therefore lacking a sufficient amount of propellant to complete a lunar transfer through the traditional Hohmann strategy. To overcome this issue scientists started looking for a different way to get Hiten to the Moon. In particular, they started investigating trajectories that exploited the gravitational fields of the Moon, the Earth and the Sun, allowing for a small propellant requirement. Such *ballistic* trajectories were found through numerical simulations and Hiten was able to achieve lunar orbit using only 3 out of the 7 kg of propellant that the spacecraft was provided with. However, the transfer resulted in a 150 days long journey, a value significantly larger than the 3 days required for a traditional Hohmann transfer [6]. A comparison between a ballistic capture trajectory and a traditional Hohmann transfer is depicted in Figure 1.1.

The success of the japanese satellite marked a new milestone in space exploration: since Hiten, more missions have looked for and applied ballistic capture trajectories, including the first ESA's mission to the Moon, SMART-1, launched in 2003, and NASA's mission to map the lunar gravity field, GRAIL, launched in 2011. The concept of ballistic capture has also been considered in the early stages of the development of the ESA's mission to Mercury, Bepi-Colombo [15].

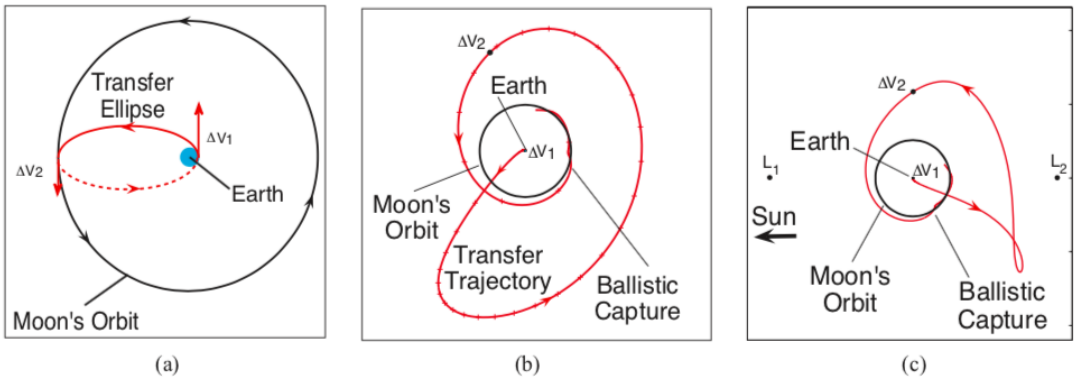

Figure 1.1: Hohmann transfer (a). Ballistic capture in inertial (b) and rotating frame (c), respectively [16].

1.2 Motivation and Objectives

In the last decade, research in the field of miniaturized satellites has grown significantly: this has opened the possibility to smaller companies to develop and fly their own satellites. However, the smaller scale of such spacecraft implies the necessity of introducing low-energy transport systems, among which the ballistic capture phenomenon can be found. In this context, the EXTREMA project, ongoing at Politecnico di Milano within the Horizon 2020 programme, aims at proving that such miniaturized probes are fully capable to navigate autonomously in deep-space. The project exploits the ballistic capture phenomenon around Mars to prove that miniaturized spacecraft can perform autonomous tasks also in complex scenarios.

The ballistic capture phenomenon represents a very interesting possibility in the trajectory design process due to its advantages with respect to traditional patched conics transfers. Among the upsides of such ballistic capture trajectories there are:

- reduction of the propellant mass required for the injection burn;
- removal of single point failure associated with the traditional hyperbolic insertion;
- wider launch windows due to the intrinsic nature of the phenomenon considered.

Due to their advantages, ballistic capture transfers are more frequently being considered in the design process, leading to the necessity of better understanding the *robustness* of the chosen trajectory. In particular, it is worth analysing how variations in the time frame considered can affect the resulting transfer and answering the following research question:

How do particular portions of a Capture Set evolve under the influence of variations in the capture epoch?

The focus will therefore be only on a small region of the Capture Set: the neighbourhood of the most regular trajectories will be extensively analysed.

1.3 Work Summary and Structure

Whilst answering the research question represents the final milestone of this study, during the developed work also an in-depth analysis of previously achieved results has been performed. The early stages of this thesis extensively covered the physics behind the gravitational capture phenomenon. Subsequently, the work focused on understanding how particular mathematical

tools could be adapted to the problem at hand and developing models that were later tested on the case study in order to finally answer the proposed research question.

The present work is organised as follows:

- Chapter 2 will cover the theoretical background necessary to understand and study the ballistic capture phenomenon;
- Chapter 3 will give an in-depth physical and dynamical description of the ballistic capture phenomenon;
- Chapter 4 will describe the workflow and the methodology followed throughout this document;
- Chapter 5 will present the results obtained;
- Chapter 6 will summarise the conclusions reached in the present thesis, underlining areas in which future developments appear desirable.

Chapter 2

Background

In this chapter, an in-depth description of the ideas at the basis of the phenomenon at hand will be given through the definition of the reference frames used, the equations of motion, the variational equations characterizing the problem and the mathematical background of Lagrangian Coherent Structures.

2.1 Reference Frames

2.1.1 Earth Mean Equator and Equinox of J2000

In order to introduce this reference frame, it is mandatory to define what J2000 represents: it is the time epoch corresponding to 12:00 at Greenwhich on January 1^{st} 2000, Barycentric Dynamic Time (TDB). It is now possible to define the Earth Mean Equator and Equinox of J2000 (EME2000) inertial reference frame, shown in Figure 2.1:

- the positive x-axis (x_e) points at the mean equinox at J2000;
- the positive z-axis (z_e) points at the celestial North Pole;
- the positive y-axis (y_e) completes the dextral orthonormal triad.

This reference frame, although being defined through the Earth's equator and equinox, is not necessarily centered at the Earth.
In the present work, the ephemerides are assumed to be defined in this reference frame. However, a more rigorous definition would involve the use of the International Celestial Reference Frame (ICRF), which presents infinitesimal discrepancies with the EME2000 frame[4].

2.1.2 Radial-Tangential-Normal

In literature, ballistic capture has mainly been studied using reference frames connected with the orbit of the target body and its position along the orbit itself. The Radial-Tangential-Normal frame at epoch t_0 (RNT@t_0), centred at the target body as shown in Figure 2.1, is defined such that [17]:

- the positive z-axis (z_r) is orthogonal to the orbital plane;
- the positive x-axis (x_r) is aligned with the Sun-planet line, pointing from the Sun to the planet;
- the positive y-axis (y_r) completes the dextral orthonormal triad.

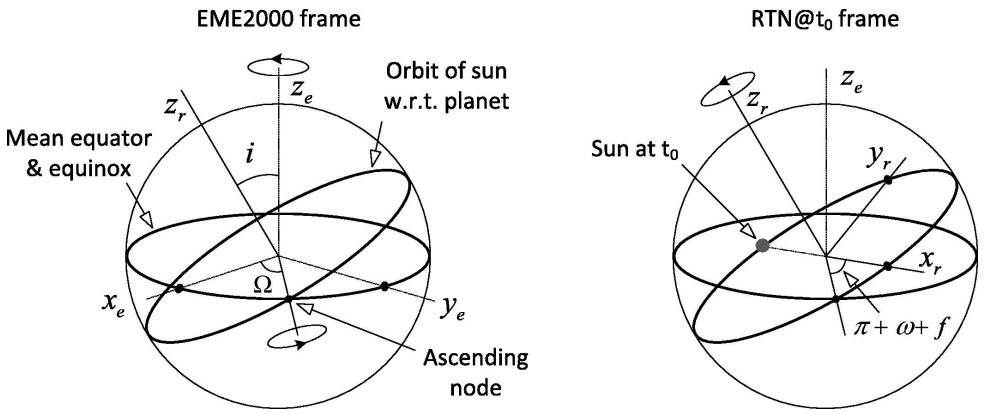

Figure 2.1: EME2000 and RTN@t_0 reference frames [17].

The transformation from the RNT@t_0 reference frame to the EME2000 one is given by [17]

$$\begin{pmatrix} x_e \\ y_e \\ z_e \end{pmatrix} = \begin{bmatrix} \sin\theta\sin\Omega\cos i - \cos\theta\cos\Omega & \sin\theta\cos\Omega + \cos\theta\sin\Omega\cos i & \sin\Omega\sin i \\ -\cos\theta\sin\Omega - \sin\theta\cos\Omega\cos i & \sin\theta\sin\Omega - \cos\theta\cos\Omega\cos i & -\cos\Omega\sin i \\ -\sin\theta\sin i & -\cos\theta\sin i & \cos i \end{bmatrix} \begin{pmatrix} x_r \\ y_r \\ z_r \end{pmatrix} \tag{2.1}$$

with $\theta = \omega + f$, where i, Ω, ω and f represent inclination, right ascension of the ascending node, argument of periapsis and true anomaly of the Sun in the EME2000 frame, respectively.

2.1.3 Roto-Pulsating Frame

Another useful reference frame is the Roto-Pulsating Frame (RPF). It is defined in the Circular Restricted 3-Body Problem (discussed in Section 2.2.1) such that both primaries are at rest on the x-axis, in particular:

- the positive x-axis is directed from the largest primary to the target one;
- the positive z-axis is aligned with their orbital angular momentum vector;
- the positive y-axis completes the dextral orthonormal triad.

Since the two primaries are at rest, their position within this frame is intrinsically defined: the largest sits at $x = -\mu$, whilst the target lays at $x = 1 - \mu$, with

$$\mu = \frac{m_2}{m_1 + m_2}$$

being the mass parameter of the Sun-target system. This reference frame will be used in Section 3.1 when introducing the concept of Weak Stability Boundary and the definition of *stable* and *unstable* trajectories, as well as during the exposition of some results in Chapter 5.

2.2 Equations of Motion

2.2.1 Circular Restricted 3-Body Problem

Due to the nature of the phenomenon, ballistic capture trajectories cannot be found in the context of the 2-Body problem of the Keplerian dynamics: at least two major gravitational fields must be considered to observe a particle undergoing ballistic capture. The simplest non-Keplerian model that allows to compute ballistic capture trajectories is the Circular Restricted 3-Body Problem (CR3BP), where a particle with negligible mass is influenced by the gravitational fields of two main bodies (also referred to as *primaries*) cycling about the centre of mass

of the system on circular orbits.
In the EME2000 reference frame centred at the target planet, the motion of the particle is described by the following second-order differential equation [17]

$$\ddot{\mathbf{r}} + \frac{\mu_t}{r^3}\mathbf{r} + \mu_s \left(\frac{\mathbf{r}_s}{r_s^3} + \frac{\mathbf{r} - \mathbf{r}_s}{\|\mathbf{r} - \mathbf{r}_s\|^3} \right) = 0 \tag{2.2}$$

with

$$\mathbf{r}_s(t) = -a \begin{pmatrix} \sin\theta \sin\Omega \cos i - \cos\theta \cos\Omega \\ -\cos\theta \sin\Omega - \sin\theta \cos\Omega \cos i \\ -\sin\theta \sin i \end{pmatrix} \tag{2.3}$$

where a is the target's planet orbital semi-major axis.
In Equation 2.2:

- $\mathbf{r}$ and $\mathbf{r}_s$ are the position vectors of the particle and the Sun, respectively;
- r and r_s are the magnitudes of the respective position vectors;
- μ and μ_t are the gravitational constants of the target and the Sun, respectively.

A graphical representation of the framework depicted by the CR3BP is reported in Figure 2.2.

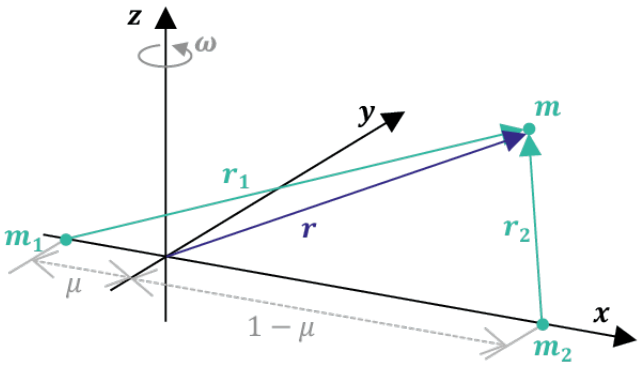

Figure 2.2: CR3BP: m_1 and m_2 are the Sun and the target planet, respectively [31].

The CR3BP will be used later in Chapter 3 to introduce the concept of Weak Stability Boundary and its connection with the Lagrange Points.

2.2.2 Elliptic Restricted 3-Body Problem

The Elliptic Restricted 3-Body Problem (ER3BP) is a model where also the eccentricity of the orbit of the target planet is considered. The motion of the particle is still described by Equation 2.2, however, in order to account for the planetary eccentricity Equation 2.3 has to be modified and becomes [17]

$$\mathbf{r}_s(t) = -\frac{a(1-e^2)}{1 + e\cos f(t)} \begin{pmatrix} \sin\theta \sin\Omega \cos i - \cos\theta \cos\Omega \\ -\cos\theta \sin\Omega - \sin\theta \cos\Omega \cos i \\ -\sin\theta \sin i \end{pmatrix} \tag{2.4}$$

where e and f are the target planet's orbital eccentricity and true anomaly, respectively. It is trivial to verify that by setting $e = 0$ the formulation of the CR3BP is restored. The ER3BP represents an intermediate step between the simple representation offered by the CR3BP and

the more complex Full Ephemerides Model. For non-negligible values of eccentricity, the circular model approximates in a very poor manner the real trajectory of the particle, whereas the elliptical one represents a good approximation of the real dynamical behaviour [17].

2.2.3 Full Ephemerides Model

A more comprehensive dynamical environment is represented by a model accounting for the gravitational fields of all the main bodies in the Solar System: the Full Ephemerides Model (EPHE). The dynamical behaviour of the particle within this framework is described by [17]

$$\ddot{\mathbf{r}} + \frac{\mu_t}{r^3}\mathbf{r} + \mu_s \left(\frac{\mathbf{r}_s}{r_s^3} + \frac{\mathbf{r} - \mathbf{r}_s}{\|\mathbf{r} - \mathbf{r}_s\|^3} \right) = -\sum_{i \in \mathbb{P}} \mu_i \left(\frac{\mathbf{r}_i}{r_i^3} + \frac{\mathbf{r} - \mathbf{r}_i}{\|\mathbf{r} - \mathbf{r}_i\|^3} \right) \tag{2.5}$$

where $\mathbb{P}$ is the set containing the perturbing bodies, which in this work includes all the planets in the Solar System except for the target one. In this framework, the states of the Sun and of the perturbing bodies are extracted from NASA's SPICE toolkit [1, 2]. A graphical representation of the EPHE model is depicted in Figure 2.3.

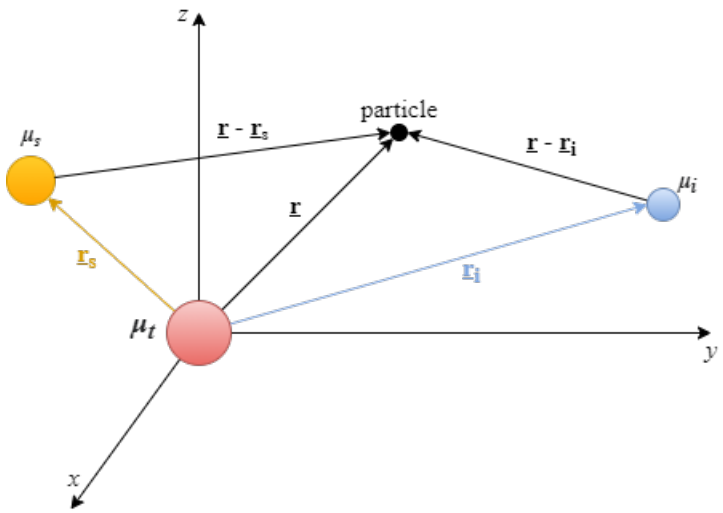

Figure 2.3: EPHE: μ_t, μ_s and μ_i are the target, the Sun and the i-th planet, respectively.

It is trivial to verify that by setting $\mathbb{P} = \varnothing$ the equations of motion of the ER3BP model are obtained.

2.2.4 Orbital Perturbations

A more accurate high-fidelity model that can be used to describe any gravitational phenomenon is one accounting for all possible orbital perturbations, such as Solar Radiation Pressure and a Non-Spherical Gravity model of the target body in addition to the complete set of gravitational fields already accounted for in the EPHE model. Such complete model would result in the following equations of motion for the particle [21]

$$\ddot{\mathbf{r}} + \frac{\mu_t}{r^3}\mathbf{r} + \mu_s \left(\frac{\mathbf{r}_s}{r_s^3} + \frac{\mathbf{r} - \mathbf{r}_s}{\|\mathbf{r} - \mathbf{r}_s\|^3} \right) = \mathbf{a}_{SRP} - \mathbf{Q}_{f \to i} \nabla U_{NSG} - \sum_{i \in \mathbb{P}} \mu_i \left(\frac{\mathbf{r}_i}{r_i^3} + \frac{\mathbf{r} - \mathbf{r}_i}{\|\mathbf{r} - \mathbf{r}_i\|^3} \right) \tag{2.6}$$

where:

- U_{NSG} is a potential function describing the geometry of the target's gravity field;
- Q_{NSG} is the transformation matrix relating the planet-fixed reference frame (in which the potential function U_{NSG} is defined) to the inertial one of the equations of motion;
- $\mathbf{f}_{SRP}$ is the acceleration vector due to the Solar Radiation Pressure.

Although the dynamical model used in the present work does not account for the Non-Spherical Gravity term appearing in Equation 2.6, the expression of both SRP and NSG perturbations is now given.

Solar Radiation Pressure

In Equation 2.6, the effect of the Solar Radiation Pressure (SRP) is represented by the term [21]

$$\mathbf{a}_{SRP} = \frac{C_R L_S}{4\pi c} \frac{A}{m} \frac{\mathbf{r} - \mathbf{r}_s}{\|\mathbf{r} - \mathbf{r}_s\|^3} \tag{2.7}$$

where:

- L_S is the luminosity of the Sun;
- c is the speed of light;
- C_R is the reflectivity coefficient of the particle;
- A is the effective area of the particle;
- m is the mass of the particle;
- $\mathbf{r}$ and $\mathbf{r}_s$ are the position vectors of the particle and Sun, respectively.

In the present work the effective area A has been considered constant and independent of the attitude orientation of the particle: this hypothesis is what constitutes the *cannonball* model.

Non Spherical Gravity

In Equation 2.6, the effect of the Non-Spherical Gravity (NSG) of the target's gravitational field is expressed through the use of the potential U_{NSG}. An approximation of this function can be obtained using a spherical harmonics expansion [21]

$$U = -\frac{\mu_t}{r}\left[1 + \sum_{n=2}^{\infty}\sum_{m=0}^{n}\left(\frac{R}{r}\right)^n P_{n,m}\sin\phi(C_{n,m}\cos m\lambda + S_{n,m}\sin m\lambda)\right] \tag{2.8}$$

with

$$P_n(x) = \frac{1}{(-2)^n n!}\frac{\mathrm{d}^n}{\mathrm{d}x^n}(1-x^2)^n \quad \text{and} \quad P_{n,m} = (1-x^2)^{m/2}\frac{\mathrm{d}^m}{\mathrm{d}x^m}P_n(x) \tag{2.9}$$

where:

- R is the target's reference radius;
- r is the distance of the particle from the target's centre of mass;
- μ_t is the target's gravitational parameter;
- ϕ is the geocentric latitude;
- λ is the geographic longitude;
- $C_{n,m}$ and $S_{n,m}$ are numerical coefficients.

It is worth highlighting that the spherical coordinates (ϕ,λ) are defined in a target-fixed reference frame centred at its centre of mass, which is the reason why the transformation matrix $Q_{f\to i}$ had to be introduced in Equation 2.6.

It is now possible to write the potential function describing the non-spherical gravity field as

$$U_{NSG} = U + \frac{\mu}{r} \tag{2.10}$$

2.3 Variational Equations

Once the dynamical model and the reference frame are defined, the motion of the particle can be described as

$$\begin{cases} \dot{\mathbf{x}}(t) = \mathbf{f}(\mathbf{x}, t) \\ \mathbf{x}(t_0) = \mathbf{x}_0 \end{cases} \tag{2.11}$$

with $\mathbf{x}(t) \in \Omega \subseteq \mathbb{R}^6$ being the state vector of the system. It is immediate to notice that Equation 2.11 is a first-order differential equation (also called *velocity map*). In Section 2.2 the dynamics of the system is described by a second-order differential equation: the transformation to a first-order one implies doubling the number of independent variables of the system. It is also worth highlighting the direct dependence on time ($\mathbf{f}$ explicitly depends on t) because of the intrinsic nature of the (perturbed) restricted n-Body problem at hand: the system is therefore non-autonomous.
Integrating Equation 2.11 allows to compute the *flow map* of the system

$$\begin{aligned} \varphi_{t_0}^t : \Omega &\mapsto \Omega \\ \mathbf{x}_0 &\mapsto \varphi_{t0}^t(\mathbf{x}_0) = \mathbf{x}(t; t_0, \mathbf{x}_0) \end{aligned} \tag{2.12}$$

returning the state at time t for each initial state $\mathbf{x}_0$ and initial time t_0.
From the expression of the flow map it is now possible to define the *State Transition Matrix* (STM) of the system as

$$\Phi := \Phi(t; t_0, \mathbf{x}_0) = D_{\mathbf{x}_0}\varphi_{t_0}^t(\mathbf{x}_0) = D_{\mathbf{x}_0}\mathbf{x}(t; t_0, \mathbf{x}_0) \tag{2.13}$$

which can be propagated through

$$\begin{cases} \dot{\Phi} = D_{\mathbf{x}}\mathbf{f}(\mathbf{x}, t)\Phi = \mathbf{A}(\mathbf{x}, t)\Phi \\ \Phi(t_0; t_0, \mathbf{x}_0) = \mathbf{I}_{n\times n} \end{cases} \tag{2.14}$$

where D is a differential operator, $\mathbf{A}$ is the Jacobian of the velocity map and $\mathbf{I}_{n\times n}$ is the identity matrix of size n. It is worth noticing that Equation 2.14 features the term $\mathbf{A}(\mathbf{x}(t), t) = D_{\mathbf{x}}\mathbf{f}(\mathbf{x}(t), t)$ which depends on $\mathbf{x}(t)$, the instantaneous state vector of the system. Because of this dependence, the integration of Equation 2.14 requires the simultaneous propagation of the dynamics of the state described in Equation 2.11. The joint system characterized by $n^2 + n$ independent variables constitutes what is referred to as *variational equations*.

2.3.1 Analytical derivatives of the velocity map

When referring to dynamical systems, it is worth remembering that the representation of the state is not unique: there is in fact an infinite set of equivalent formulations. In the context analysed throughout the current section, a cartesian representation has been chosen, such that

$$\mathbf{x}(t) = \begin{pmatrix} \mathbf{r}(t) \\ \mathbf{v}(t) \end{pmatrix} = \begin{pmatrix} \mathbf{r}(t) \\ \dot{\mathbf{r}}(t) \end{pmatrix} \qquad \text{and} \qquad \dot{\mathbf{x}}(t) = \mathbf{f}(\mathbf{x}, t) = \begin{pmatrix} \mathbf{v}(t) \\ \mathbf{a}(\mathbf{r}, \mathbf{v}, t) \end{pmatrix} = \begin{pmatrix} \dot{\mathbf{r}}(t) \\ \ddot{\mathbf{r}}(\mathbf{r}, t) \end{pmatrix}$$

As previously mentioned, the term $\mathbf{A}(\mathbf{x}(t), t)$ represents the Jacobian of the velocity

$$\mathbf{A}(\mathbf{x}, t) = D_{\mathbf{x}}\mathbf{f}(\mathbf{x}, t) = \frac{\partial \mathbf{f}(\mathbf{x}, t)}{\partial \mathbf{x}(t)} \tag{2.15}$$

Making use of the representation chosen, it is possible to further analyse such Jacobian

$$\frac{\partial \mathbf{f}(\mathbf{x}, t)}{\partial \mathbf{x}(t)} = \begin{bmatrix} \dfrac{\partial \mathbf{v}(t)}{\partial \mathbf{r}(t)} & \dfrac{\partial \mathbf{v}(t)}{\partial \mathbf{v}(t)} \\ \dfrac{\partial \mathbf{a}(\mathbf{r}, \mathbf{v}, t)}{\partial \mathbf{r}(t)} & \dfrac{\partial \mathbf{a}(\mathbf{r}, \mathbf{v}, t)}{\partial \mathbf{v}(t)} \end{bmatrix}_{6\times 6} = \begin{bmatrix} \mathbf{0}_{3\times 3} & \mathbf{I}_{3\times 3} \\ \dfrac{\partial \ddot{\mathbf{r}}(\mathbf{r}, t)}{\partial \mathbf{r}(t)} & \dfrac{\partial \ddot{\mathbf{r}}(\mathbf{r}, t)}{\partial \dot{\mathbf{r}}(t)} \end{bmatrix}_{6\times 6} \tag{2.16}$$

where $\mathbf{0}_{3\times 3}$ and $\mathbf{I}_{3\times 3}$ are the null and identity matrices of size 3, respectively. By recalling the expression of the acceleration which the particle is subjected to (given in Section 2.2), it is easy to notice that $\ddot{\mathbf{r}}(\mathbf{r}, t)$ does not depend on the velocity. This in turn means that

$$\frac{\partial \ddot{\mathbf{r}}(\mathbf{r}, t)}{\partial \dot{\mathbf{r}}(t)} = \mathbf{0}_{3\times 3}$$

and therefore

$$\mathbf{A}(\mathbf{x}, t) = \frac{\partial \mathbf{f}(\mathbf{x}, t)}{\partial \mathbf{x}(t)} = \begin{bmatrix} \mathbf{0}_{3\times 3} & \mathbf{I}_{3\times 3} \\ \dfrac{\partial \ddot{\mathbf{r}}(\mathbf{r}, t)}{\partial \mathbf{r}(t)} & \mathbf{0}_{3\times 3} \end{bmatrix}_{6\times 6} \tag{2.17}$$

To obtain the Jacobian of the velocity field is therefore necessary to compute only one term, whose analytical expression will follow [22]. It is however worth recalling that the expression of the acceleration given in Section 2.2 featured many different terms, each associated to its source. To ease the reading and understanding of the work, each component will be treated individually. For the sake of completeness, the analytical derivative of the term associated with the NSG component is provided in Appendix A.

Central Body gravitational field

The most important contribution to the Variational Equations arises from the term associated with the gravity field of the target body. When considering the gravity field as ideally spherical the expression of the partial derivative is given by

$$\left(\frac{\partial \ddot{\mathbf{r}}}{\partial \mathbf{r}}\right)_{SG} = -\mu_t \left(\frac{1}{r^3}\mathbf{I}_{3\times 3} - 3\mathbf{r}\frac{\mathbf{r}^T}{r^5}\right) \tag{2.18}$$

where the subscript SG stands for "Spherical Gravity" and the term $\mathbf{r}\mathbf{r}^T$ represents the dyadic product, which results in a 3×3 matrix and should not be confused with the dot product $\mathbf{r}^T\mathbf{r}$.

When the NSG component of the gravity field of the central body is accounted for, the expression of the partial derivative is different. In a body-centred frame the expression of the derivative assumes the following form

$$\left(\frac{\partial \ddot{\mathbf{r}}}{\partial \mathbf{r}}\right)_{NSG} = \sum_{n,m} \frac{\partial \ddot{\mathbf{r}}_{nm}}{\partial \mathbf{r}} \tag{2.19}$$

The analytical expression of the right hand side of Equation 2.19 in given in Appendix A.

Third Body perturbations

Since the framework at hand is that of the restricted n-Body problem, there are $n-2$ additional gravitational fields influencing the motion of the particle. Although the formulation presented in Section 2.2.3 would suggest a distinction between the contribution due to the Sun and those due to the planets, in reality they are all of the same nature and are therefore here referred to as *third body perturbations*. The partial derivative of the acceleration generated by these perturbations is given by

$$\left(\frac{\partial \ddot{\mathbf{r}}}{\partial \mathbf{r}}\right)_{3B} = -\sum_{i \in \mathbb{P}} \mu_i \left(\frac{1}{\|\mathbf{r} - \mathbf{r}_i\|^3} \mathbf{I}_{3\times 3} - 3(\mathbf{r} - \mathbf{r}_i) \frac{(\mathbf{r} - \mathbf{r}_i)^T}{\|\mathbf{r} - \mathbf{r}_i\|^5} \right) \tag{2.20}$$

Solar Radiation Pressure perturbation

The last term to analyse is the component of the acceleration due to the SRP. Recalling the model used in Section 2.2.4 to describe this force, the expression of the partial derivative assumes the following form

$$\left(\frac{\partial \ddot{\mathbf{r}}}{\partial \mathbf{r}}\right)_{SRP} = \frac{C_R L_S}{4\pi c} \frac{A}{m} \left(\frac{1}{\|\mathbf{r} - \mathbf{r}_s\|^3} \mathbf{I}_{3\times 3} - 3(\mathbf{r} - \mathbf{r}_s) \frac{(\mathbf{r} - \mathbf{r}_s)^T}{\|\mathbf{r} - \mathbf{r}_s\|^5} \right) \tag{2.21}$$

It is therefore now possible to compute the Jacobian $\mathbf{A}(\mathbf{x}, t)$ of the velocity field in Equation 2.17, since

$$\frac{\partial \ddot{\mathbf{r}}(\mathbf{r}, t)}{\partial \mathbf{r}(t)} = \left(\frac{\partial \ddot{\mathbf{r}}}{\partial \mathbf{r}}\right)_{SG} + \left(\frac{\partial \ddot{\mathbf{r}}}{\partial \mathbf{r}}\right)_{3B} + \left(\frac{\partial \ddot{\mathbf{r}}}{\partial \mathbf{r}}\right)_{SRP} \tag{2.22}$$

2.3.2 Cauchy-Green Strain Tensor

Having a complete description of the State Transition Matrix and its computation, the Finite-time Cauchy-Green (CG) Strain Tensor can now be introduced

$$\Delta(T, \mathbf{x}_0, t_0) := \Phi^T(t_0 + T; \mathbf{x}_0, t_0) \cdot \Phi(t_0 + T; \mathbf{x}_0, t_0) \tag{2.23}$$

This mathematical construct allows to quantify the relative stretching of nearby trajectories for a given time interval, as shown in Figure 2.4. By definition, the CG tensor Δ is symmetric and positive definite and therefore characterized by n real positive eigenvalues. This tensor will be used when discussing Lagrangian Coherent Structures in Section 2.4: in fact, its eigenstructure is a powerful tool in the study of underlying behaviours of dynamical systems.

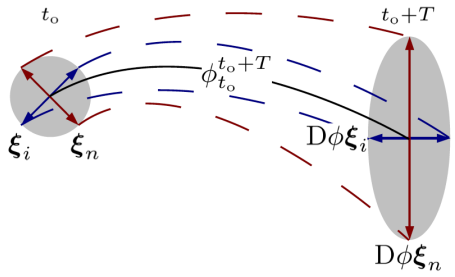

Figure 2.4: Stretching associated with eigenvectors of the Cauchy-Green Tensor [28].

2.3.3 Sensitivity to changes in the initial epoch

At the core of the present work there is the question about what influence does the initial epoch have in the resulting trajectory of the particle. It is therefore important to define the derivative of the flow map with respect to the initial epoch t_0, given by [11]

$$\frac{\mathrm{d}\varphi_{t_0}^{t}}{\mathrm{d}t_0} = -\Phi(t;\mathbf{x}_0,t_0)\mathbf{f}(\mathbf{x}_0,t_0) \tag{2.24}$$

At the basis of this expression lies the idea that for sufficiently small variations, a perturbation in the initial epoch δt_0 can be mapped as a perturbation in the initial state vector $\delta\mathbf{x}_0$, as shown in Figure 2.5.

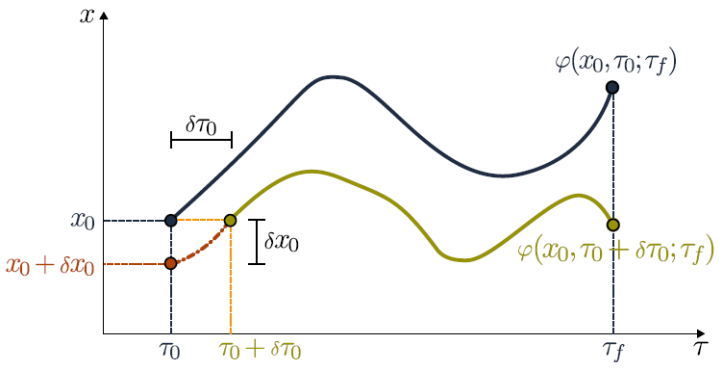

Figure 2.5: Representation of the initial flow projection [11].

2.4 Lagrangian Coherent Structures

A particular mathematical tool suited to study complex nonlinear and non-autonomous dynamical systems is represented by *Lagrangian Coherent Structures* (LCS) [21, 27]. Here the word *Lagrangian* highlights the evolution of such structures in the state space throughout time, as opposed to the Eulerian specification of the flow.
As will be discussed in Section 3.1, the dynamical behaviour of autonomous systems can be qualitatively described by considering equilibrium points and invariant manifolds. In complex non-autonomous systems like the one represented by the restricted n-Body problem, such manifolds cannot be defined: *Coherent Structures* are an attempt at generalizing this concept to "systems with arbitrary time dependence" [26].

2.4.1 Poincaré and Stroboscopic maps

Within the mathematics of dynamical systems a powerful construct is represented by the *Poincaré map* (also called *first recurrence map*). Such tool is obtained by intersecting the flow with a lower-dimensional surface transversal to the flow called Poincaré section. A schematic representation of this concept is reported in Figure 2.6.

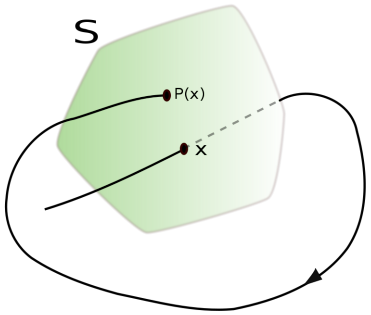

Figure 2.6: Poincaré map P transforms x into $P(x)$ onto the Poincaré section S.[1]

A particular type of Poincaré map that can be defined when studying non-autonomous periodic dynamical systems (with period T) is the *Stroboscopic map*, where the state of the system is studied in intervals of T time units.

2.4.2 LCS Definition and Classification

The following formal definition of Lagrangian Coherent Structures is given:

- LCS are *material surfaces* in that they have sufficient dimension to visibly impact the dynamics of the system and move coupled with the flow (as suggested by "Lagrangian");
- LCS are *locally* characterized by the strongest attraction, repulsion or shear in the flow.

LCS can also be classified following the same rationale used when analysing invariant manifolds:

- *Hyperbolic* LCS are structures characterized by the strongest attraction/repulsion;
- *Elliptic* LCS are closed material surfaces;
- *Parabolic* LCS are structures characterized by the strongest shearing.

In the present thesis, only hyperbolic LCS will be used.

2.4.3 Projection on a 2D space

Although Lagrange Coherent Structures can be applied in any high degrees-of-freedom system, in the present work their application will be limited to a 2-dimensional flow [21, 23]. In Section 3.2, it is shown that the dynamical system considered is a 6-dimensional one: some additional mapping needs to be introduced in order for the strainlines to be defined in a 2D space. The flow ψ is therefore introduced, which is related to the physical flow φ by [21]

$$\psi = \pi \circ XX2S \circ I2XX \circ \varphi \circ XX2I \circ S2XX \circ M$$

The successive transformation of the physical flow can be represented as

$$\mathbb{R}^2 \xmapsto{M} \mathbb{R}^6 \xmapsto{S2XX} \mathbb{R}^6 \xmapsto{XX2I} \mathbb{R}^6 \xmapsto{\varphi} \mathbb{R}^6 \xmapsto{I2XX} \mathbb{R}^6 \xmapsto{XX2S} \mathbb{R}^6 \xmapsto{\pi} \mathbb{R}^2$$

[1] Retrieved from: `https://en.wikipedia.org/wiki/Poincaré_map`. Last visited: 12/09/2021.

Such that

$$\begin{Bmatrix} x_0^{OP} \\ y_0^{OP} \end{Bmatrix} \mapsto \begin{Bmatrix} x_0^{OP} \\ y_0^{OP} \\ 0 \\ \dot{x}_0^{OP} \\ \ddot{y}_0^{OP} \\ 0 \end{Bmatrix} \mapsto \begin{Bmatrix} x_0^{XX} \\ y_0^{XX} \\ z_0^{XX} \\ \dot{x}_0^{XX} \\ \dot{y}_0^{XX} \\ \dot{z}_0^{XX} \end{Bmatrix} \mapsto \begin{Bmatrix} x_0 \\ y_0 \\ z_0 \\ \dot{x}_0 \\ \dot{y}_0 \\ \dot{z}_0 \end{Bmatrix} \mapsto \begin{Bmatrix} x_T \\ y_T \\ z_T \\ \dot{x}_T \\ \dot{y}_T \\ \dot{z}_T \end{Bmatrix} \mapsto \begin{Bmatrix} x_T^{XX} \\ y_T^{XX} \\ z_T^{XX} \\ \dot{x}_T^{XX} \\ \dot{y}_T^{XX} \\ \dot{z}_T^{XX} \end{Bmatrix} \mapsto \begin{Bmatrix} x_T^{OP} \\ y_T^{OP} \\ z_T^{OP} \\ \dot{x}_T^{OP} \\ \dot{y}_T^{OP} \\ \dot{z}_T^{OP} \end{Bmatrix} \mapsto \begin{Bmatrix} x_T^{OP} \\ y_T^{OP} \end{Bmatrix} \tag{2.25}$$

where OP stands for "Orbital Plane", identified by the initial osculating orbital elements. As will be explained in Section 3.3.5, the particle is supposed to start its motion at the perigee of an osculating ellipse. Therefore, given its radius of pariapsis r_{p0} and its argument of periapsis ω (i.e. given its polar coordinates), the derivation of the cartesian state is trivial.
In the mapping described in Equation 2.25:

- M is a function that returns the velocity vector associated to the input point given in cartesian coordinates. In particular, the periapsis velocity vector is given by

  $$\mathbf{v}_p = \sqrt{\frac{1+e}{r_p}}\mathbf{e}_v$$

  where $\mathbf{e}_v$ is the unit vector normal to the initial position vector;
- $S2XX$ is a rotation matrix relating the orbital plane with a generic reference frame XX where the osculating orbital elements are defined. In the present work such elements are defined in RTN@t_0, therefore the transformation assumes the following expression

  $$S2XX = \begin{bmatrix} \eta & \mathbf{0}_{3\times3} \\ \mathbf{0}_{3\times3} & \eta \end{bmatrix}$$

  with

  $$\eta = \begin{bmatrix} \cos\Omega & -\sin\Omega & 0 \\ \sin\Omega & \cos\Omega & 0 \\ 0 & 0 & 1 \end{bmatrix} \begin{bmatrix} 1 & 0 & 0 \\ 0 & \cos i & -\sin i \\ 0 & \sin i & \cos i \end{bmatrix}$$

- $XX2I$ is the rotation matrix relating the frame XX with the inertial reference frame I where the equations of motion are formulated (the EME2000 frame in this work). The expression of such transformation is given in Section 2.1.2;
- φ is the physical flow of the system, described in Section 2.3;
- $I2XX$ is the inverse of $XX2I$;
- $XX2S$ is the inverse of $S2XX$;
- π is the projection of the state to the 2D position, given by

  $$\pi(x, y, z, \dot{x}, \dot{y}, \dot{z}) = (x, y)$$

  where OP reference plane is the one defined previously and not the one associated to the final orbital elements.

It is now possible to compute the strainlines associated to the 2D flow ψ. The associated Cauchy-Green Strain Tensor is given by

$$\Delta = \Psi^T \Psi \tag{2.26}$$

where Ψ is the Jacobian of the ψ, computed through the chain rule as

$$\Psi = J_\Psi = J_\pi J_{S2XX}^T J_{XX2I}^T \Phi J_{XX2I} J_{S2XX} J_M \tag{2.27}$$

where:

- the Jacobian of the projection is given by

$$J_\pi = \begin{bmatrix} 1 & 0 & 0 & 0 & 0 & 0 \\ 0 & 1 & 0 & 0 & 0 & 0 \end{bmatrix}$$

- the Jacobian of the rotation matrices $S2XX$ and $XX2I$ are given by the matrices themselves and their inverse coincides with their transpose;
- Φ is the State Transition Matrix of the system, computed by integrating the Variational Equations defined in Section 2.3;
- the Jacobian of M is given by

$$J_M = \begin{bmatrix} 1 & 0 \\ 0 & 1 \\ 0 & 0 \\ \dfrac{\dot{x}}{\partial x} & \dfrac{\partial \dot{x}}{\partial y} \\ \dfrac{\dot{y}}{\partial x} & \dfrac{\partial \dot{y}}{\partial y} \\ 0 & 0 \end{bmatrix}$$

with

$$\begin{aligned} \frac{\partial \dot{x}}{\partial x} &= \sqrt{1+e}\frac{3xy}{2(x^2+y^2)^{7/4}} \\ \frac{\partial \dot{y}}{\partial y} &= -\sqrt{1+e}\frac{3xy}{2(x^2+y^2)^{7/4}} \\ \frac{\partial \dot{x}}{\partial y} &= \sqrt{1+e}\left(\frac{3y^2}{2(x^2+y^2)^{7/4}} - \frac{1}{(x^2+y^2)^{3/4}}\right) \\ \frac{\partial \dot{y}}{\partial x} &= \sqrt{1+e}\left(\frac{1}{(x^2+y^2)^{3/4}} - \frac{3x^2}{2(x^2+y^2)^{7/4}}\right) \end{aligned}$$

2.4.4 Strainlines

Because of the formulation of the Cauchy-Green Strain Tensor given in Equation 2.26 it is now possible to compute the associated Lagrangian Coherent Structures: for a 2D projection such as the one adopted, such structures are 1-dimensional curves called *strainlines*. In particular, it can be demonstrated that such curves are locally tangent to the the eigenvector ξ_1 associated to the smallest eivenvalue λ_1 of the CG Tensor $\Delta_{t_0}^{t_0+T}(\mathbf{x}_0)$ [12].
A strainline $\gamma(t_0) \subset \Omega \subseteq \mathbb{R}^2$ is the solution of the following Cauchy problem

$$\begin{cases} \mathbf{x}'(s) = \xi_1(\mathbf{x}(s),\, t_0,\, T) \\ \mathbf{x}(0) = \mathbf{x}_0 \in \Omega \\ |\xi_1| = 1 \end{cases} \tag{2.28}$$

Furthermore, the system of equations can be scaled as [12]

$$\begin{cases} \mathbf{x}'(s) = \tilde{\xi}_1(\mathbf{x}(s),\, t_0,\, T) \\ \mathbf{x}_0 = \mathbf{x}_0 \in \Omega \end{cases} \tag{2.29}$$

with

$$\tilde{\xi}_1(\mathbf{x}(s),\, t_0,\, T) = \text{sign}(\mathbf{x}(s))\, \alpha(\mathbf{x}(s))\, \xi_1(\mathbf{x}(s),\, t_0,\, T) \tag{2.30}$$

where:

- $\alpha(\mathbf{x}(s))$ allows to regularize the procedure and stop the integration if a degenerate point is approached. It is defined as

$$\alpha(\mathbf{x}(s)) = \left(\frac{\lambda_2(\mathbf{x}(s)) - \lambda_1(\mathbf{x}(s))}{\lambda_2(\mathbf{x}(s)) + \lambda_1(\mathbf{x}(s))} \right)^2$$

- $\text{sign}(\mathbf{x}(s))$ is introduced to ensure the smoothness of the strainline. At the $k-$th integration step, it must be verified that

$$\tilde{\xi}_1(\mathbf{x}(s),\, t_0,\, T) \cdot (\mathbf{x}_{k-1} - \mathbf{x}_k) \geqslant 0$$

Chapter 3

Ballistic Capture

The ballistic capture is a phenomenon by means of which a small body like an asteroid or a spacecraft can start orbiting a celestial body in a completely natural manner. This process is however only temporary, meaning that after a finite amount of time the particle will escape the primary it was orbiting, unless some sort of energy dissipation is introduced (such as thrusting manoeuvres, aerobraking [19], etc). Nevertheless, ballistic trajectories can perform multiple revolutions around the targeted celestial body and present a set of advantages with respect to traditional transfer methods, as mentioned in Section 1.2.

3.1 Weak Stability Boundary

As explained in Section 2.2.1, the simplest model that allows to compute ballistic capture trajectories is the CR3BP. Within this framework, five distinct equilibrium points can be identified: the *Lagrange points* or *libration points*, as shown in Figure 3.1. Out of these five points, three are located on the line passing through the primaries and are therefore called *collinear points*.

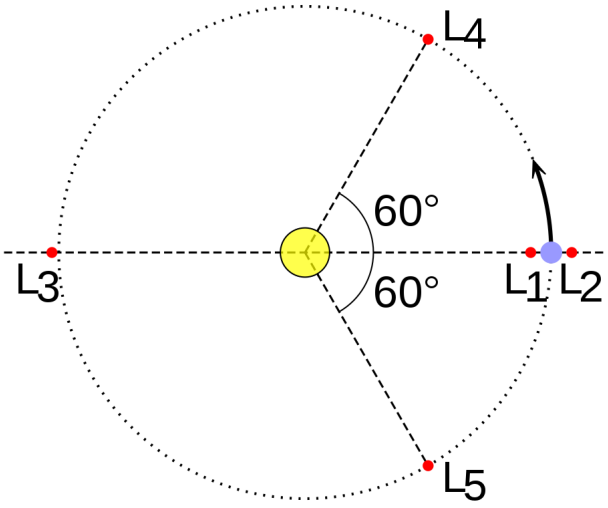

Figure 3.1: Lagrange points.[1]

These points represent unstable equilibrium points in the dynamics described by the CR3BP, meaning that from a mathematical standpoint they are associated with stable and unstable

[1]Retrieved from: `https://en.wikipedia.org/wiki/Trojan_(celestial_body)`. Last visited: 12/09/2021.

manifolds: topological structures that can be shown to be connected to what is referred to as Weak Stability Boundary (WSB) [13][2]. This is a particular region of the space around a celestial body where the transition from stable to unstable (and/or viceversa) ballistic trajectories manifests itself. It is now important to define what the terms *stable* and *unstable* mean.

The simplest description of the ballistic capture phenomenon can be given in the context of a *planar* CR3BP: the particle is bound to move onto the plane defined by the two primaries. In particular, the RPF reference frame defined in Section 2.1.3 will be used during the considerations done throughout the present section.
Recalling what was mentioned in Section 2.3.1, there exist infinite equivalent representations of the state vector. In the study of ballistic trajectories, the initial condition of the system is usually defined such that the particle starts its motion at the periapsis of an osculating ellipse

$$\mathbf{x}(t_0) = [a, e, i, \Omega, \omega, f]^T(t_0) = [a_0, e_0, i_0, \Omega_0, \omega_0, 0]^T = \mathbf{x}_0 \tag{3.1}$$

Due to the lower dimensionality of the planar problem, the set of indipendent variables reduces from 6 to 4:

$$\mathbf{x}_0 = [a_0, e_0, i_0, \Omega_0, \omega_0, 0]^T \longmapsto [a_0, e_0, \omega_0, 0]^T \tag{3.2}$$

In fact, i and Ω uniquely identify the plane where the motion takes place, which in this case is constrained to coincide with the one identified by the orbits of the primaries:

$$i(t) = i_0 \qquad \text{and} \qquad \Omega(t) = \Omega_0$$

Let also H be the Kepler energy of the particle with respect to the target body:

$$H = \frac{1}{2}v^2 - \frac{\mu}{r} \tag{3.3}$$

with

$$r = \frac{a(1-e^2)}{1 + e\cos f} \qquad \text{and} \qquad v = \sqrt{\mu\left(\frac{2}{r} - \frac{1}{a}\right)}$$

It is now possible to define the concept of *stability* within this framework [29]. With reference to Figure 3.2, consider the line emanating from the target primary and passing through the point identified by the initial osculating orbital elements of Equation 3.2: the trajectory is said to be *stable* if it completes a revolution about the target $P2$ maintaining a negative Kepler energy and without revolving around the primary $P1$, otherwise the motion is said to be *unstable*.

By considering a discretization of the plane and initial orbital eccentricity, the set of stable points (and therefore also the one of unstable points) is described through its algorithmic definition. For instance in [29], the search grid is defined as

$$r_p = [0, 2\cdot 10^{-3}, \ldots, 1.5], \quad \theta = [0, 2\pi/1000, \ldots, 2\pi] \quad \text{and} \quad e = [0, 0.05, \ldots, 0.95] \tag{3.4}$$

with $r_p = a(1-e)$ being the periapsis radius of the osculating ellipse. The set of initial conditions that result in stable trajectories is then defined as the following countable union of open intervals

[2]Such relation has also been shown exploiting the Poincaré map [7].

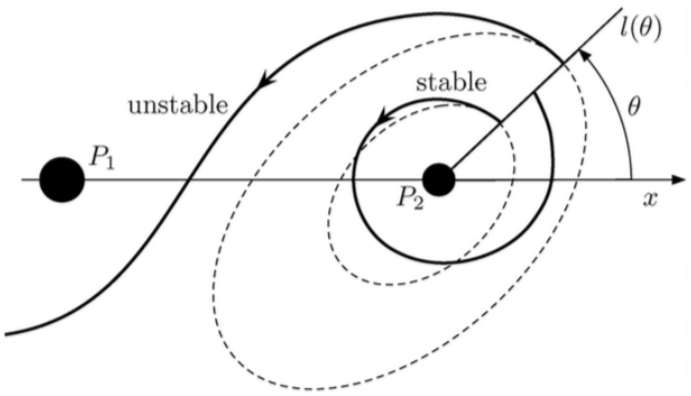

Figure 3.2: 2D stable and unstable trajectories. Here θ is the argument of periapsis [29].

$$\mathcal{W}(\theta, e) = \bigcup_{k \geqslant 1} (r^*_{2k-1}, r^*_{2k})$$

where r^* represent endpoints of stable intervals. By allowing θ to vary within the search space, the following set can be introduced

$$\mathcal{W}(e) = \bigcup_{\theta \in [0, 2\pi)} \mathcal{W}(\theta, e)$$

Finally, by considering the finite interval of eccentricities associated with negative Kepler energy, the *Stable Set* can be defined

$$\mathcal{W} = \bigcup_{e \in [0,1)} \mathcal{W}(e) \tag{3.5}$$

From the Stable Set $\mathcal{W}$, the Weak Stability Boundary (WSB) $\partial\mathcal{W}$ can be defined: as the notation suggests, it represents the contour of the Stable Set

$$\partial\mathcal{W} := \{r^*(\theta, e) \mid \theta \in [0, 2\pi),\ e \in [0, 1)\} \tag{3.6}$$

From a physical standpoint, the WSB represents the surface in the state space acting as separatrix between two different dynamical behaviours, such as stable and escape trajectories.

An additional consideration in the study of the WSB is accounting for the possibility of multiple revolutions about the target celestial body [13]. Given $n \in \mathbb{Z} - \{0\}$, the generalized Stable Set $\mathcal{W}_n$ is defined as the set containing those initial conditions that result in trajectories that perform n revolutions around the target primary, as shown in Figure 3.3. The concept of generalized Stable Sets automatically leads to the idea of generalized WSB. From $\mathcal{W}_n$, the generalized Weak Stability Boundary $\partial\mathcal{W}_n$ is defined as the locus of points $r^*(\theta, e)$, endpoints of the n-stable open intervals $(r^*_{2k-1},\ r^*_{2k})$.

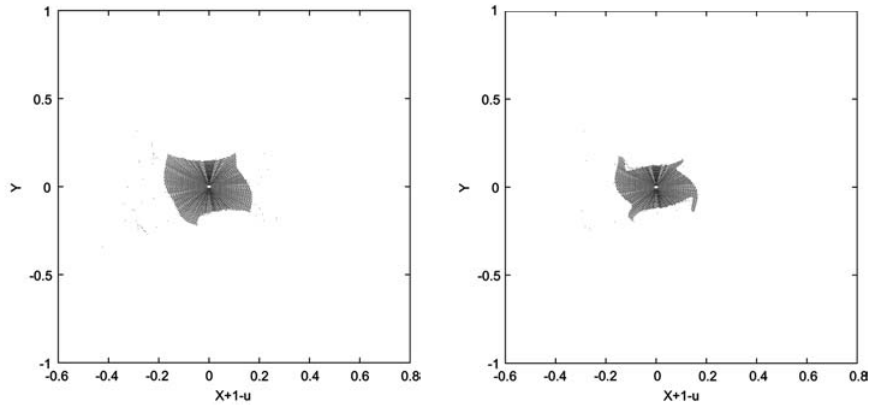

Figure 3.3: $\mathcal{W}_3$ (left) and $\mathcal{W}_6$ (right) in the Earth-Moon CR3BP with $e_0 = 0$ [13].

3.2 3D Model

A more comprehensive description of the ballistic capture phenomenon requires the analysis of 3D trajectories. If in the 2D case the surface identifying a complete revolution was a line, the 3D counterpart is a semi-plane. In fact, if one were to use the same stability criterion defined for the 2D model, the motion of the particle would always result unstable [25]. In an inertial reference frame, such plane is uniquely defined by the initial condition $\mathbf{x}_0$, as shown in Figure 3.4: in fact, considering the cartesian representation of the state vector, the plane is identified by all vectors $\mathbf{r} = [x, y, z]^T$ satisfying

$$\mathbf{r} \cdot (\mathbf{h}_0 \times \mathbf{r}_0) = 0 \tag{3.7}$$

with $\mathbf{h}_0$ being the specific angular momentum vector of the particle, defined as

$$\mathbf{h}_0 = \mathbf{r}_0 \times \mathbf{v}_0 \qquad \text{and} \qquad \mathbf{x}_0 = \begin{pmatrix} \mathbf{r}_0 \\ \mathbf{v}_0 \end{pmatrix}$$

The k-th intersection with the plane is achieved at time t_1 if

$$\mathbf{r}^{(k)}(t_1) \cdot (\mathbf{h}_0 \times \mathbf{r}_0) = 0 \tag{3.8}$$

In particular the intersection lies on the semi-plane of interest if

$$\mathbf{r}^{(k)}(t_1) \cdot \mathbf{r}_0 > 0 \tag{3.9}$$

Finally, the intersection coincides with a complete revolution if

$$(\mathbf{v}^{(k)} \cdot \mathbf{v}_0)\,(\mathbf{v}^{(k-1)} \cdot \mathbf{v}_0) > 0 \tag{3.10}$$

This last constraint is imposed to discard all the spurious intersections due to a possible "oscillatory" motion around the intersection semi-plane, as shown in Figure 3.4(b).

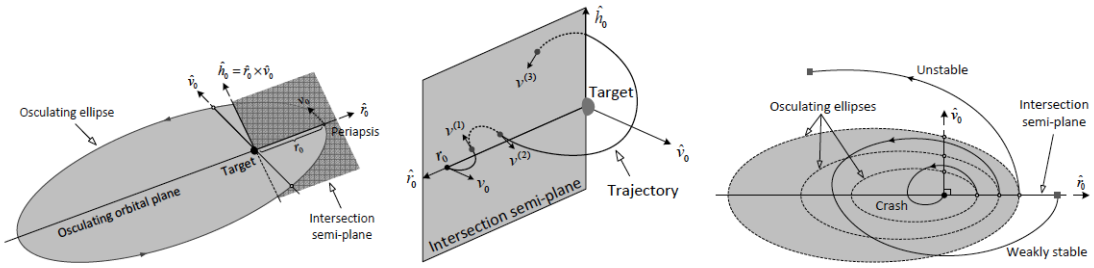

(a) Intersection plane (b) Multiple intersections (c) Orbit categories

Figure 3.4: 3D stable and unstable trajectories [20].

The particle is instead said to *escape* from the target at time t_e if:

$$H(t_e) > 0 \qquad \text{and} \qquad r(t_e) > R_{SOI} \tag{3.11}$$

where $R_{SOI} = a_t \left(\frac{\mu_t}{\mu_s}\right)^{2/5}$ represents the radius of the Sphere of Influence (SOI) of the primary. Escape occurs whenever the particle is found outside the SOI with positive Kepler energy.
An impact with the target at time t_i occurs if:

$$r(t_i) < R \tag{3.12}$$

with R being the mean equatorial radius of the planet.
Finally, an impact with the j-th moon of the target occurs at time t_m if:

$$\|\mathbf{r}(t_m) - \mathbf{r}_j\| < R_j \tag{3.13}$$

where R_j represents the mean equatorial radius of the j-th moon.

3.2.1 Trajectory Classification

It is now possible to divide the set of initial conditions into five non-intersecting subsets: for a given n, an initial condition can belong to one and only one subset.

- The n-Weakly Stable Set $\mathcal{W}_n$ contains those initial conditions resulting in trajectories that perform n complete revolutions around the target. An example is reported in Figure 3.5.

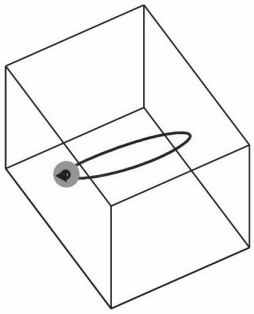

Figure 3.5: Weakly Stable sample trajectory [18].

- The n-Unstable Set $\mathcal{X}_n$ contains those initial conditions resulting in trajectories that perform $n-1$ complete revolutions around the target before escaping from the planet. An example is reported in Figure 3.6.

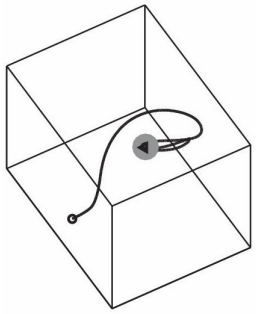

Figure 3.6: Unstable sample trajectory [18].

- The n-Crash Set $\mathcal{K}_n$ contains those initial conditions resulting in trajectories that perform $n-1$ complete revolutions around the target before impacting with the planet. An example is reported in Figure 3.7.

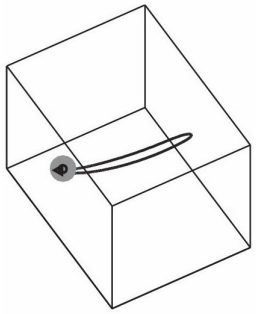

Figure 3.7: Crash sample trajectory [18].

- The n-Moon Crash Set $\mathcal{M}_n$ contains those initial conditions resulting in trajectories that perform $n-1$ complete revolutions around the target before impacting with a moon of the planet. An example is reported in Figure 3.8.

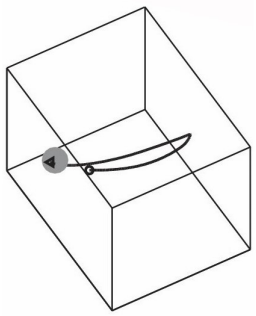

Figure 3.8: Moon Crash sample trajectory [18].

- The n-Acrobatic Set $\mathcal{D}_n$ contains those initial conditions resulting in trajectories that perform $n-1$ complete revolutions around the target and then do not verify none of the previous conditions within a given time span[3]. An example is reported in Figure 3.9.

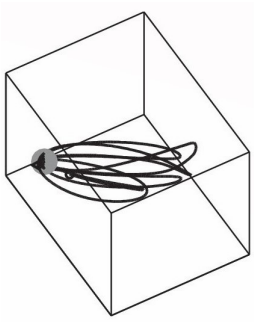

Figure 3.9: Acrobatic sample trajectory [18].

When the generalized WSB was introduced in Section 3.1, n was not bound to be a natural number, but rather any non-zero integer $n \in \mathbb{Z} - \{0\}$. When a negative value of n is considered the behaviour described is the one obtained by integrating the equations of motion in backward time. Because of this, *backward* stability (and consequently all other behaviours) can be defined. There is in fact nothing that constrains one initial condition to have the same type of behaviour both in forward and backward time.

From these considerations, the *Capture Set* can finally be introduced:

$$\mathcal{C}_{-1}^{n} := \mathcal{X}_{-1} \bigcap \mathcal{W}_n \tag{3.14}$$

The set $\mathcal{C}_{-1}^{n}$ is therefore defined as the set containing all the initial conditions that result in n-stable trajectories when propagated in forward time ($\mathcal{W}_n$ component) and escape trajectories in backward time ($\mathcal{X}_{-1}$ component).
Also the following additional intersection sets can be defined:

- the *Escape Set* $\mathcal{E}_{-n}^{1} = \mathcal{W}_{-n} \bigcap \mathcal{X}_1$, containing all initial conditions that result in trajectories that perform n revolutions in backward time and escape from the target in forward time (defining *ballistic escape trajectories*) [8, 30];
- the *Impact Set* $\mathcal{I}_{-1}^{n} = \mathcal{X}_{-1} \bigcap \mathcal{K}_n$, containing all initial conditions that result in trajectories that escape from the target in backward time and perform $n-1$ revolutions in forward time before impacting with the planet (defining *ballistic impact trajectories*) [24];
- the *Inject Set* $\mathcal{J}_{-1}^{n} = \mathcal{K}_{-1} \bigcap \mathcal{W}_n$, containing all initial conditions that result in trajectories that impact with the target in backward time and perform n revolutions in forward time (defining *ballistic inject trajectories*);
- the *Landing Set* $\mathcal{L}_{-n}^{1} = \mathcal{W}_{-n} \bigcap \mathcal{K}_1$, containing all initial conditions that result in trajectories that perform n revolutions in backward time and impact with the target in forward time (defining *ballistic landing trajectories*).

[3] Conventionally defined as the time required to cycle the Sphere of Influence four times: $\Delta t = 4 \cdot 2\pi \sqrt{\frac{R_{SOI}^3}{\mu}}$

Mathematics of the set manipulation

Let $\mathbb{I}$ be the set containing all initial conditions, the following relationship holds:

$$\mathcal{W}_n \bigcup \mathcal{X}_n \bigcup \mathcal{K}_n \bigcup \mathcal{M}_n \bigcup \mathcal{D}_n = \begin{cases} \mathbb{I} & \text{for } n = \pm 1 \\ \mathcal{W}_{n-1} & \text{for } n \geqslant 2 \\ \mathcal{W}_{n+1} & \text{for } n \leqslant -2 \end{cases} \tag{3.15}$$

Consider for instance the 3-Unstable Set $\mathcal{X}_3$: by definition, an initial condition that belongs to this set performs 2 revolutions before escaping from the target, it is therefore a subset of the 2-Stable Set $\mathcal{W}_2$. The same thought-process can be applied for the backward propagation. In general, it is true that:

$$\mathcal{G}_n \subseteq \begin{cases} \mathcal{W}_{n-1} & \text{for } n \geqslant 2 \\ \mathcal{W}_{n+1} & \text{for } n \leqslant -2 \end{cases} \tag{3.16}$$

where $\mathcal{G}_n$ is the n-Generic Set. This in turn means that $\mathcal{C}^n_{-1} \neq \mathcal{C}^1_{-n}$ (in this case with $n \geqslant 2$): both sets include trajectories that perform n revolutions about the target but they contain different initial conditions. Although they *qualitatively* describe the same type of dynamical behaviour, the two sets do not coincide. Moreover, exploiting Equation 3.16 it is possible to verify that:

$$\mathcal{C}^n_{-1} \bigcap \mathcal{C}^1_{-n} = \varnothing \tag{3.17}$$

3.2.2 Stability Index and Capture Ratio

Now that a rigorous definition of *ballistic capture trajectory* is available, there is the need to further classify the orbits obtained and search for those showing more desirable features. To this end, the Stability Index $\mathcal{S}$ is introduced [20]:

$$\mathcal{S} = \frac{t_n - t_0}{n} \tag{3.18}$$

with t_n being the time instant upon completion of the n-th revolution. From a physical point of view, such index represents the mean period of each revolution.
Another aspect to analyse is the occurrence of capture trajectories, the index introduced to consider it is the Capture Ratio [17]:

$$\mathcal{R}_{\mathcal{C}} = \frac{N_{\mathcal{C}^n_{-1}}}{N_{TOT}} \tag{3.19}$$

where $N_{\mathcal{C}^n_{-1}}$ is the number of elements belonging to the Capture Set (namely the number of initial conditions generating capture orbits) and N_{TOT} is the total number of initial conditions propagated during the analysis.

3.3 The influence of physical parameters

The classification given in Section 3.2.1 can be applied to any 3D model. However, it can be demonstrated that the eccentricity of the orbit of the target planet deeply influences the ballistic capture dynamics. For non-negligible eccentricity values, this implies that the CR3BP is not a suitable model to accurately describe the phenomenon at hand. Moreover, it can be proven that for some celestial bodies, including third-body perturbations can lead to different results [17].

3.3.1 The role of planet's eccentricity

As already anticipated, the planet's orbital eccentricity plays a fundamental role in the ballistic capture phenomenon. As Figure 3.10 shows, it can be noticed that increasing eccentricity results in higher values of the capture ratio $\mathcal{R}_\mathcal{C}$ and therefore denser capture sets.

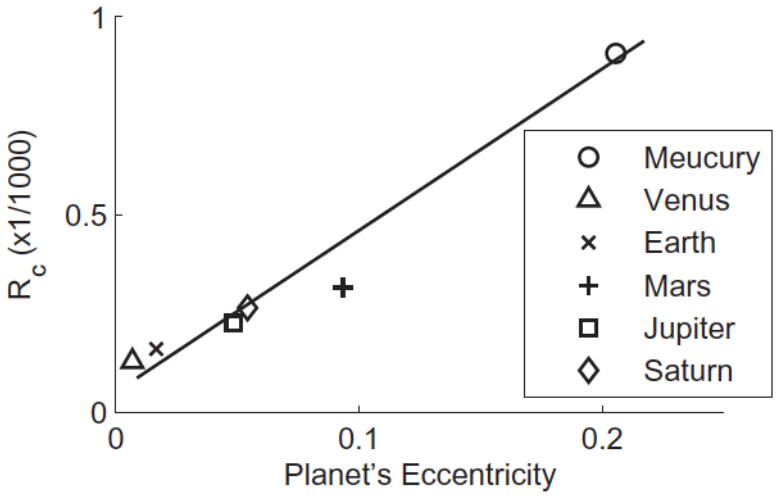

Figure 3.10: Capture ratio data points and trendline against planetary eccentricity [17].

It is also worth mentioning that the results obtained within the CR3BP differ also qualitatively from those returned by more accurate models. The trajectories computed are often very different from those given by the ER3BP and EPHE models, meaning that strong variations in the Stability Index $\mathcal{S}$ are likely to be observed [17].

3.3.2 The role of planet's true anomaly

The previous results have been obtained under the assumption that the planet is at its perihelion at the beginning of the simulations. Considering different initial positions along the orbit, variations in both $\mathcal{R}_\mathcal{C}$ and $\mathcal{S}$ can be observed. In particular [17]:

- the capture set is larger (i.e. $\mathcal{R}_\mathcal{C}$ is maximized) when:
  - $f \in [\pi/2,\, 3\pi/2]$ for prograde orbits;
  - $f \in [0,\, \pi/2] \vee [3\pi/2,\, 2\pi]$ for retrograde orbits;
- orbits are more regular (i.e. $\mathcal{S}_{\min}$ is minimized) when $f \in [0,\, \pi/2]$ for both prograde and retrograde orbits.

A graphical representation of these results can be appreciated in Figure 3.11.

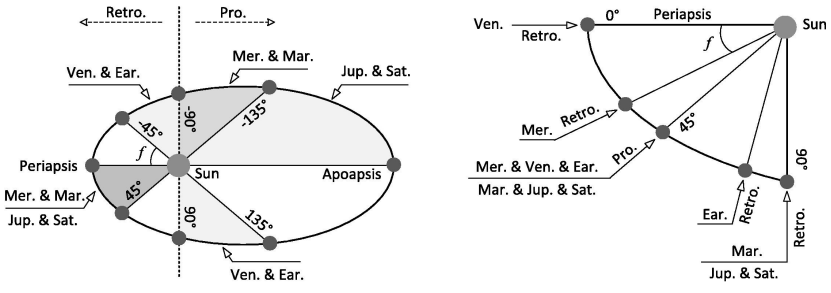

(a) Maximum $\mathcal{R}_c$ vs true anomaly

(b) Minimum $\mathcal{S}_{\min}$ vs true anomaly

Figure 3.11: True anomalies of maximum $\mathcal{R}_\mathcal{C}$ and $\mathcal{S}_{\min}$ [17].

3.3.3 The role of planet's natural satellites

At the beginning of the present Chapter 3, it was mentioned that ballistic trajectories require a source of energy dissipation in order to yield permanent capture. In particular, it is possible to exploit close passages of the planet's moons in order to achieve a *zero-cost* permanent capture [18].

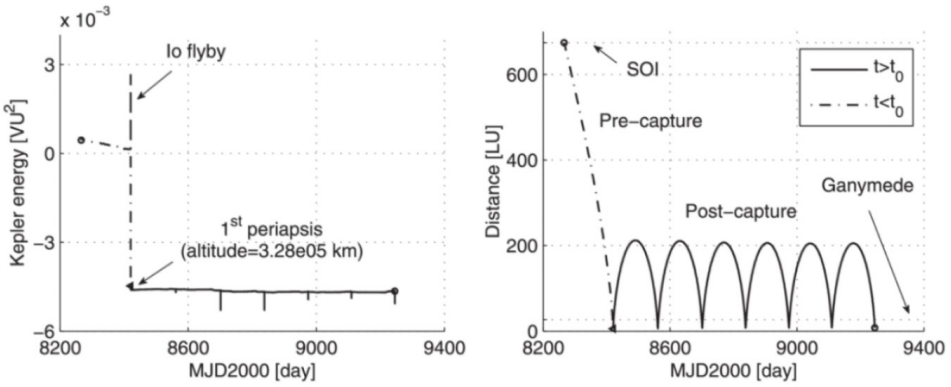

(a) Kepler energy wrt Jupiter (b) Distance to Jupiter

Figure 3.12: Permanent capture around Jupiter exploiting gravity assists [18].

In Figure 3.12 an example of such satellite-aided capture is reported: upon completion of the fly-by of Jupiter's moon Io, the Kepler energy is decreased such that the particle is thereafter trapped around the planet.
However, in order to achieve a significant change in the energy of the particle, the natural satellite where the gravity-assist is performed should have a strong enough gravitational influence. This in turn means that in a real case scenario, only large natural satellites such as the Moon or those orbiting outer planets are a suitable option.

3.3.4 The role of particle's plane orientation

Another aspect to be analysed is also the effect of the orientation of the plane associated with the particle's initial condition. In particular the following conclusions were reached [17]:

- the maximum chance for capture does not occur in the Sun-planet plane. Two different inclination ranges that maximize the capture ratio can be observed: $i_0 \in [40^\circ, 70^\circ]$ and $i_0 \in [150^\circ, 160^\circ]$;
- although sensitivity to right ascension is visible, no distinct pattern can be appreciated;
- prograde orbits evolve in more regular post-capture dynamics;
- the minimum Stability Index depends on the initial orientation, especially for polar orbits.

Figures 3.13 and 3.14 represent a visual representation of the previous considerations for various target planets. From left to right, top to bottom: Mercury, Venus, Earth, Mars, Jupiter, Saturn.

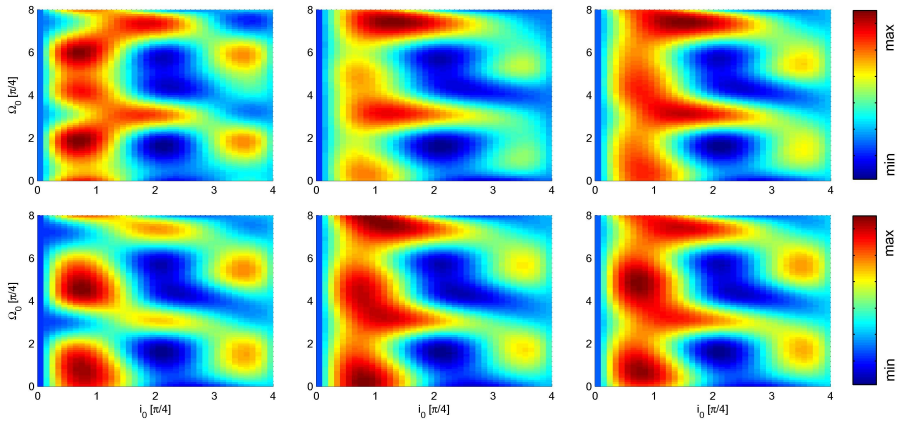

Figure 3.13: Capture Ratio at different i_0 and Ω_0 [17].

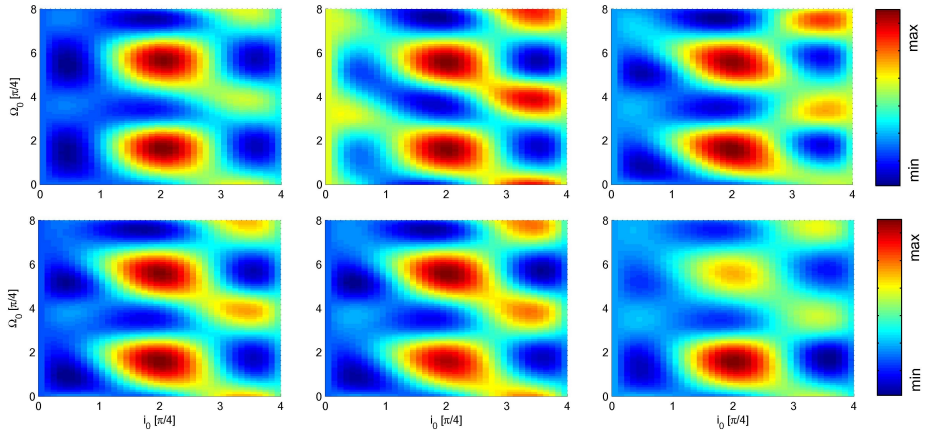

Figure 3.14: Stability Index at different i_0 and Ω_0 [17].

3.3.5 Additional remarks on particle's orbital elements

To completely and accurately describe gravitational capture, the six-dimensional infinite vector space defined by the orbital elements should be considered. In order to reduce the search space to a feasible one, some elements are therefore constrained to a predefined interval or fixed value. Conventionally:

- $f_0 = 0$, although nothing precludes the possibility of considering different angular positions. One advantage of this convention is ensuring the presence of at least one *true* apsidal point with orthogonal position and velocity vectors where efficient orbital manoeuvring could be performed.
- $e_0 \in [0.9, 1)$, although both smaller and larger values represent also valid options. In fact, it can be proven that initially parabolic (or hyperbolic) orbits can evolve into closed ones and that initially large circular orbits can result in escape trajectories. However, said interval has been proven to be a consistent source of valuable results [14].

3.4 Numerical Implementation

Throughout the previous chapters and sections little to no information about the implementation has been given. In the present section the main aspect concerning the numerical propagation of the dynamics of the system will be covered.
The integration of the equations of motion has been performed through the *GRAvity TIdal*

Slide (GRATIS) toolbox. Developed at Politecnico di Milano and written in MATLAB, its name recalls the idea of submarines exploiting the tidal phenomenon to save the expenses of underwater voyages. Moreover, the abbreviation GRATIS implicitly suggests the idea of something happening "for-free", just like the ballistic capture dynamics making use of the gravitational potential energy offered by the Solar System to develop "cost-free" trajectories.

Recalling Section 2.2, the equations of motion represent a system of ordinary differential equations (ODE), therefore built-in MATLAB integrators are a viable choice for the propagation of the dynamics: *ode113* has been selected [9]. This is a Variable Stepsize Variable Order (VSVO) integration scheme based on the Adams-Bashforth-Moulton method [22].

Another important feature introduced in GRATIS is the use of dimensionless quantities to describe the phenomenon. This allows to increase the efficiency of the numerical integration. The dimensionless units (DU) introduced within the toolbox and used in the present work are:

- the *length unit* LU, defined as the mean radius of the target celestial body

$$\mathrm{LU} = R$$

- the *gravity unit* MU, defined as the gravitational parameter of the target celestial body

$$\mathrm{MU} = \mu_t$$

- the *time unit* TU, defined as

$$\mathrm{TU} = \sqrt{\frac{\mathrm{LU}^3}{\mathrm{MU}}}$$

- the *velocity unit* VU, defined as

$$\mathrm{VU} = \frac{\mathrm{LU}}{\mathrm{TU}}$$

The numerical values of the dimensionless units for Mars (expressed in suitable multiples of the International System of Units) are given in Table 3.1.

DU	**Value**	**SI unit**
LU	3396	km
MU	$4.2828 \cdot 10^4$	$\mathrm{km}^3/\mathrm{s}^2$
TU	965.2814	s
VU	3.5513	km/s

Table 3.1: Dimensionless units at Mars.

Other important numerical values that have to be assigned are those describing the spacecraft itself. When discussing the SRP acceleration in Section 2.2.4, the reflectivity coefficient and the area-to-mass ratio (defined as the inverse of the mass-to-area ratio) were introduced. Within this work, the numerical values considered for such coefficients are:

$$\frac{m}{A} = 75\,\mathrm{kg/m}^2 \qquad \text{and} \qquad C_R = 1.3$$

The study of the ballistic capture phenomenon is therefore studied within GRATIS by defining a computational grid of initial conditions which are propagated and then classified by means of the definitions given in Section 3.2.1.

3.4.1 Loss of significance

Whilst the clever use of position vectors and size for the celestial bodies considered removes the need of introducing a regularization scheme (such as the Levi-Civita one used in the 2D-case [13, 14, 29]), a reformulation of the equations of motion is still necessary in order to avoid loss of significance during integration. In fact, recalling the right hand side of Equation 2.5 and considering only one term for simplicity (note that the same consideration holds also for the term associated to the Sun, on the left hand side of the equation)

$$\frac{\mathbf{r}_i}{r_i^3} + \frac{\mathbf{r} - \mathbf{r}_i}{\|\mathbf{r} - \mathbf{r}_i\|^3} \tag{3.20}$$

It is easy to verify that when the particle is in the vicinity of the target body ($\mathbf{r} \ll \mathbf{r}_i$)

$$\frac{\mathbf{r} - \mathbf{r}_i}{\|\mathbf{r} - \mathbf{r}_i\|^3} \approx -\frac{\mathbf{r}_i}{r_i^3}$$

This would result in the computer storing the result of Equation 3.20 with few significant digits, leading to large rounding errors.
However, it can be noted that Equation 3.20 has the following form

$$\frac{\mathbf{p}}{p^3} - \frac{\mathbf{d}}{d^3} \tag{3.21}$$

where:

- $\mathbf{p} = \mathbf{r}_i$ is the position vector of the i-th celestial body;
- $\mathbf{d} = \mathbf{r}_i - \mathbf{r}$ is the position of the i-th body relative to the particle (Figure 2.3).

It it possible to prove that Equation 3.21 can also be expressed as [5]

$$\frac{1}{d^3}(\mathbf{r} + f(q)\mathbf{p}) \tag{3.22}$$

with

$$f(q) = q\frac{3 + 3q + q^2}{1 + (1+q)^{3/2}} \qquad \text{and} \qquad q = \frac{\mathbf{r} \cdot (\mathbf{r} - 2\mathbf{p})}{\mathbf{p} \cdot \mathbf{p}}$$

Therefore, loss of significance can be avoided at the cost of a more complex formulation of the equations of motion which results in an increase of the computational demand.

Chapter 4

Methodology

This chapter will cover and explain the approach adopted and followed during the development of the present study, making use of the mathematical and numerical tools described in the previous chapters and sections.
Starting from the complete Capture Set $\mathcal{C}^6_{-1}$ at Mars for a given initial epoch, the present work studied the evolution in time of one particular sub-portion. Before explaining the methodology adopted, it is worth briefly analysing the initial Capture Set, shown in Figure 4.1. The assumptions under which it has been computed are:

- $t_0 = 8743$ MJD2000, corresponding to December 9^{th} 2023 and $f_t \approx 270°$;
- $r_{p0} = R + [100, 200, 300, \ldots, 10R]$ km;
- $e_0 = 0.99$;
- $i_0 = 36°$;
- $\Omega_0 = 36°$;
- $\omega_0 = [0, 1, 2, \ldots, 360]°$;
- $f_0 = 0°$;
- the set of perturbing bodies included are: Sun, Mercury, Venus, Earth, Jupiter, Saturn, Uranus, Neptune and the two martian moons Phobos and Deimos.

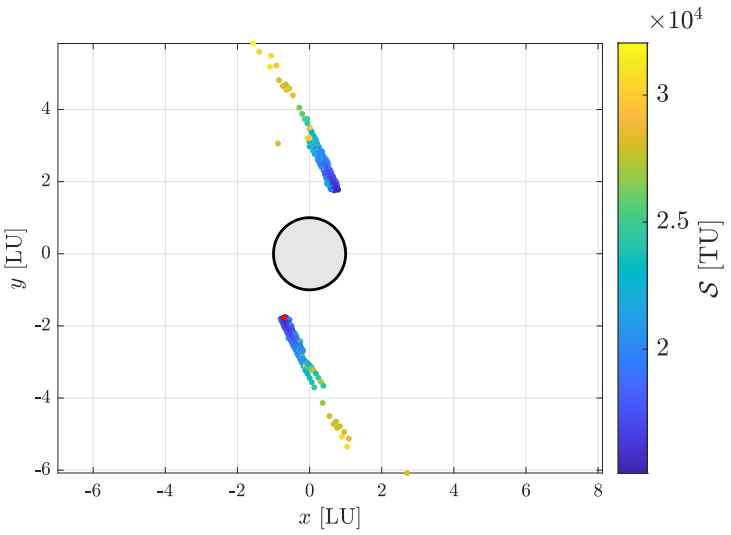

Figure 4.1: Capture set around Mars on December 9^{th} 2023. $\mathcal{S}_{\text{min}}$ shown in red.

One important aspect worth mentioning is that although the initial Capture Set accounts for the gravitational perturbations introduced by the martian satellites, the present study has neglected their contribution to reduce the computational burden. In fact, accounting for short-period objects in the equations of motion significantly increases the cost of the simulation, resulting in a higher number of integration steps and sensibly longer computational times [3].

4.1 Capture Region definition

Following up on the definition of Stability Index $\mathcal{S}$ given in Section 3.2.2, the region of interest of the Capture Set has been selected as a small circular region centred at the initial condition characterized by $\mathcal{S}_{\min} = \min(\mathcal{S})$.
As it can be seen in Figure 4.1, the initial condition associated with $\mathcal{S}_{\min}$ lies at the "edge" of the Capture Set. This can be explained by recalling how $\mathcal{C}^6_{-1}$ and $\mathcal{S}$ are defined (Equation 3.14 and Equation 3.18): in fact, the Stability Index is defined only on the post-capture arc of the trajectory (for $t \geqslant t_0$) and therefore characterizes only the $\mathcal{W}_6$ portion of the Capture Set. It is therefore likely that lower values of Stability Index exist within the 6-Stable Set that do not belong to the Capture Set

$$\exists\, \mathbf{x}_{nc} \;:\; \mathcal{S}(\mathbf{x}_{nc}) \;<\; \min_{\mathrm{x}_0 \in \mathcal{C}^6_{-1}} (\mathcal{S}),\; \mathbf{x}_{nc} \notin \mathcal{C}^6_{-1} \tag{4.1}$$

Whilst this consideration will be used in Section 4.3 to define a suitable radius of the region of interest, for the present analysis any arbitrary value could be selected. However, for the sake of coherence and homogeneity, the same value $r = 75$ km that will be explained in Section 4.3.3, will be used throughout the entirety of the study.
One more aspect to assess is the discretization used to analyse the problem. The grid chosen is defined with respect to its centre such that $r = [0, 7.5, 15, \ldots, 75]$ km and $\alpha = [0, 20, 40, \ldots, 360]^\circ$. Finer meshes have been tested and the one selected resulted in a good compromise between accuracy and computational time required.

During the early stages of this work various indices have been defined and considered. The choice of using the Stability Index $\mathcal{S}$ resulted from the review of the literature and of the state of the art. It is in fact the most used index to characterize the regularity of the post-capture trajectories. The other indices analysed are reported in Appendix B.

4.2 The role of the capture epoch

It is important to note that the orbital elements generating the Capture Set shown in Figure 4.1 are defined in the RTN reference frame. It is therefore fundamental to express the epoch at which the frame is defined. In fact, different time instants result in different reference frames:

$$\mathrm{RTN@}t_0 \neq \mathrm{RTN@}(t_0 + \delta t_0)$$

This difference is immediately evident when considering the rotation matrix between the RTN and the EME2000 reference frames given in Equation 2.1: the transformation in fact depends on the true anomaly f of the planet, directly function of the time instant considered.
From this consideration, two possible paths open when introducing the perturbation on the capture epoch:

- always defining the initial conditions in the RTN@t_0 coordinate system;
- defining the initial conditions in a *time-local* RTN@$(t_0 + \delta t_0)$ coordinate system.

Although the difference between reference frames caused by the variation in the capture epoch are infinitesimal, their effect cannot be neglected. In fact, whilst the former option corresponds to a "simple" perturbation δt_0 at the start of the propagation (accounting for the variation in the position of the bodies in the Solar System), the latter translates instead into a perturbation both in the initial epoch and in the initial condition $\mathbf{x}_0$ (due to the variation in the reference frame), as schematically shown in Figure 4.2. Within this thesis, both approaches will be covered and analysed.

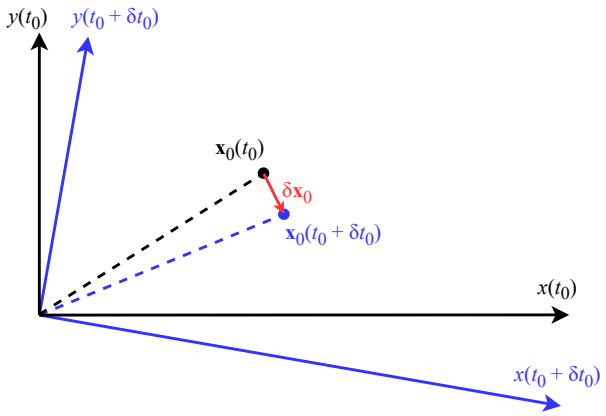

Figure 4.2: 2D representation of the $\delta\mathbf{x}_0$ perturbation introduced by RNT@$(t_0 + \delta t_0)$.

4.3 Algorithmic propagation through Stable Sets

Within the context described, the defined region has been investigated at a finite number of initial epochs. In particular, the analysis stops whenever one of the following condition is satisfied:

- the region does not intersect the Capture Set

$$\mathcal{R} \bigcap \mathcal{C}^6_{-1} = \varnothing \quad \text{or equivalently} \quad \nexists\, \mathbf{x}_0 \in \mathcal{R},\ \mathbf{x}_0 \in \mathcal{C}^6_{-1}$$

- the region completely belongs to the Capture Set

$$\mathcal{R} \bigcap \mathcal{C}^6_{-1} = \mathcal{R} \quad \text{or equivalently} \quad \nexists\, \mathbf{x}_0 \in \mathcal{R},\ \mathbf{x}_0 \notin \mathcal{C}^6_{-1}$$

where $\mathcal{R}$ represents the region of interest. In particular, the second criterion ensures that the "edge" of the Capture Set (where $\mathcal{S}_{\text{min}}$ is located) always intersects the region investigated.

Because of the two possibilities mentioned in Section 4.2 when discussing the effect of the capture epoch on the reference frame, three different types of analyses with increasing degree of complexity have been conducted:

- same set of initial orbital elements with fixed reference frame RTN@t_0;
- same set of initial orbital elements with varying reference frame RTN@$(t_0 + \delta t_0)$;
- varying set of initial orbital elements with varying reference frame RTN@$(t_0 + \delta t_0)$.

4.3.1 Fixed orbital elements in fixed reference frame

In this context, the frame where the initial osculating orbital elements are defined coincides with the one used to generate the Capture Set shown in Figure 4.1. From a planeto-centric standpoint, the set of initial conditions expressed in EME2000 cartesian coordinates always identify the same set of initial states: the patching points between pre-capture and post-capture

arcs are identical, independently from the variation δt_0 considered. A schematic representation of the workflow adopted throughout this analysis is reported in Figure 4.3.

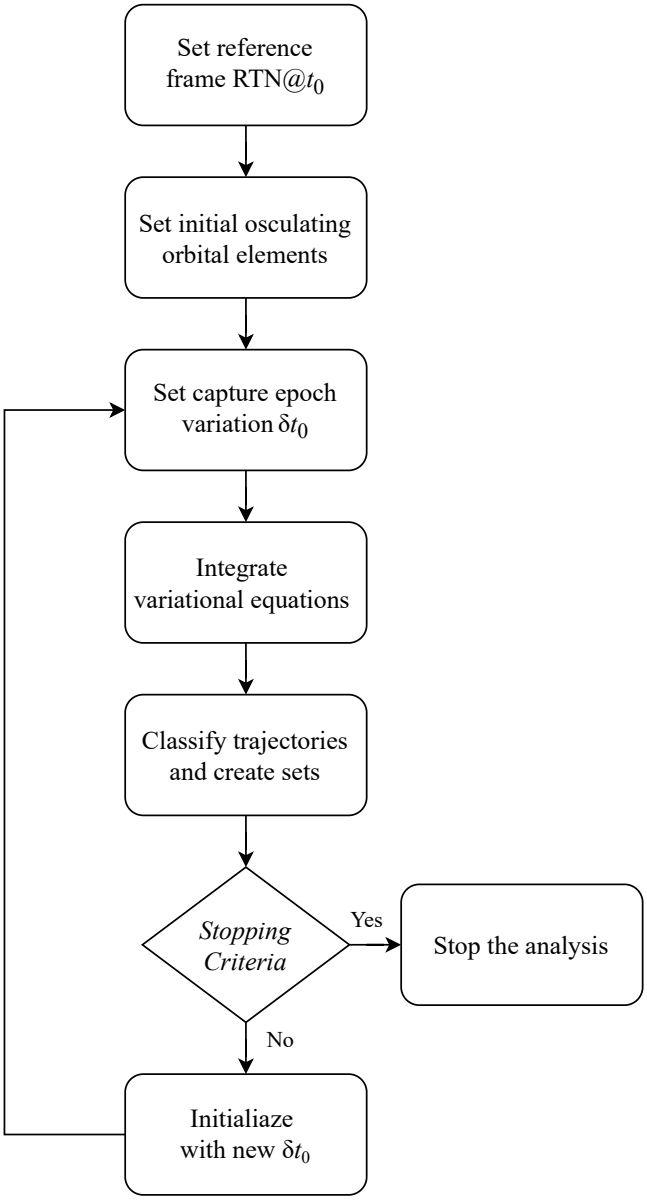

Figure 4.3: Workflow for fixed orbital elements in fixed reference frame.

From the integration of the Variational Equations the time history of the STM associated with each initial condition is obtained. This it turn means that also the derivative of the flow with respect to the initial epoch can be computed through Equation 2.24

$$\frac{\mathrm{d}\varphi^t_{t_0}}{\mathrm{d}t_0} = -\Phi^t_{t0}\,\mathbf{f}(t_0, \mathbf{x}_0) \quad \text{for } t \in [t_0,\, t_f]$$

where t_f represents the time instant which satisfies one of the criteria reported in Section 3.2.1 and therefore stops the integration of the Variational Equations. Under the assumption of small variations with respect to the nominal condition, it is possible to assume that

$$\varphi^t_{t_0+\delta t_0}(\mathbf{x}_0) \approx \tilde{\varphi}^t_{t_0+\delta t_0}(\mathbf{x}_0) = \varphi^t_{t_0}(\mathbf{x}_0) + \frac{\mathrm{d}\varphi^t_{t_0}}{\mathrm{d}t_0}\delta t_0 \tag{4.2}$$

where $\tilde{\varphi}^t_{t_0+\delta_t 0}$ is the approximated flow. The results obtained from this analysis will be presented in Section 5.1.

4.3.2 Fixed orbital elements in varying reference frame

Within this framework the initial osculating orbital elements are defined in a *time-local* RTN@$(t_0 + \delta t_0)$ reference frame. This in turn means that with respect to the EME2000 planetocentric coordinate system, a different set of initial conditions (i.e. a different region of the phase space) is considered for each capture epoch

$$\mathbf{x}_0(t_0) \neq \mathbf{x}_0(t_0 + \delta t_0) \quad \forall\, \mathbf{x}_0 \in \mathcal{R}$$

A diagram of the workflow adopted throughout this analysis is reported in Figure 4.4.

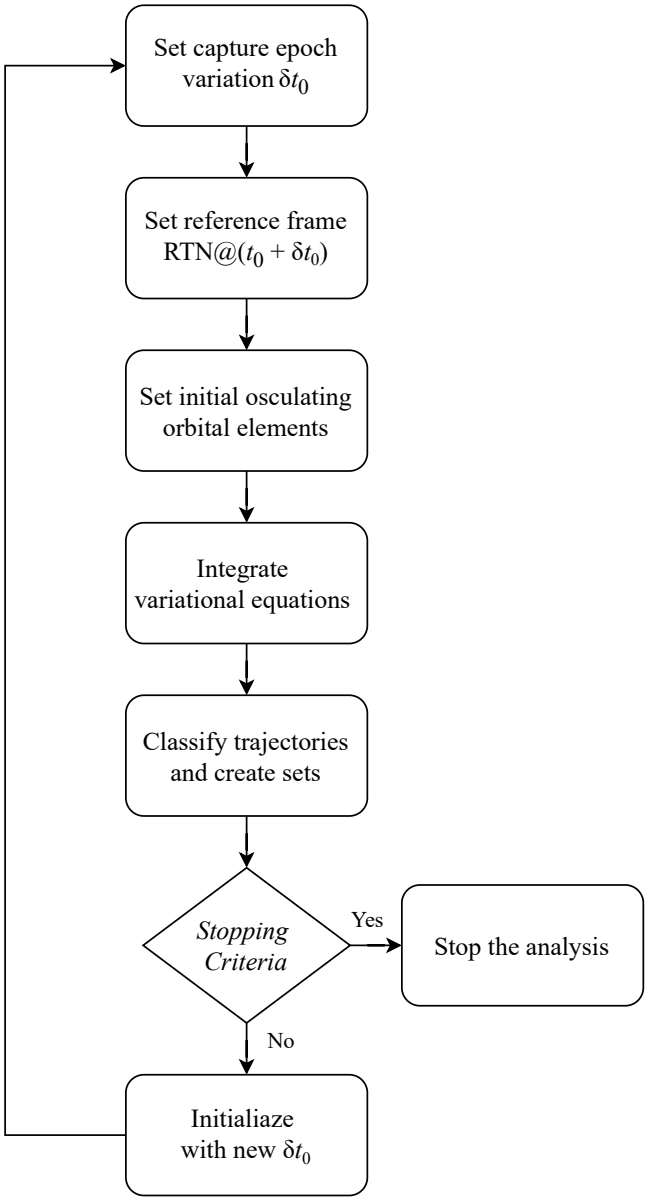

Figure 4.4: Workflow for fixed orbital elements in varying reference frame.

By comparing the workflows reported in Figure 4.3 and Figure 4.4 it is easy to verify that the methods differ in the way the feedback loop is applied: whilst in the former the block creating the initial osculating orbital elements is outside of the loop, in the latter it is instead completely

enclosed. In fact, this directly follows from the considerations made in Section 4.2 and at the beginning of the current one.

With the same rationale followed in Section 4.3.1 the derivative of the flow can be computed. However, in order to estimate the flow generated by $\mathbf{x}_0(t_0 + \delta t_0)$ starting from the integration of $\mathbf{x}_0$, Equation 4.2 becomes

$$\varphi^t_{t_0+\delta t_0}(\mathbf{x}_0 + \delta\mathbf{x}_0) \approx \tilde{\varphi}^t_{t_0+\delta t_0}(\mathbf{x}_0 + \delta\mathbf{x}_0) = \varphi^t_{t_0}(\mathbf{x}_0) + \frac{\mathrm{d}\varphi^t_{t_0}}{\mathrm{d}t_0}\delta t_0 + \Phi^t_{t_0}\delta\mathbf{x}_0 \tag{4.3}$$

with $\delta\mathbf{x}_0 = \mathbf{x}_0(t_0 + \delta t_0) - \mathbf{x}_0(t_0)$ as shown in Figure 4.2.
The difference between Equation 4.2 and Equation 4.3 lies in the term $\Phi^t_{t_0}\delta\mathbf{x}_0$: this term accounts for the infinitesimal difference between the reference frames in which the initial conditions are defined at the different capture epochs.

The results associated with the current analysis will be presented in Section 5.2.

4.3.3 Varying orbital elements in varying reference frame

The analysis described hereafter constitutes a variation of the one previously described in Section 4.3.2. In this context the reference frame is once again defined in a *time-local* fashion, therefore rotating according to the position of the planet along its orbit. The new feature introduced in this study is the investigation of a different region of space at each capture epoch. In particular the set of initial osculating orbital elements considered at each iteration will depend on the results of the ones studied at the previous epoch. Once the region is propagated and classified, the Stability Index is computed for those initial conditions resulting in ballistic capture trajectories and the one associated with the lowest value of $\mathcal{S}$ is selected as the centre of the region at the following iteration (with same dimensions and discretization). A scheme of the workflow applied within the current analysis is reported in Figure 4.5.

Because of the way the centre is defined, it is important to recall Section 4.1: since $\mathcal{S}_{\min}$ is likely to lie on the "edge" of the Capture Set (which in the case at hand coincides with the WSB of $\mathcal{W}_6$), it is important to ensure that the region is not entirely enclosed within $\mathcal{C}^6_{-1}$

$$\mathcal{R} \not\subset \mathcal{C}^6_{-1} \quad \text{or, equivalently} \quad \exists\, \mathbf{x}_0 \in \mathcal{R},\ \mathbf{x}_0 \notin \mathcal{C}^6_{-1} \tag{4.4}$$

The value of $r = 75$ km anticipated in Section 4.1 directly follows from this concept. Such radius is sufficiently large to satisfy Equation 4.4 yet able to limit the computational cost of the analysis. It is worth highlighting that such condition shall be satisfied at any iteration: a smaller radius could result in the region being "saturated" at a generic time epoch $t_0 + \delta t_0$.

In accordance with the previous analyses, the derivative of the flow is computed through Equation 2.24 whilst Equation 4.3 can be used to estimate the flow generated by $\mathbf{x}_0(t_0 + \delta t_0)$. However, due to the difference between the two methods it is convenient to reformulate such equation as follows

$$\varphi^t_{t_0+\delta t_0}(\mathbf{x}_0 + \delta\mathbf{x}_0) \approx \tilde{\varphi}^t_{t_0+\delta t_0}(\mathbf{x}_0 + \delta\mathbf{x}_0) = \varphi^t_{t_0}(\mathbf{x}_0) + \frac{\mathrm{d}\varphi^t_{t_0}}{\mathrm{d}t_0}\delta t_0 + \Phi^t_{t_0}(\delta\mathbf{x}_0^{(\mathrm{R})} + \delta\mathbf{x}_0^{(\mathrm{T})}) \tag{4.5}$$

where $\delta\mathbf{x}_0^{(\mathrm{R})}$ and $\delta\mathbf{x}_0^{(\mathrm{T})}$ are the infinitesimal variations in the initial condition $\mathbf{x}_0$ due to the rotation of the RTN reference frame caused by the perturbation δt_0 in the capture epoch and by the translation of the centre of the region, respectively.

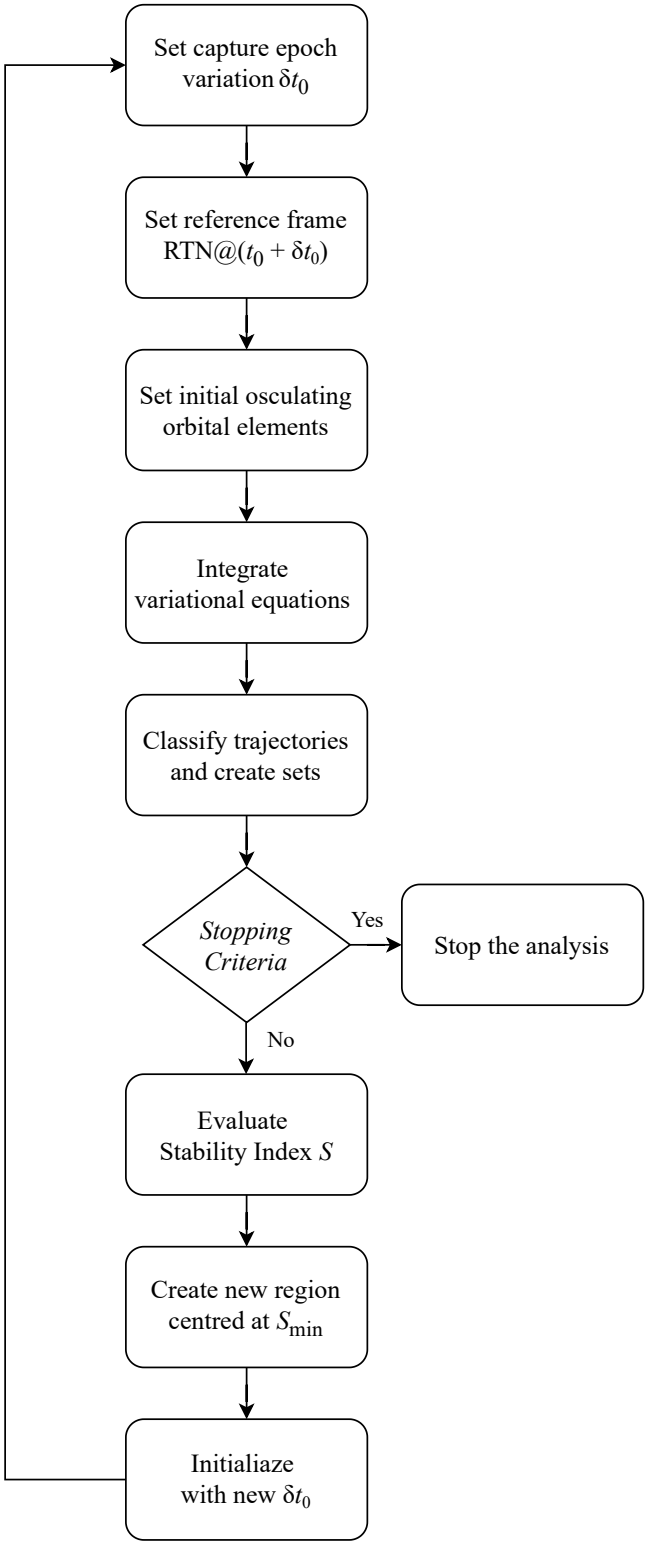

Figure 4.5: Workflow for varying orbital elements in varying reference frame.

The results obtained from the present analysis will be presented in Section 5.3.

4.4 Stroboscopic Strainlines

In order to achieve a complete description of the region considered, also stroboscopic strainlines have been used [21]. They are a useful tool when attempting to identify the WSB, where $\mathcal{S}_{\min}$ is likely to be found.
In order to compute such strainlines, the Cauchy problem defined in Equation 2.29 is integrated. The propagation of such system requires a boundary condition $\mathbf{x}_0$. Such point is defined by inspecting the circumference delimiting the region and identifying the "last" point belonging to the Stable Set. The procedure is schematically reported in Figure 4.6.

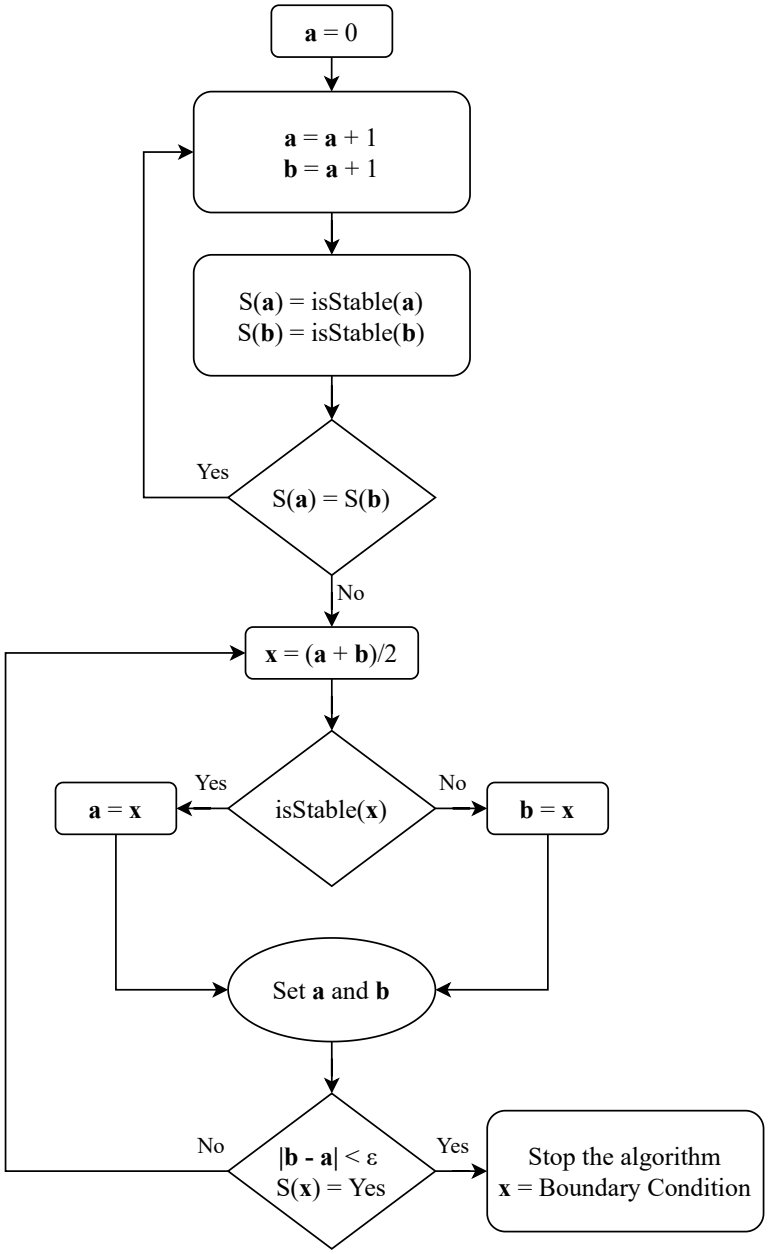

Figure 4.6: Algorithm identifying the boundary condition $\mathbf{x}_0$.

where:

- **a**, **b** and **x** are angles (expressed in degrees) associated to different points on the perimeter of the circular region;
- isStable(z) is a function that evaluates whether the point associated to the input angle z belongs to the Stable Set following the criteria defined in Section 3.2.1;
- ε is the tolerance stopping the algorithm (set to 10^{-10} in this work).

In the region analysed, the WSB will intercept the circumference in two distinct points (tangency is prevented by Equation 4.4). This in turn means that the algorithm can identify two distinct boundary conditions ($\mathbf{x}_0^{(1)}$ and $\mathbf{x}_0^{(2)}$), as shown in Figure 4.7.

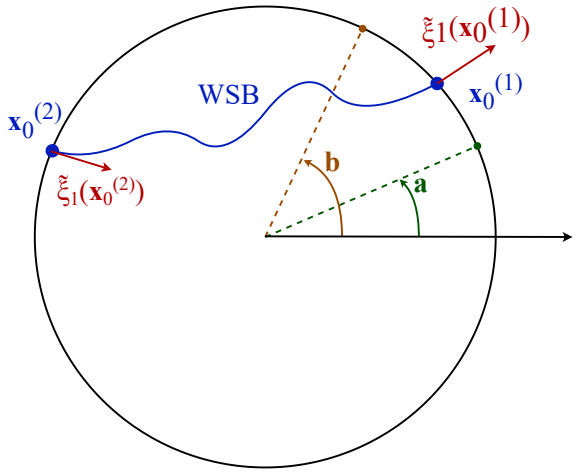

Figure 4.7: Example of two distinct boundary conditions identified by the algorithm.

Since both $\mathbf{x}_0^{(1)}$ and $\mathbf{x}_0^{(2)}$ represent valid choices, Equation 2.29 has to be modified. In fact, the example reported in Figure 4.7 clearly shows that for one of the two boundary conditions the associated eigenvector $\tilde{\xi}_1(\mathbf{x}_0^{(1)})$ points outwards with respect to the region. This in turn would result in the strainline being computed on the outside neighbourhood of the region. In order to correct such pointing discrepancies, the following coefficient is introduced

$$\beta(\mathbf{x}(s)) = \text{sign}(\tilde{\xi}_1(\mathbf{x}(s)) \cdot (\mathbf{x}_0^{(f)} - \mathbf{x}_0^{(i)})) \tag{4.6}$$

where $\mathbf{x}_0^{(i)}$ is the boundary condition selected for the Cauchy problem and $\mathbf{x}_0^{(f)}$ is the remaining one. Equation 2.30 now becomes

$$\tilde{\xi}_1(\mathbf{x}(s),\, t_0,\, T) = \beta(\mathbf{x}(s))\text{sign}(\mathbf{x}(s))\, \alpha(\mathbf{x}(s))\, \xi_1(\mathbf{x}(s),\, t_0,\, T) \tag{4.7}$$

Chapter 5

Results

In this chapter the results obtained from the methodology outlined throughout Chapter 4 will be presented and compared against previous findings, whenever possible. During the exposition, some sample orbits computed will be shown, both in inertial and pulsating frames. Additionally, the state vectors and the estimation error of $\tilde{\varphi}^t_{t_0+\delta t_0}(\mathbf{x}_0)$ will be reported, highlighting the results obtained when predicting the flow variations caused by perturbations in the capture epoch. Finally, the Capture Sets will be compared with the respective strainlines.

5.1 Fixed orbital elements in fixed reference frame

According to the procedure defined in Section 4.3.1, a circular region of radius $r = 75$ km has been investigated at a finite number of capture epochs with a time step of 1 day

$$\delta t_0^{(i+1)} = \delta t_0^{(i)} + 1 \text{ day}$$

In particular, the stopping criteria defined resulted in the analysis stopping at $\delta t_0 = 4$ days: because of the emptiness criterion being verified, useful data span time epochs in the range [0, 3] days. As expected from the considerations of Section 4.1 and confirmed by Figure 5.1, $\mathcal{S}_{\min}$ lies on the "edge" of the Capture Set. Moreover, it appears immediately that the variation on the capture epoch causes the number of ballistic capture trajectories to diminish as larger values of δt_0 are considered. Recalling the definition of Capture Ratio given in Section 3.2.2 and limiting its evaluation to the region of interest, it is true that

$$\mathcal{R}_{\mathcal{C}}(\delta t_0^{(i+1)}) < \mathcal{R}_{\mathcal{C}}(\delta t_0^{(i)})$$

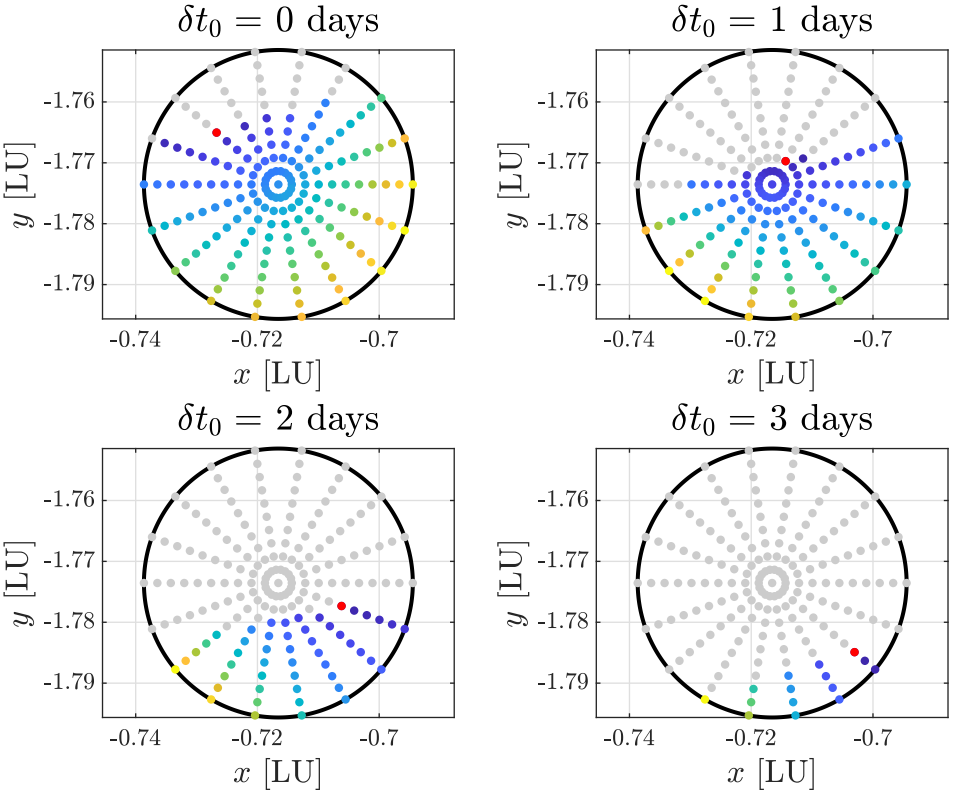

Figure 5.1: Capture Sets at different δt_0. $\mathcal{S}_{\min}$ shown in red, computational grid in grey.

5.1.1 Validation of the fixed-fixed approximation

Exploiting Equation 4.2 it is possible to obtain the value of the approximated flow at a generic δt_0. Because approximating the region at the same epochs where it is computed exactly would not be of particular interest, such technique will be used to estimate the behaviour at a capture epoch not previously considered. In particular for $\delta t_0 = 0.25$ days, Figure 5.4 shows the comparison between the *nominal* flows $\varphi^t_{t_0}$ and $\varphi^t_{t_0+\delta t_0}$ and the approximation of the latter $\tilde{\varphi}^t_{t_0+\delta t_0}$ generating from the initial condition at centre of the region. Figure 5.5 reports the L^2-norm of the associated approximation error, computed as

$$err(t) = \frac{\|\varphi^t_{t_0+\delta t_0} - \tilde{\varphi}^t_{t_0+\delta t_0}\|}{\|\varphi^t_{t_0+\delta t_0}\|} \tag{5.1}$$

When computing the error it is important to recall that the quantities investigated are the discrete output of a numerical integration. In particular, since the integration scheme used employs a control on the stepsize (Section 3.4), the history of the flows is interpolated such that the quantities are consistent. Moreover, since the integration is stopped according to the criteria defined in Section 3.2.1, also the time span covered by $\varphi^t_{t_0}$ (and therefore also by $\tilde{\varphi}^t_{t_0+\delta t_0}$) and $\varphi^t_{t_0+\delta t_0}$ could be different.

One more remark worth mentioning is the fact that the approximation disregards a small initial portion of the time history (both in forward and backward time). It can be experimentally verified that for $|t| \lesssim 150$ TU the error is too large to consider any result obtained for such intervals. However, this does not represent a major issue when comparing the length of such interval and the integration span: in fact the time scale of the dynamics is in the range of 10^4 TU. Such behaviour can be explained by considering Equations 2.14 and 2.24

$$\frac{\mathrm{d}\varphi^t_{t_0}}{\mathrm{d}t_0} \overset{(t\to 0)}{=} -\mathbf{f}(\mathbf{x}_0, t_0) \tag{5.2}$$

and therefore Equation 4.2 becomes

$$\tilde{\varphi}^t_{t_0+\delta t_0}(\mathbf{x}_0) \overset{(t\to 0)}{=} \varphi^t_{t_0}(\mathbf{x}_0) - \mathbf{f}(\mathbf{x}_0, t_0)\delta t_0 \tag{5.3}$$

meaning that for sufficiently small t, the approximation is constructed as an Euler step of size δt_0. Provided that the step is sufficiently small, the Euler method could accurately approximate the real behaviour, however, since the step has a fixed value of $\delta t_0 = 0.25$ days, it is not suitable to describe a complex highly nonlinear dynamics such as the one at hand. As t increases the integration of the STM embeds the dynamics of the phenomenon and the accuracy of the approximation improves.
To better examine the approximation, the same procedure has been applied also for $\delta t_0 = [0.50, 0.75, 1]$ days. As expected, the error increases for larger variations in the capture epoch, as can be observed in Figure 5.2.

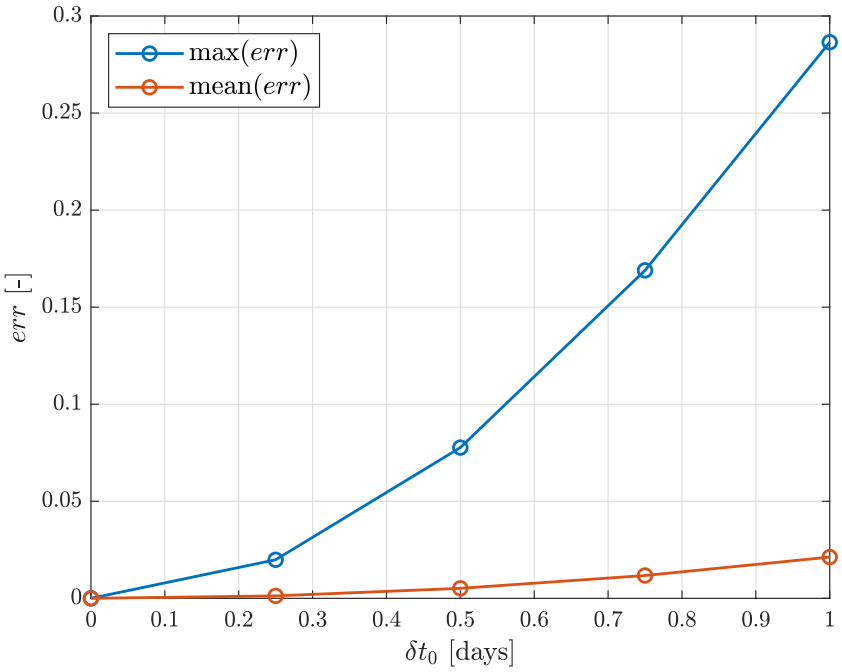

Figure 5.2: Comparison of the approximation error for different values of δt_0.

Whilst the maximum error increases significantly for increasing δt_0, the mean error remains limited and therefore the approximated trajectory qualitatively describes the real dynamics with discrete accuracy. However, it can be noted that the same process can be performed from the other extreme of the time interval: considering as nominal condition the region at $t_0 + 1$ day and approximating the dynamics "from the right". Therefore a more clever way of constructing the approximation is to modify Equation 4.2 as follows

$$\tilde{\varphi}^t_{t_0+\delta t_0} = \begin{cases} \varphi^t_{t_0} + \dfrac{\mathrm{d}\varphi}{\mathrm{d}t_0}\delta t_0 & \text{for } \delta t_0 \lesssim 0.5 \\ \varphi^t_{t_0+1} + \dfrac{\mathrm{d}\varphi}{\mathrm{d}t_0}(1-\delta t_0) & \text{for } \delta t_0 \gtrsim 0.5 \end{cases} \tag{5.4}$$

where δt_0 is expressed as a fraction of the time interval (which in the present example is equal to 1 day). Using this consideration, Figure 5.3 reports the associated approximation error.

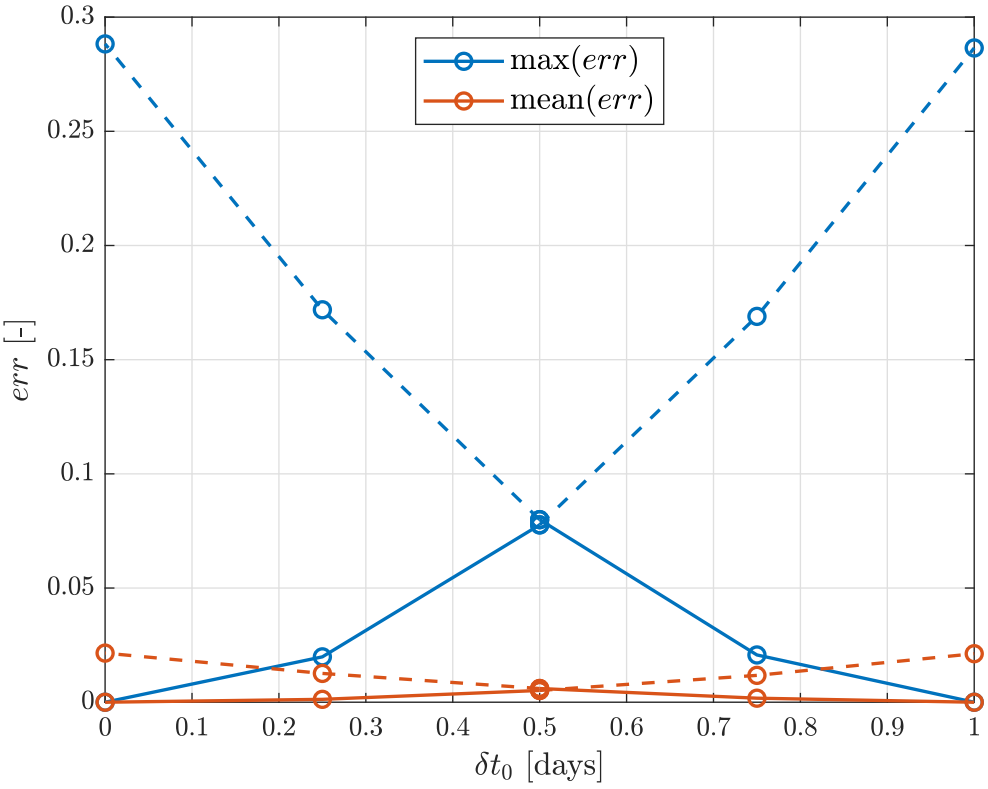

Figure 5.3: Compensated estimation error at different δt_0. The dashed lines represent the non-compensated errors of the estimation.

It is worth noticing that due to the complexity of the ballistic capture phenomenon, the knowledge of which approximation is more suitable for $\delta t_0 \approx 0.5$ is not available a priori.

Observing Figures 5.4 and 5.5, it is immediate to verify that peaks in the approximation error coincide with sharp changes in the state variables. In fact, in the post-capture arc such peaks coincide with close-approaches (not necessarily complete revolutions), whilst for the pre-capture phase only one peak is encountered and corresponds to the particle approaching the escape condition. A possible explanation of this behaviour could be the high sensitivity of such portions of the trajectory: in fact, in such points the propagation demands more integration steps to guarantee the requested accuracy, implying that the dynamics is extremely sensitive.

Figures 5.6 and 5.7 report the trajectories generated by the exact flows $\varphi^t_{t_0}$ and $\varphi^t_{t_0+\delta t_0}$ as well as by the approximated one $\tilde{\varphi}^t_{t_0+\delta t_0}$ in EME2000 and RPF reference frames, respectively. It is easy to verify that although the approximation error reported in Figure 5.5 reaches a maximum value of 2%, the trajectory computed approximates with discrete accuracy the exact behaviour: the mean error (0.1%) is in fact considerably smaller than the maximum.

The results obtained for the limiting case of $\delta t_0 = 0.5$ days are reported in Appendix B.

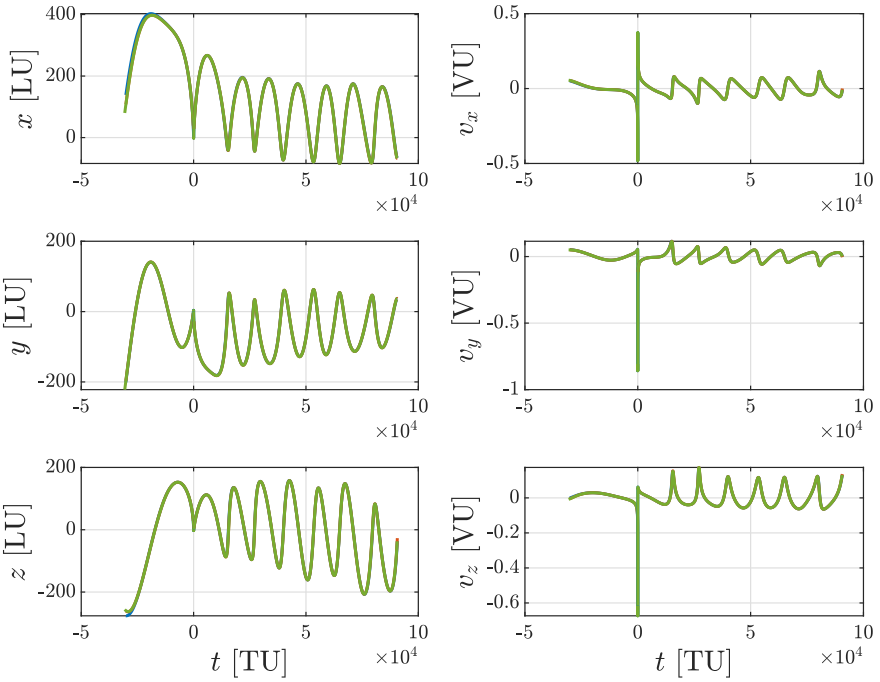

Figure 5.4: State vectors for $\varphi^t_{t_0}$ (blue), $\varphi^t_{t_0+\delta t_0}$ (green), and $\tilde{\varphi}^t_{t_0+\delta t_0}$ (orange) for $\delta t_0 = 0.25$ days.

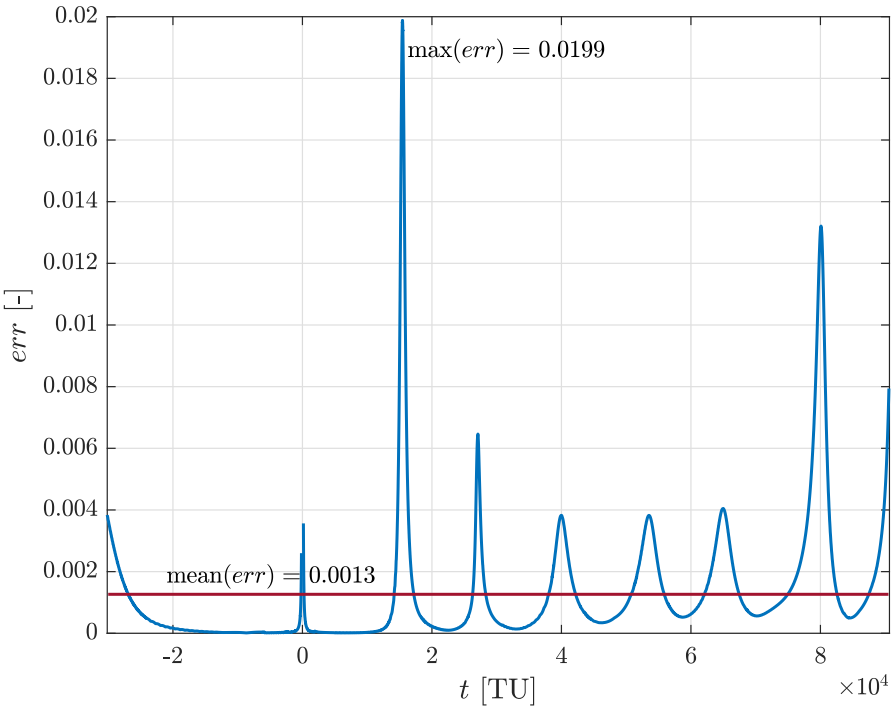

Figure 5.5: L^2-norm and mean value of the approximation error for $\delta t_0 = 0.25$ days.

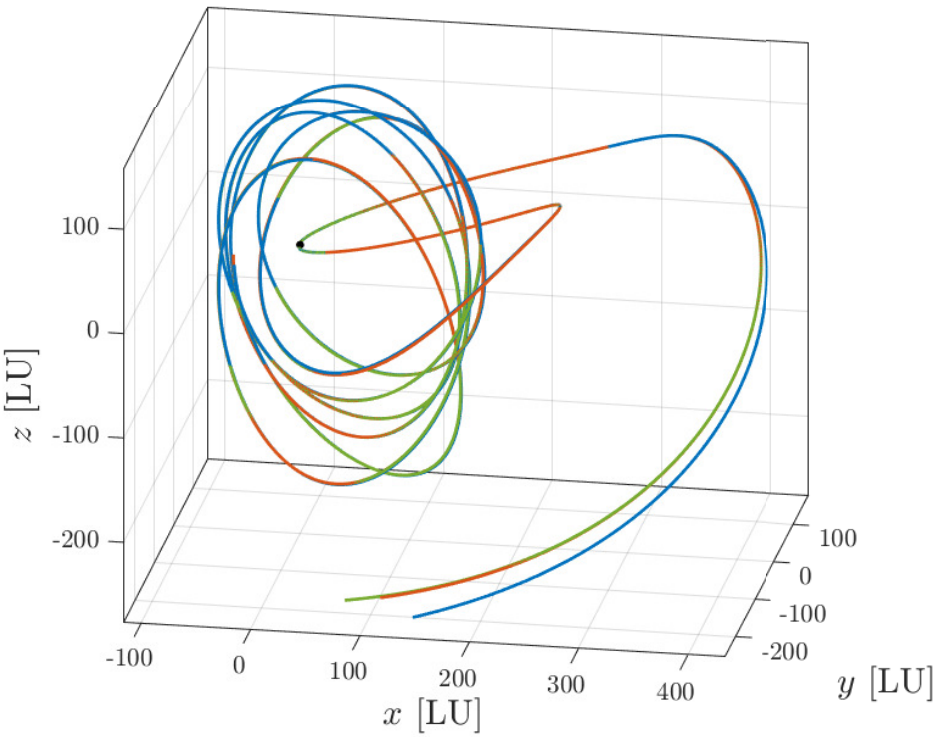

Figure 5.6: Trajectories in EME2000 for $\varphi_{t_0}^t$ (blue), $\varphi_{t_0+\delta t_0}^t$ (green), and $\tilde{\varphi}_{t_0+\delta t_0}^t$ (orange) for $\delta t_0 = 0.25$ days.

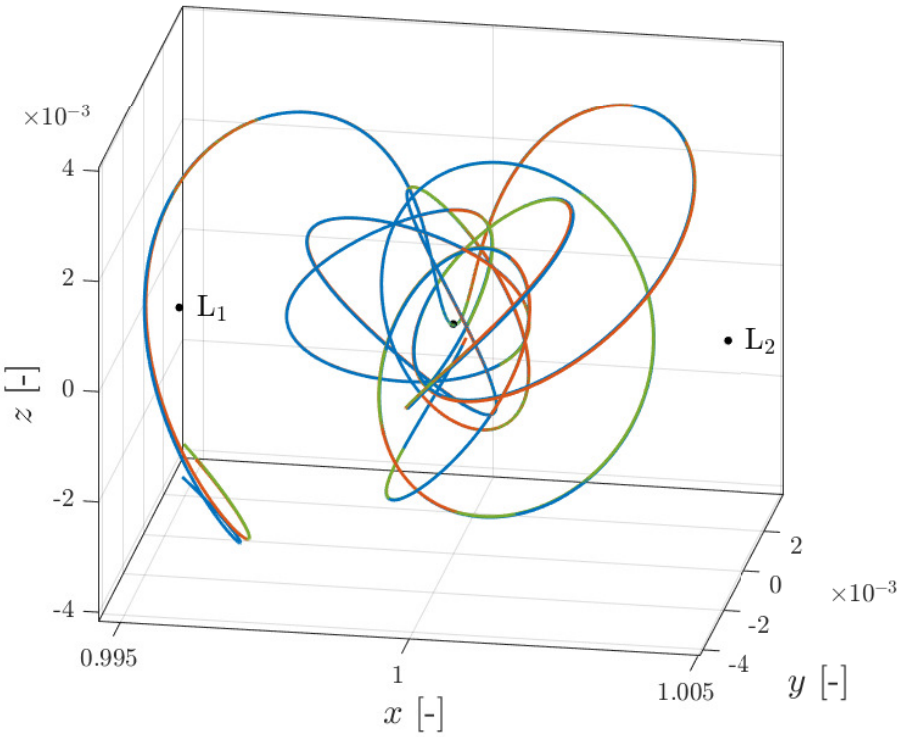

Figure 5.7: Trajectories in RPF for $\varphi_{t_0}^t$ (blue), $\varphi_{t_0+\delta t_0}^t$ (green), and $\tilde{\varphi}_{t_0+\delta t_0}^t$ (orange) for $\delta t_0 = 0.25$ days.

5.2 Fixed orbital elements in varying reference frame

The results produced following the rationale explained in Section 4.3.2 will now be presented. As before, the region has been investigated for capture epochs one day apart from each other. In particular the stopping criteria resulted in a observation window of [0, 9] days. As can be appreciated in Figure 5.8, in this analysis the algorithm was stopped because of the region being completely enclosed within the Capture Set.

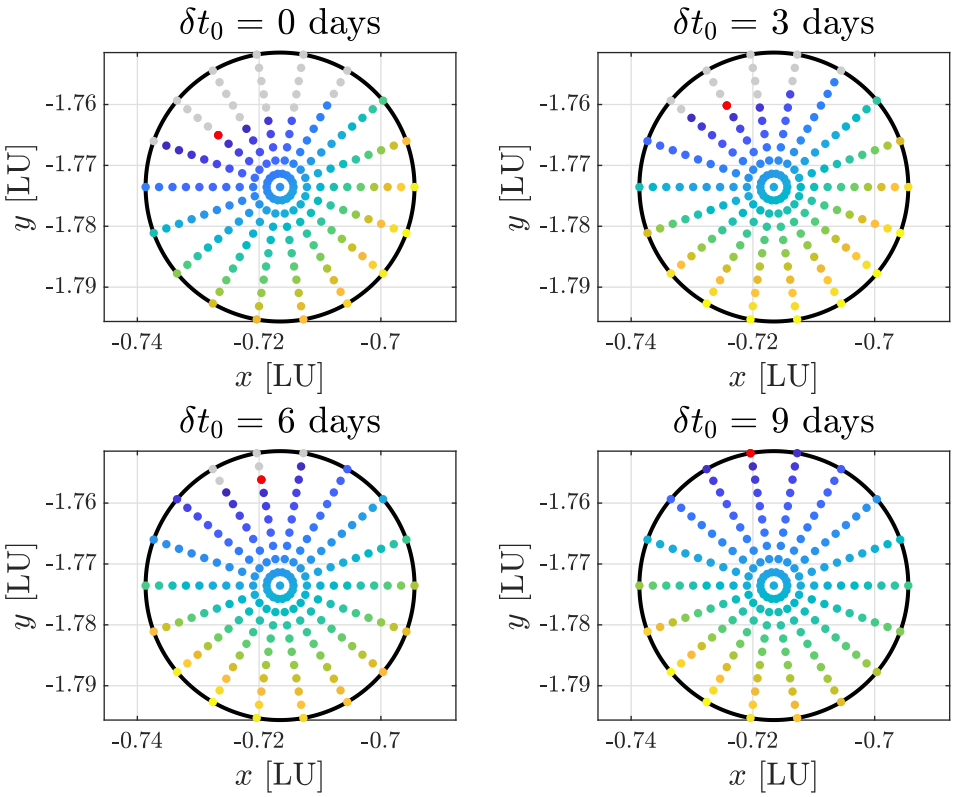

Figure 5.8: Capture Sets at different δt_0. $\mathcal{S}_{\min}$ shown in red, computational grid in grey.

Now that the initial osculating orbital elements are defined in the *time-local* RTN@$(t_0 + \delta t_0)$ reference frame, the region is not only able to stay within the Capture Set for a longer time span, it also becomes completely enclosed by the WSB. In fact, it can be observed that:

$$\mathcal{R}_{\mathcal{C}}(\delta t_0^{(i+1)}) > \mathcal{R}_{\mathcal{C}}(\delta t_0^{(i)})$$

Since the region is now observed for a longer time span, it is interesting to evaluate how $\mathcal{S}$ evolves due to the variations in the capture epoch. Figure 5.9 reports the evolution of average and minimum Stability Index within the region: both curves monotonically decrease over time. To better understand how such quantities vary under the effect of different capture epochs, a second analysis was conducted accounting for a larger region ($r = 150$km) and δt_0 covering a time span of $[-42, 42]$ days (to reduce the computational burden a non-uniform discretization was selected). The corresponding results are reported in Figure 5.10. In both images the iterations where the region completely belongs to the Capture Set are marked with a cross. It can be noted that in the neighbourhood of $\delta t_0 = 0$ (i.e. the nominal condition) the two curves are very close, meaning that within the region the initial conditions resulting in capture orbits exhibit similar behaviours. Therefore, in such time interval the trajectories are the most *robust* to variations in the initial state vector.

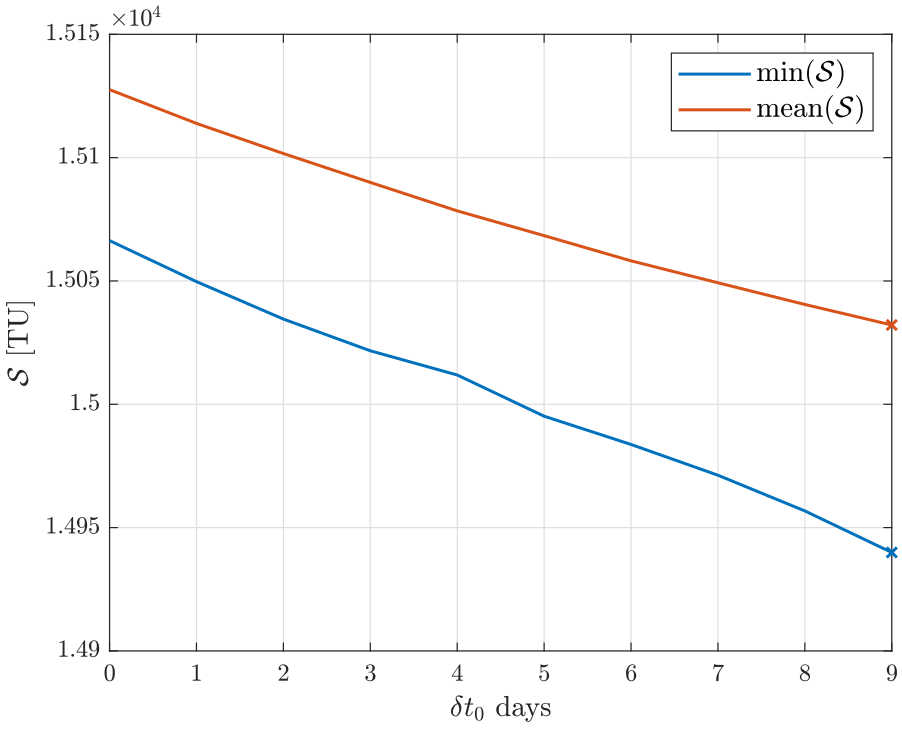

Figure 5.9: Minimum and average Stability Index at different δt_0.

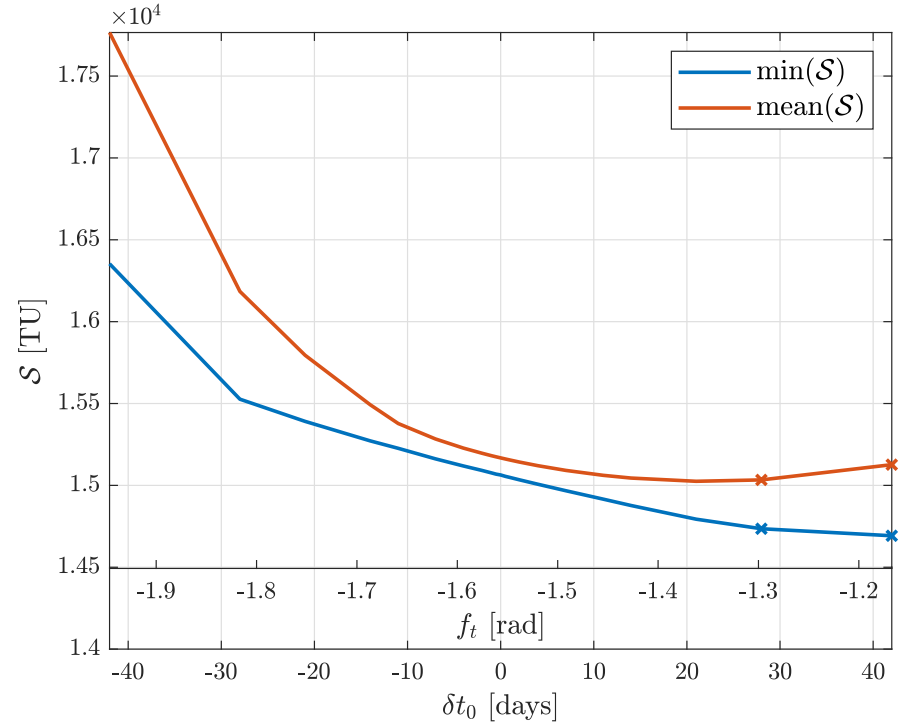

Figure 5.10: Minimum and average Stability Index for the extended analysis.

5.2.1 Validation of the fixed-varying approximation

Exploiting Equation 4.3 it is possible to approximate the flow generated by the initial conditions subjected to infinitesimal variations in capture epoch and initial state vector. For consistency with the analysis performed in Section 5.1, the variation in the capture epoch has been set as $\delta t_0 = 0.25$ days.
Following the same rationale as before, the approximation can be performed both from the "left" and "right" extremes. The maximum and average approximation errors at different capture epochs can therefore be computed and are reported in Figure 5.11.

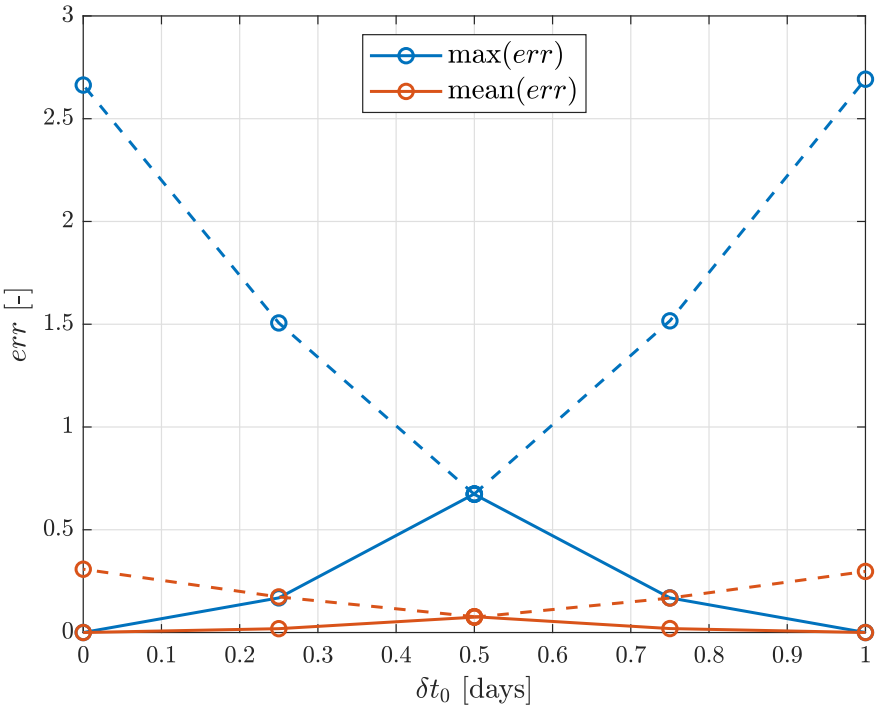

Figure 5.11: Compensated estimation error at different δt_0. The dashed lines represent the non-compensated errors of the estimation.

It can be noticed that the maximum value of the error is significantly larger than the one found in Figure 5.5 for the previous analysis. Because of such large errors, this approximation should be carefully considered and studied, since it appears to be extremely sensitive to changes in the capture epoch.

Figure 5.12 shows the comparison between the *nominal* flows $\varphi^t_{t_0}$ and $\varphi^t_{t_0+\delta t_0}$ and the approximation of the latter $\tilde{\varphi}^t_{t_0+\delta t_0}$ originating from the initial condition at the centre of the region. Figure 5.13 reports the L^2-norm of the associated error, computed as per Equation 5.1.
Figures 5.14 and 5.15 report the trajectories generated by the exact flows $\varphi^t_{t_0}$ and $\varphi^t_{t_0+\delta t_0}$ as well as by the approximated one $\tilde{\varphi}^t_{t_0+\delta t_0}$. As expected, the accuracy of the approximation has worsen with respect to the one reported in the previous section. In particular it is possible to notice that the current investigation produces significantly larger discrepancies than the previous one, especially when considering time instants near the escape point. However, due to the mean error being relatively small (2%) the trajectory computed does represent a good estimation of the nominal flow on the majority of the integration period.

The results obtained for the limiting case of $\delta t_0 = 0.5$ days are reported in Appendix B.

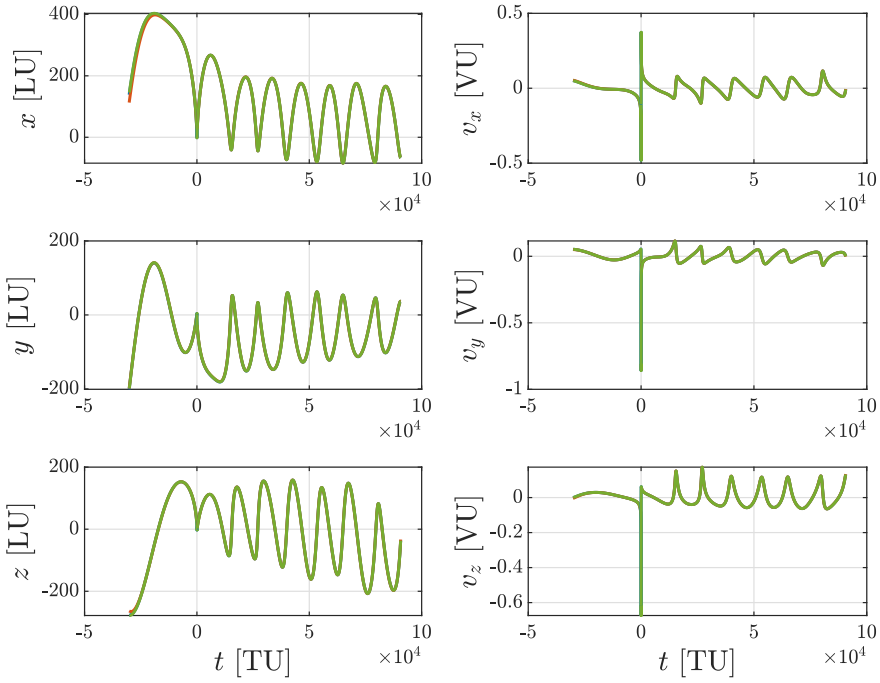

Figure 5.12: State vectors for $\varphi^t_{t_0}$ (blue), $\varphi^t_{t_0+\delta t_0}$ (green), and $\tilde{\varphi}^t_{t_0+\delta t_0}$ (orange) for $\delta t_0 = 0.25$ days.

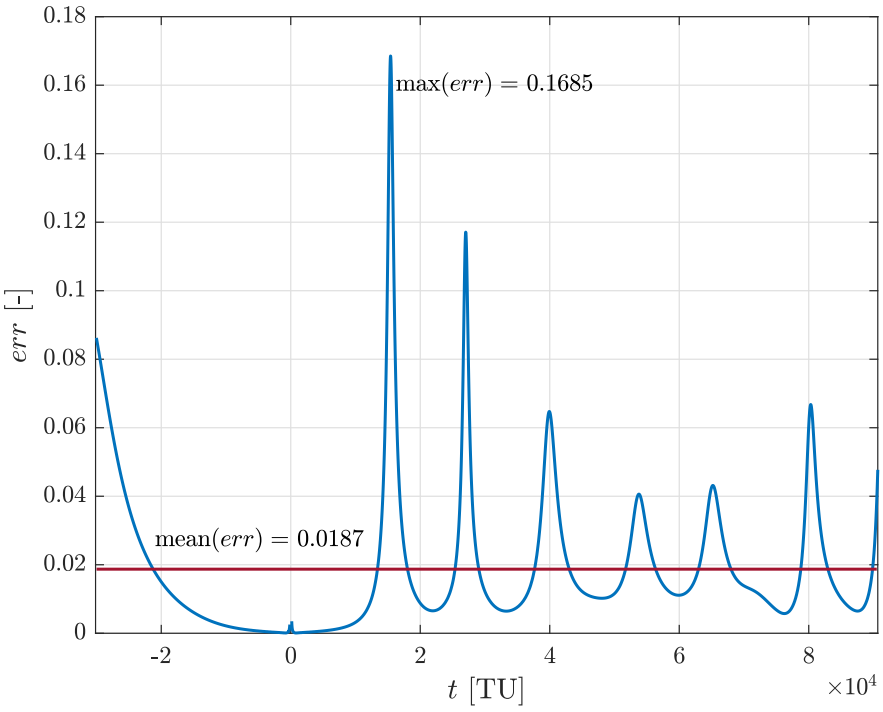

Figure 5.13: L^2-norm and mean value of the approximation error for $\delta t_0 = 0.25$ days.

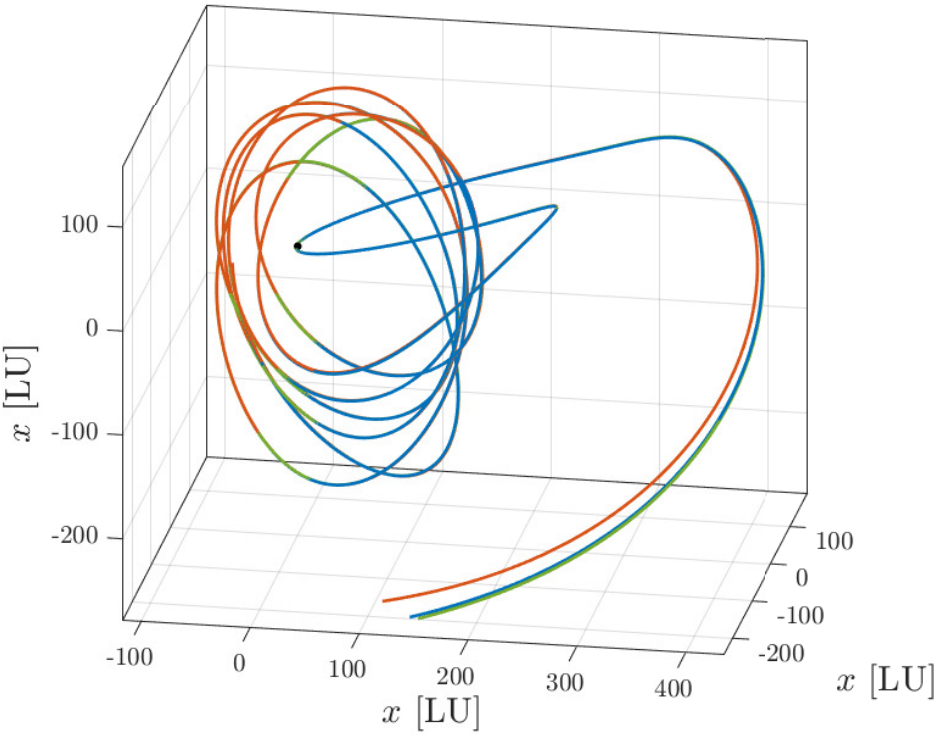

Figure 5.14: Trajectories in EME2000 for $\varphi^t_{t_0}$ (blue), $\varphi^t_{t_0+\delta t_0}$ (green), and $\tilde{\varphi}^t_{t_0+\delta t_0}$ (orange) for $\delta t_0 = 0.25$ days.

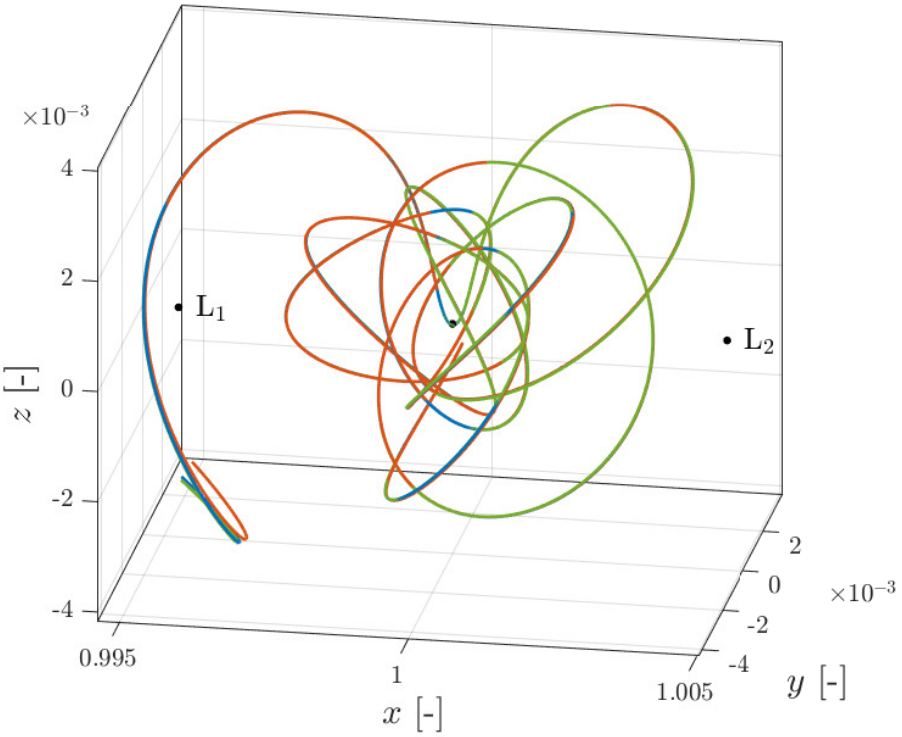

Figure 5.15: Trajectories in RPF for $\varphi^t_{t_0}$ (blue), $\varphi^t_{t_0+\delta t_0}$ (green), and $\tilde{\varphi}^t_{t_0+\delta t_0}$ (orange) for $\delta t_0 = 0.25$ days.

5.3 Varying orbital elements in varying reference frame

Considering Figures 5.9 and 5.10 it was stated that the iterations where the region is completely enclosed within the Capture Set are signaled with cross marker. In particular, it is because of these specific iterations that the procedure described in Section 4.3.3 was conceptualized. Such analysis aims at answering the question:

To what extent can the most regular initial conditions in the Capture Set be tracked?

The results obtained exploiting the algorithm used to tackle such question are reported in Figure 5.16. It is worth noticing that the region dynamically evolves along the Capture Set for approximately 300 days (evaluations have been performed with a constant step size of 2 days), and it is particularly interesting to relate such propagation to the true anomaly of the target planet. In fact, observing the secondary x-axis present in Figure 5.16 it can be verified that such time span corresponds to the angular span covering $f_t = [-\pi/2, \pi/2]$ and in particular that $\mathcal{S}$ presents a minimum in the interval $t_f = [0, \pi/2]$, in accordance with the literature results reported in Section 3.3.2.

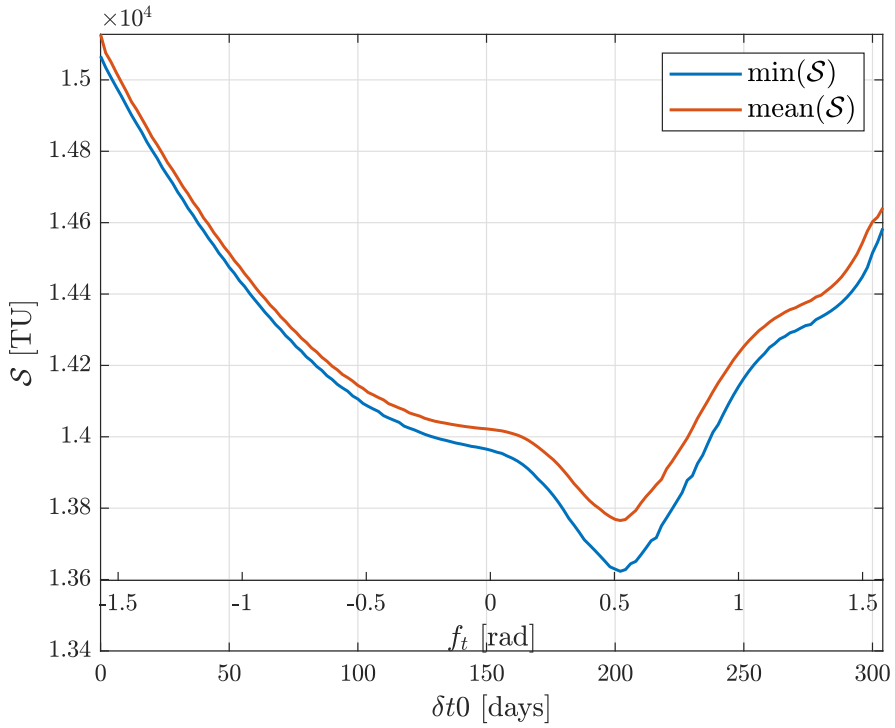

Figure 5.16: Minimum and average Stability Index evolution in time.

It is also worth mentioning that the algorithm collected data up to $\delta t_0 = 322$ days, however the interval [304, 322] has been neglected in Figure 5.16 due to the corresponding behaviour exhibited by the region. A complete representation of the time span is given in Appendix B.

It is also interesting to observe the path traced by the region whilst evolving in time along with the Capture Set, as reported in Figures 5.17 and 5.18. It is interesting to notice that the minimum in the Stability Index where $\mathcal{S}$ changes behaviour is associated with a reversal of the direction followed by the region.

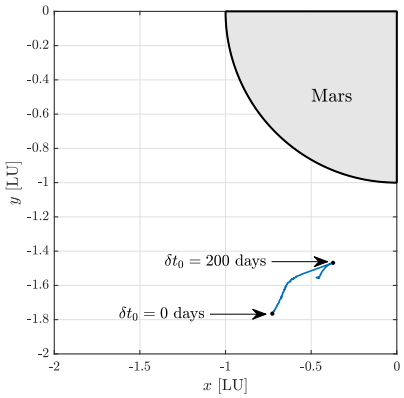

Figure 5.17: Path traced by the region during the algorithmic propagation.

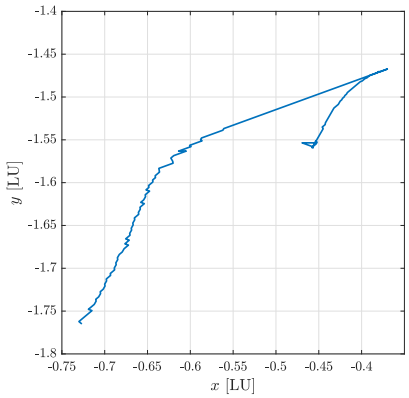

Figure 5.18: Detailed view of the path traced by the region.

5.3.1 Validation of the varying-varying approximation

Making use of Equation 4.5 it is possible to approximate the flow generated by the initial conditions subjected to variations in the capture epoch and initial state vector. As done for the previous analyses, the perturbation on the capture epoch has been set to $\delta t_0 = 0.25$ days. Consistently with the previous analyses, the approximation can be performed from both extremes of the time interval and therefore considering different nominal flows depending on the query point to be approximated. In particular, Figure 5.19 reports the maximum and average approximation error for different capture epochs. However, it is important to stress that within the present section the time interval considered does not coincide with the one computed with the algorithm and presented in Section 5.3. In particular, whilst the previous interval spanned over two days, the current one covers only one day. Moreover, it is worth mentioning that in the present case also the translation of the region has to be accounted for (represented by the term $\delta\mathbf{x}_0^{(\mathrm{T})}$ in Equation 4.5). To this end, the displacement has been linearly interpolated between the data available for the "left" and "right" extremes of the time window considered.

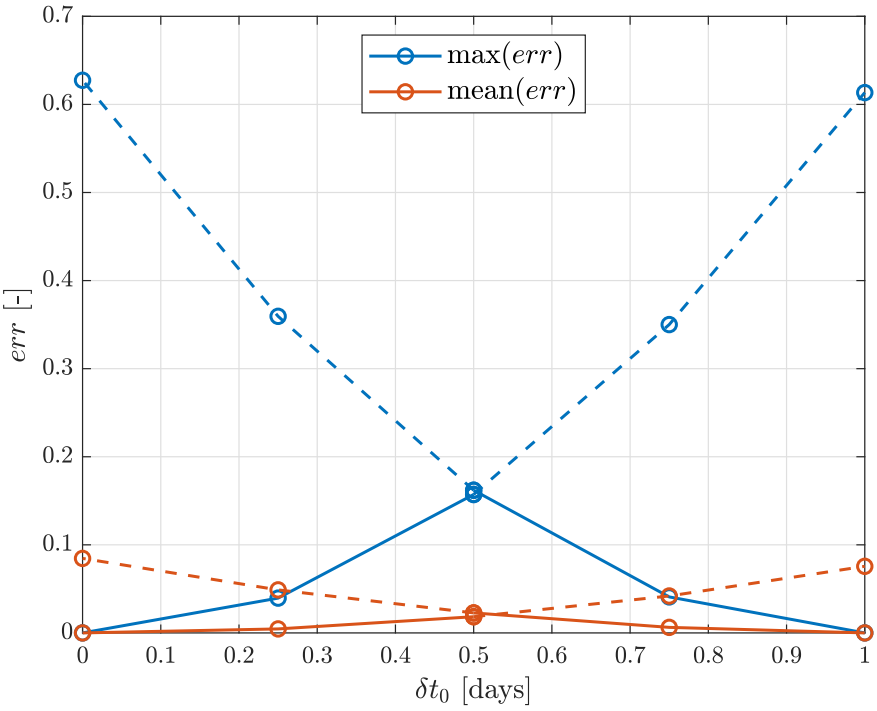

Figure 5.19: Compensated estimation error at different δt_0. The dashed lines represent the non-compensated errors of the estimation.

When analysing the results of the approximation, Figure 5.20 shows the comparison between the *nominal* flows $\varphi^t_{t_0}$ and $\varphi^t_{t_0+\delta t_0}$ and the approximation of the latter $\tilde{\varphi}^t_{t_0+\delta t_0}$ originating from the initial condition at the centre of the region. Figure 5.21 reports the L^2-norm of the associated approximation error computed by means of Equation 5.1.

Figures 5.22 and 5.23 report the trajectories generated by the aforementioned flows. It is interesting to notice that the accuracy of the approximation has increased with respect to the fixed-varying case previously analysed. A possible explanation behind such phenomenon might be that the rigid motion of the region onto the osculating plane is compensating the inaccuracies introduced by the rotation of the reference frame. In fact, the accuracy of the approximation is comparable to the one obtained for the fixed-fixed case reported in Section 5.1.

The results obtained for the limiting case of $\delta t_0 = 0.5$ days are reported in Appendix B.

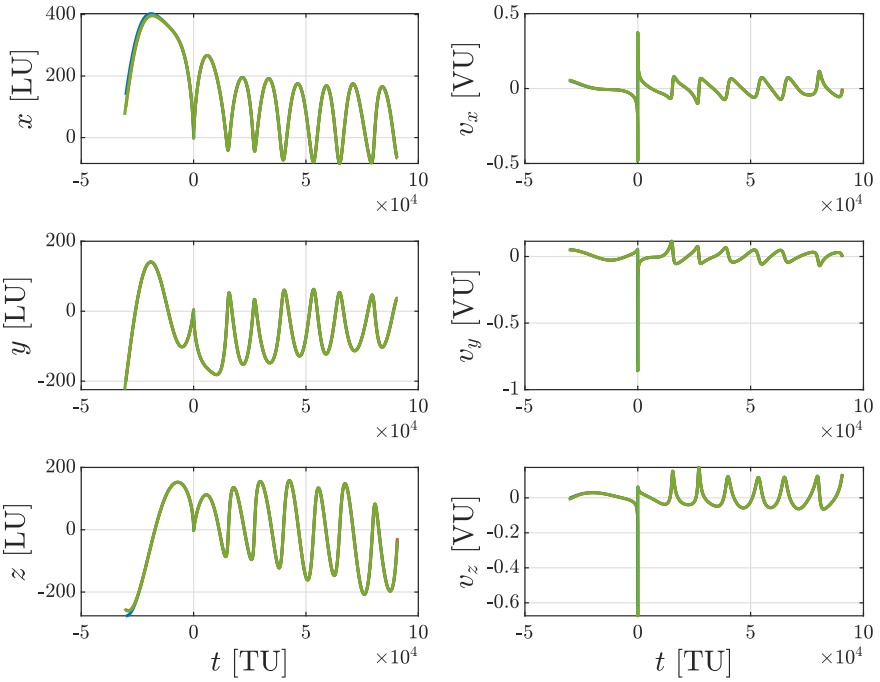

Figure 5.20: State vectors for $\varphi_{t_0}^t$ (blue), $\varphi_{t_0+\delta t_0}^t$ (green), and $\tilde{\varphi}_{t_0+\delta t_0}^t$ (orange) for $\delta t_0 = 0.25$ days.

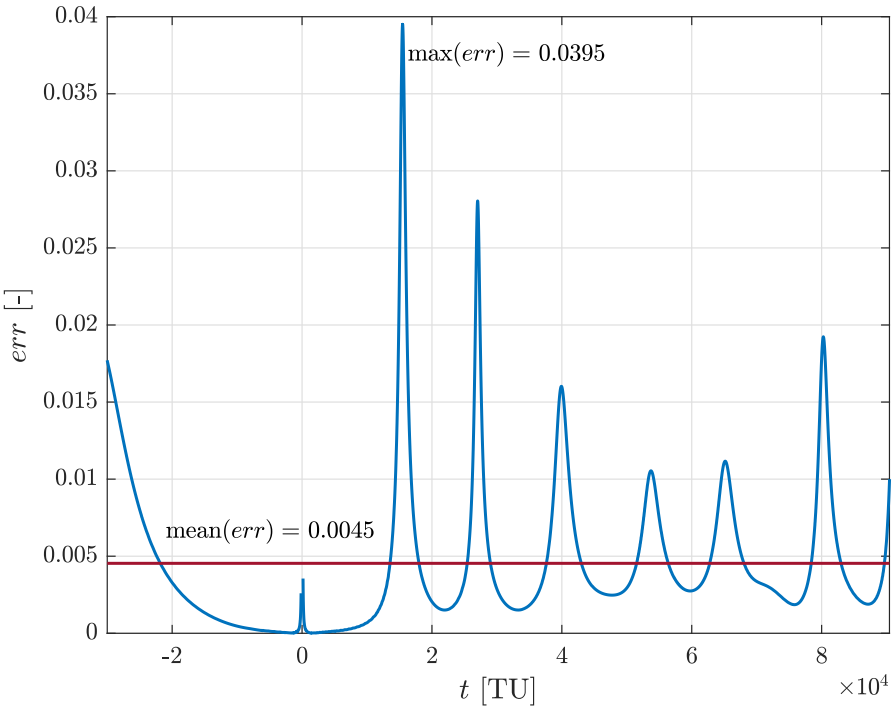

Figure 5.21: L^2-norm and mean value of the approximation error for $\delta t_0 = 0.25$ days.

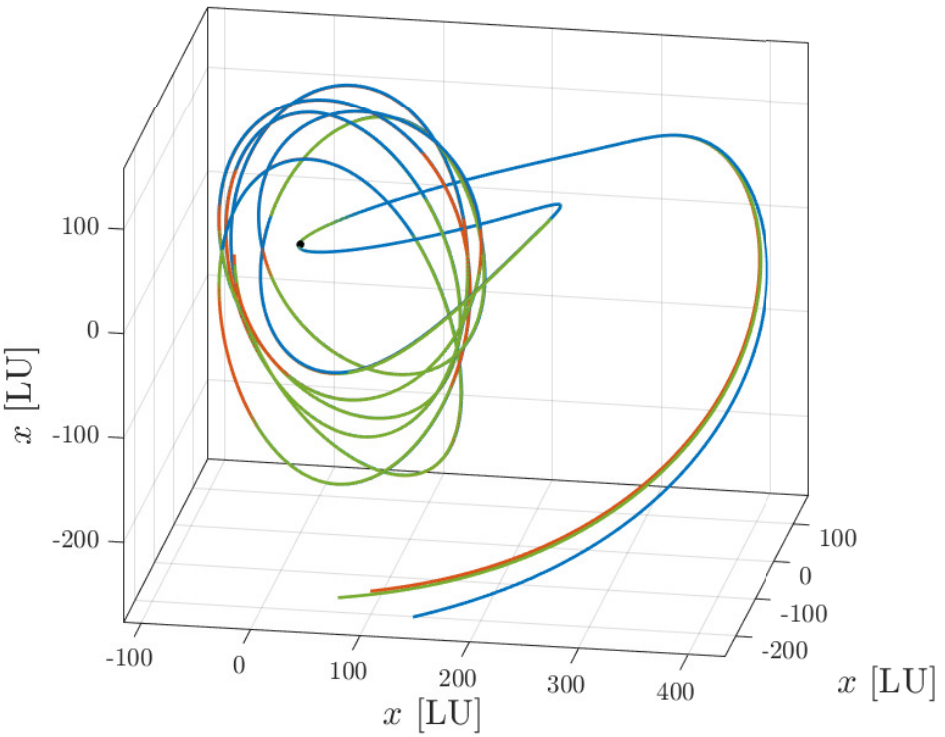

Figure 5.22: Trajectories in EME2000 for $\varphi_{t_0}^t$ (blue), $\varphi_{t_0+\delta t_0}^t$ (green), and $\tilde{\varphi}_{t_0+\delta t_0}^t$ (orange) for $\delta t_0 = 0.25$ days.

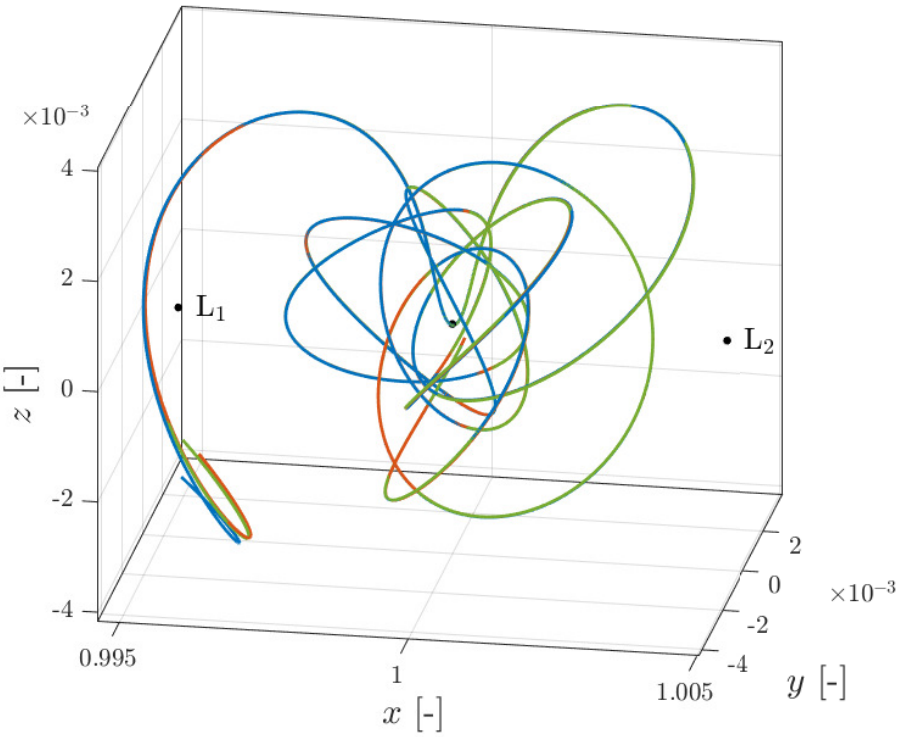

Figure 5.23: Trajectories in RPF for $\varphi_{t_0}^t$ (blue), $\varphi_{t_0+\delta t_0}^t$ (green), and $\tilde{\varphi}_{t_0+\delta t_0}^t$ (orange) for $\delta t_0 = 0.25$ days.

5.4 Additional considerations on the Capture Set

Since the definition of the region of interest revolves around the Stability Index $\mathcal{S}$, it is worth investigating how such parameter evolves and behaves inside a small region of space. An interesting feature is the relationship between the Capture Set and its "edge" within the region studied, here referred to as Capture Boundary. In particular, it is worth understanding how the Stability Index behaves with respect to the boundary. To this end it is convenient to study the shape and distribution of isolines (or contour lines) within the region. Here, in order to have results showing a sufficient accuracy, the same $r = 150$ km circumference introduced in Section 5.2 has been used. If such lines were to be parallel to the boundary, one could conclude that the gradient of the Stability Index would be orthogonal to the boundary itself. However, no particular connection between Capture Boundary and isolines appears to exist, as shown in Figure 5.24.

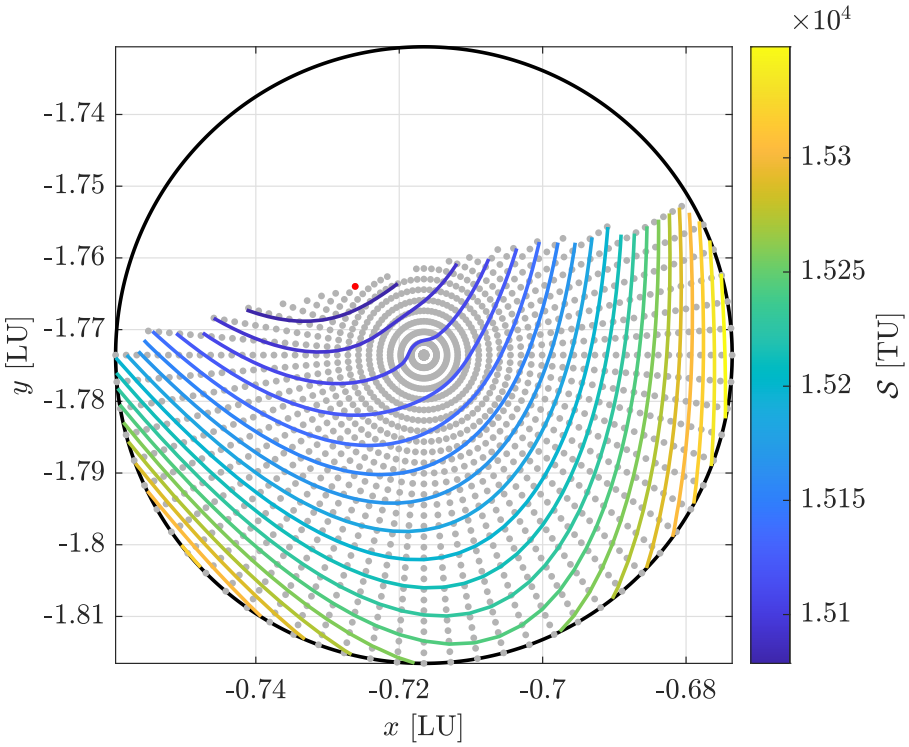

Figure 5.24: Stability Index isolines within the region for $\delta t_0 = 0$ days. $\mathcal{S}_{\text{min}}$ shown in red.

It is worth mentioning that the behaviour of the contour lines in proximity of the centre of the region is highly affected by numerical noise. In fact, an interpolation scheme has to be used in order to compute the isolines in between the available data points. This consideration explains the weird bent performed by the isoline approaching the centre of the region in Figure 5.24. In fact, to further confirm this consideration, it can be noticed that no geometry justifying such bent appear when analysing a 3D plot of the data points, as reported in Figure 5.25.

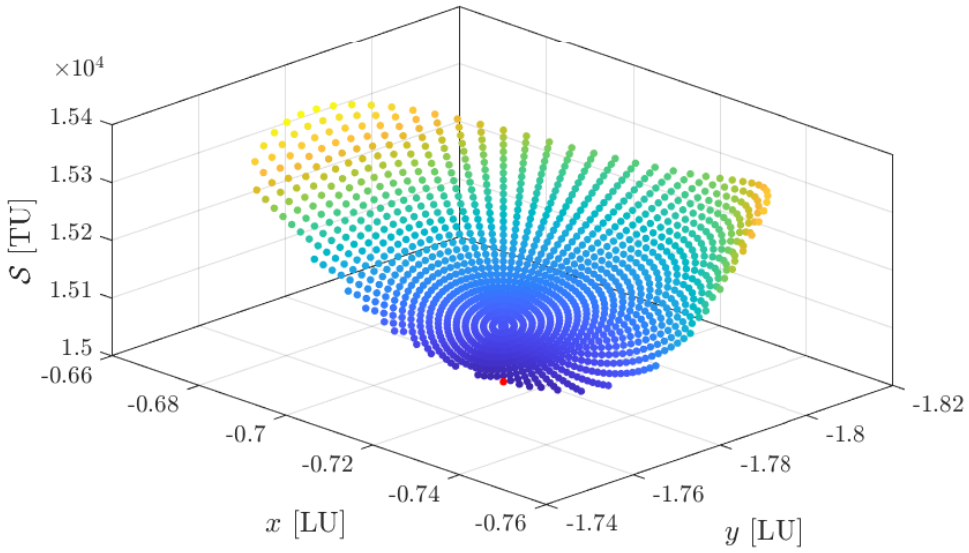

Figure 5.25: 3D scatter plot of the available data points. $\mathcal{S}_{\text{min}}$ shown in red.

Section 4.1 explained the reason behind the location of the minimum Stability Index. A visual representation of such explanation can be appreciated in Figures 5.26 and 5.27. Exploiting the Delaunay triangulation to avoid the numerical noise associated with the interpolation lying behind other representation techniques, two surfaces are defined: the one on top represents the surface described by the Stability Index within the forward-Stable Set $\mathcal{W}_6$ whilst the flat one at the basis represents the portion belonging to the backward-Unstable Set $\mathcal{X}_{-1}$. Since the Capture Set is constructed as the intersection of the two aforementioned sets, it is easy to observe how $\mathcal{X}_{-1}$ governs the definition of the Capture Boundary.

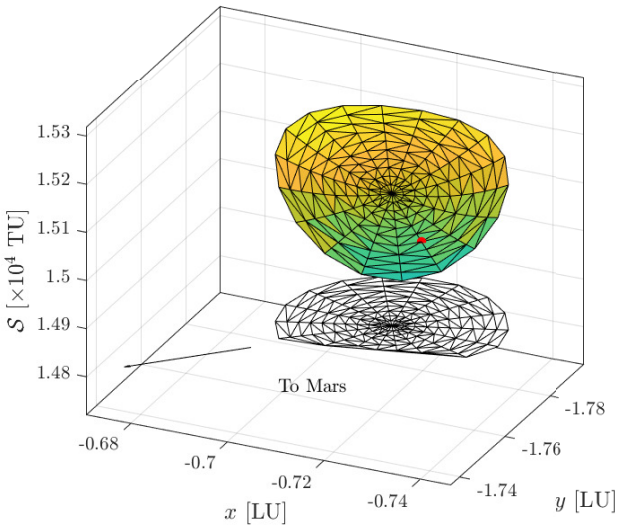

Figure 5.26: Front-view of $\mathcal{W}_6$ and $\mathcal{X}_{-1}$ for $\delta t_0 = 0$ days. $\mathcal{S}_{\min} \in \mathcal{C}^6_{-1}$ shown in red.

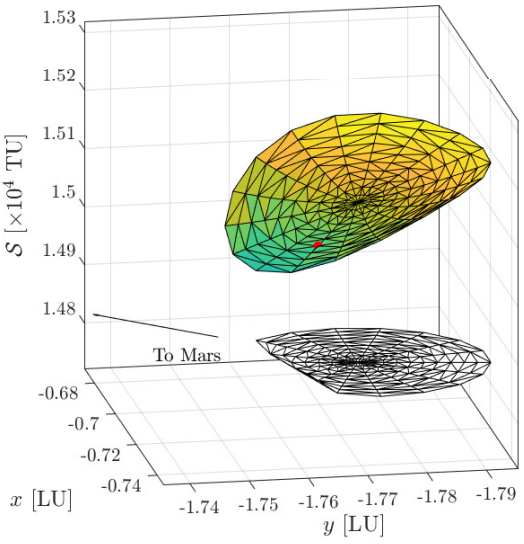

Figure 5.27: Side-view of $\mathcal{W}_6$ and $\mathcal{X}_{-1}$ for $\delta t_0 = 0$ days. $\mathcal{S}_{\min} \in \mathcal{C}^6_{-1}$ shown in red.

However, a more comprehensive investigation reveals that the Capture Boundary is not always completely governed by the backward-Unstable Set. In fact, by applying the same rationale for $\delta t_0 = 200$ days, significantly different surfaces can be appreciated, as shown in Figures 5.28 and 5.29.

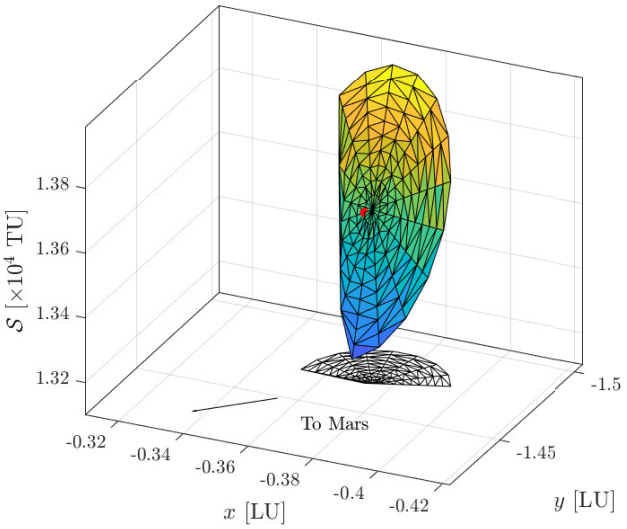

Figure 5.28: Front-view of $\mathcal{W}_6$ and $\mathcal{X}_{-1}$ for $\delta t_0 = 200$ days. $\mathcal{S}_{\min} \in \mathcal{C}^6_{-1}$ shown in red.

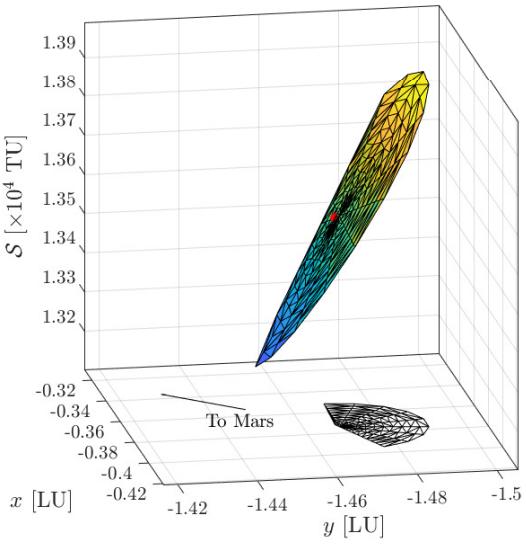

Figure 5.29: Side-view of $\mathcal{W}_6$ and $\mathcal{X}_{-1}$ for $\delta t_0 = 200$ days. $\mathcal{S}_{\min} \in \mathcal{C}^6_{-1}$ shown in red.

Although the behaviour reported is qualitatively different depending on the capture epoch considered, it is interesting to notice that the consideration made in Section 4.1 is always valid. In fact, it can be observed that the initial condition associated with the minimum Stability Index lies on the portion of the Capture Boundary governed by the backward-Unstable Set for the whole 322 days span analysed.

5.5 Stroboscopic Strainline definition of the Capture Boundary

When constructing the Capture Set about a selected planet, the results span over characteristic lengths so large that no a priori assumption about the local behaviour can be made. For instance, no knowledge on the small-scale geometry of the Capture Boundary is available. For example, one could ask the following question:

Is the Capture Boundary well represented by stroboscopic strainlines?

As explained in Section 4.4 two possible boundary conditions for the integration of the Cauchy problem of Equation 2.29 are available. Here, both points have been considered, as shown in Figure 5.30.

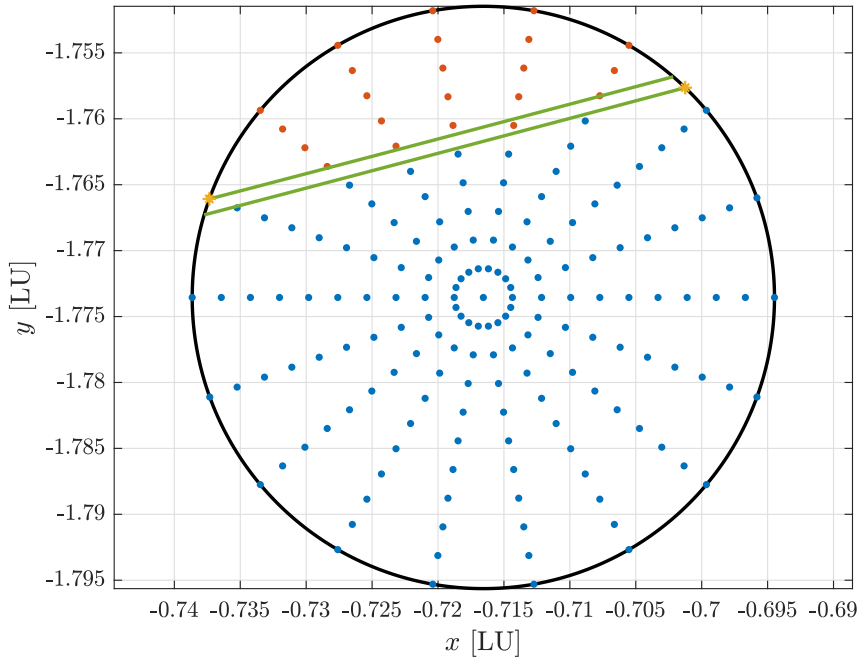

Figure 5.30: Strainlines (green) associated to $\mathcal{C}^6_{-1}$ (blue) at t_0. $\mathcal{W}_{-1}$ shown in orange.

It is interesting to notice that two different strainlines emerge from the integration and that they appear to be intersecting the sets. This behaviour can be explained when considering the classification criteria given in Section 3.2.1. In fact, such algorithmic definition can sometimes cause the loss of a portion of the dynamical behaviour, meaning that one criterion could be triggered resulting in the associated classification, even though the overall behaviour could be of a different nature. In this case for example, it is possible for one trajectory that escapes the target to briefly trigger the revolution criterion. The introduction of strainlines represents an attempt at identifying the WSB by means of mathematical tools accounting for the dynamics of the ballistic capture phenomenon [21, 23].
By inspection it is possible to verify that initial conditions situated "just below" the *lower* strainline result in ballistic capture trajectories, whilst those lying "just above" the *upper* strainline do not generate capture. In particular, because of what has been said in Section 4.1, it can be verified that orbits that do not generate capture are stable in backward time (capture requires backward escape, as per Equation 3.14). Sample trajectories reporting such results are shown in Figure 5.31.

It can be noticed that all trajectories depicted in blue belong to $\mathcal{X}_{-1}$ (and therefore to $\mathcal{C}^6_{-1}$), all those coloured in orange belong to $\mathcal{W}_{-1}$, whilst the green trajectories (initial conditions located in between the strainlines computed) are not associated with one unique behaviour. From these considerations it is possible to infer that the WSB is bounded within the portion of space delimited by the strainlines computed. This in turn means that initial conditions in proximity of such portion of the state space are likely to manifest larger changes in flow under the effect of small variations δt_0 and $\delta \mathbf{x}_0$. It can be shown that such trajectories generate maximum approximation errors that are larger than those presented by other points of the region. An example of such behaviour can be observed in Figure 5.32, where the varying-varying analysis is considered, the error computed greatly exceeds the one reported in Section 5.3 for the centre

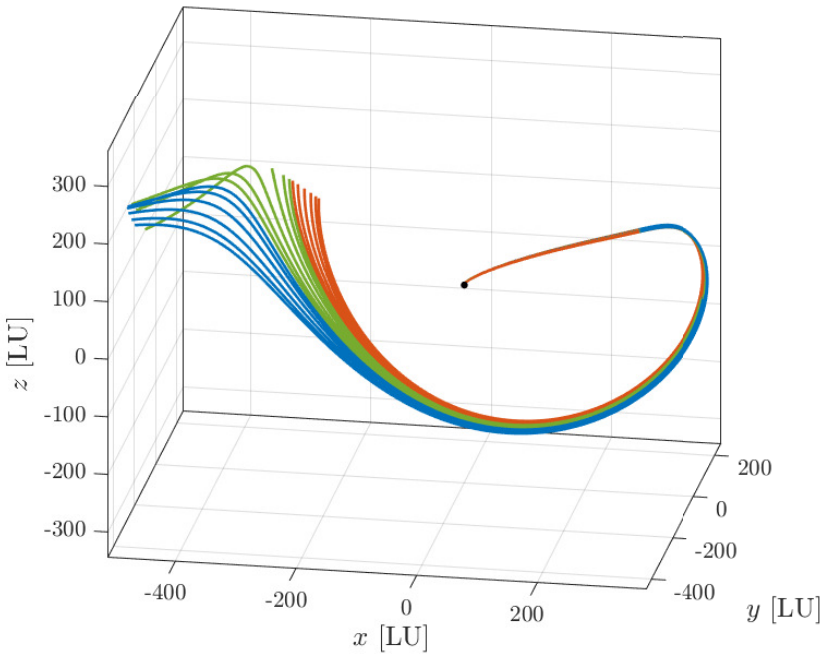

Figure 5.31: Pre-capture trajectories generated from initial conditions "below" the lower stainline (blue), "above" the upper strainline (orange), and "between" the strainlines (green).

of the region. In particular, although the average error is small in both images, the one now being considered manifests a large peak in the pre-capture arc, which is consistent with the aforementioned considerations.

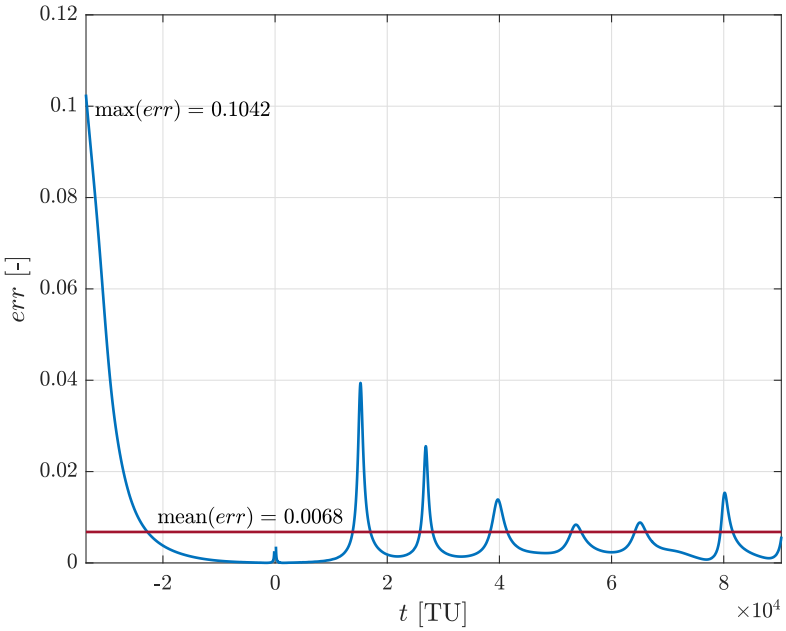

Figure 5.32: Approximation error in proximity of the strainlines.

Chapter 6

Conclusions and Recommendations

6.1 Conclusions

As introduced in Section 1.2, this thesis aims at answering the following research question:

How do particular portions of a Capture Set evolve under the influence of variations in the capture epoch?

The answer to such question has been given under different types of analyses, considering different types of variations. The results presented show that when considering a region of the Capture Set defined by means of quantities found in literature, it is possible to estimate and predict its evolution in time. In particular, it can be concluded that the approximations defined are able to qualitatively describe the exact trajectories for a good portion of their time history, even when large peak errors are observed.

In particular, it has been shown that given a time interval of interest and the Capture Sets at the extremes of such interval, it is possible to approximate the *continuous* evolution in time of the region analysed. Such estimation can therefore be exploited in the trajectory design of low-energy transfers in order to preliminary identify a very narrow time-window of interest as well as opening the possibility to preemptively estimate the effect of uncertainties in the critical phases of the capture phenomenon. This methodology could be applied on board of autonomous satellites in order to accelerate the high-fidelity re-computation of highly regular ballistic capture orbits, so as to verify if different capture epoch and state vector at capture should be targeted.

Additionally, to better understand the small-scale behaviour of ballistic Capture Sets and orbits, also a detailed analysis has been conducted by means of stroboscopic strainlines. This in turn showed that although strainlines represent a useful mathematical tool to identify underlying dynamical features, they are not able to return an exact representation of the WSB. A particular feature exhibited by strainlines is the fact that by solving the associated Cauchy problem results in two different strainlines, each corresponding to one of the two different boundary conditions identified. In fact, if they were able to exactly identifying the WSB, it would be reasonable to conclude that the same curve would be identified, independently of the boundary condition considered. However, they are able to define a narrow region of the state space where it is reasonable to conclude that the WSB is located.

6.2 Recommendations

Based on the results of this work, future developments and efforts are required. In fact:

- Although the techniques developed allow to qualitatively estimate the flow originating from any generic perturbation, no information has been obtained on how the perturbed trajectory behaves. Therefore, future developments could aim at predicting which initial conditions will generate perturbed flows belonging to the Capture Set as well as refining the estimation, for example exploiting differential correction algorithms.
- The techniques developed in this thesis could be used to define a variable stepsize in the propagation and study of the dynamical evolution of the Capture Set.
- It is worth further analysing the reason behind the excessive error on the initial portion of the approximation (i.e. $|t| \lesssim 150$ TU) and if corrections of such behaviour are possible.
- The different behaviour exhibited by the estimation error across the different types of analyses conducted should be further investigated.
- The limits of applicability of the assumptions under which the approximation is defined should be further investigated.
- The correlation between peaks in the approximation error and the evolution of the state vector in time should be carefully studied.
- Although in this thesis new interesting results in the position of the WSB were found, a more comprehensive and exhaustive study should be conducted so as to clarify how LCS and strainlines correlate to it.
- It is worth investigating what is the real small-scale behaviour of the WSB (and also of the Capture Boundary). In particular, it might be interesting to study if it is represented by a smooth and differentiable surface.

Appendices

Appendix A

Additional Derivatives

In this appendix the expression of the right hand side of Equation 2.19 will be given. Recalling the symmetry property of the desired matrix and the condition of a vanishing sum of the diagonal elements, it is possible to reduce the number of independent components to be evaluated from 9 to 5 [22].

$$
\begin{aligned}
\frac{\partial \ddot{x}_{nm}}{\partial x} &\overset{(m=0)}{=} \frac{1}{2}\frac{\mu_t}{R^3}\left[(+C_{n0}V_{n+2,2}) - \frac{(n+2)!}{n!}(+C_{n0}V_{n+2,0})\right] \\
&\overset{(m=1)}{=} \frac{1}{4}\frac{\mu_t}{R^3}\Bigg[(+C_{n1}V_{n+2,3} + S_{n1}W_{n+2,3}) \\
&\qquad + \frac{(n+1)!}{(n-1)!}(-3C_{n1}V_{n+2,1} - S_{n1}W_{n+2,1})\Bigg] \\
&\overset{(m>1)}{=} \frac{1}{4}\frac{\mu_t}{R^3}\Bigg[(+C_{nm}V_{n+2,m+2} + S_{nm}W_{n+2,m+2}) \\
&\qquad + 2\frac{(n-m+2)!}{(n-m)!}(-C_{nm}V_{n+2,m} - S_{nm}W_{n+2,m}) \\
&\qquad + \frac{(n-m+4)!}{(n-m)!}(+C_{nm}V_{n+2,m-2} + S_{nm}W_{n+2,m-2})\Bigg]
\end{aligned}
$$

$$
\begin{aligned}
\frac{\partial \ddot{x}_{nm}}{\partial y} &\overset{(m=0)}{=} \frac{1}{2}\frac{\mu_t}{R^3}\left[(+C_{n0}W_{n+2,2})\right] \\
&\overset{(m=1)}{=} \frac{1}{4}\frac{\mu_t}{R^3}\Bigg[(+C_{n1}W_{n+2,3} - S_{n1}V_{n+2,3}) \\
&\qquad + \frac{(n+1)!}{(n-1)!}(-C_{n1}W_{n+2,1} - S_{n1}V_{n+2,1})\Bigg] \\
&\overset{(m>1)}{=} \frac{1}{4}\frac{\mu_t}{R^3}\Bigg[(+C_{nm}W_{n+2,m+2} - S_{nm}V_{n+2,m+2}) \\
&\qquad + \frac{(n-m+4)!}{(n-m)!}(-C_{nm}W_{n+2,m-2} + S_{nm}W_{n+2,m-2})\Bigg]
\end{aligned}
$$

$$\begin{aligned}\frac{\partial \ddot{x}_{nm}}{\partial z} &\overset{(m=0)}{=} \frac{\mu_t}{R^3}\left[(n+1)(+C_{n0}V_{n+2,1})\right] \\ &\overset{(m>0)}{=} \frac{\mu_t}{R^3}\left[\frac{n-m+1}{2}(+C_{nm}V_{n+2,m+1}+S_{nm}W_{n+2,m+1})\right. \\ &\quad \left. + \frac{(n-m+3)!}{2(n-m)!}(-C_{nm}V_{n+2,m-1}-S_{nm}W_{n+2,m-1})\right]\end{aligned}$$

$$\begin{aligned}\frac{\partial \ddot{y}_{nm}}{\partial z} &\overset{(m=0)}{=} \frac{\mu_t}{R^3}\left[(n+1)(+C_{n0}W_{n+2,1})\right] \\ &\overset{(m>0)}{=} \frac{\mu_t}{R^3}\left[\frac{n-m+1}{2}(+C_{nm}W_{n+2,m+1}-S_{nm}V_{n+2,m+1})\right. \\ &\quad \left. + \frac{(n-m+3)!}{2(n-m)!}(+C_{nm}W_{n+2,m-1}-S_{nm}V_{n+2,m-1})\right]\end{aligned}$$

$$\frac{\partial \ddot{z}_{nm}}{\partial z} \overset{(m\geq 0)}{=} \frac{\mu_t}{R^3}\left[\frac{(n-m+2)!}{(n-m)!}(+C_{nm}V_{n+2,m}+S_{nm}W_{n+2,m})\right]$$

where $C_{n,m}$ and $S_{n,m}$ are coefficients describing the planet's mass distribution whilst $V_{n,m}$ and $W_{n,m}$ are defined through recurrence relations and depend on the Legendre polynomials used for the spherical harmonics expansion of the gravitational field.

Appendix B

Additional Results

B.1 Additional indexes

When defining the region to investigate, different types of indices have been considered and defined. In particular, apart from the Stability Index $\mathcal{S}$ largely discussed and used throughout the thesis, also the Regularity Coefficient $\overline{\mathcal{S}}$ [10, 21] has been investigated. It is defined as

$$\overline{\mathcal{S}} = \left| \frac{\mathcal{S}}{\mathcal{S}_{2b}} - 1 \right| \tag{B.1}$$

where $\mathcal{S}_{2b}$ represents the period of the osculating Keplerian elliptic orbit, computed as

$$\mathcal{S}_{2b} = 2\pi \left(\frac{r_{p0}}{1 - e_0} \right)^{3/2}$$

Additionally, also a *normalized* Stability Index has been constructed and investigated in this thesis, defined as

$$\tilde{\mathcal{S}} = \left| \frac{\Delta t_n}{S_{2b}} - 1 \right| \tag{B.2}$$

where $\Delta t_n = t_n - t_{n-1}$ is the time interval required to complete the n-th revolution.

However, all the indices defined can be computed for different values of n. Therefore a more complete description would be

$$\mathcal{S} = \mathcal{S}_n, \quad \overline{\mathcal{S}} = \overline{\mathcal{S}}_n, \quad \tilde{\mathcal{S}} = \tilde{\mathcal{S}}_n$$

This in turn means that it could be worth investigating how such indices evolve at different values of n. In particular, it is interesting to define their deviation from zero, computed as

$$\text{dev}(\tilde{\mathcal{S}}) = \sqrt{\frac{1}{N} \sum_{n=1}^{N} (\tilde{\mathcal{S}}_n)^2} \tag{B.3}$$

where $N = 6$ is the maximum number of revolutions considered.

There are now 5 possible minimum points to consider: the minimum of the Stability Index $\mathcal{S}_6$ (used throughout the entirety of the thesis), the minimum of the Regularity Coefficient $\overline{\mathcal{S}}_6$ and its associated minimum deviation, the minimum of the normalized Stability Coefficient $\tilde{\mathcal{S}}_6$

and its associated minimum deviation. Figure B.1 reports the location of the initial condition associated to each of the minima defined. It is easy to verify that all points are distinct and moreover, they all lie on different portions of the "edge" of the Capture Set.

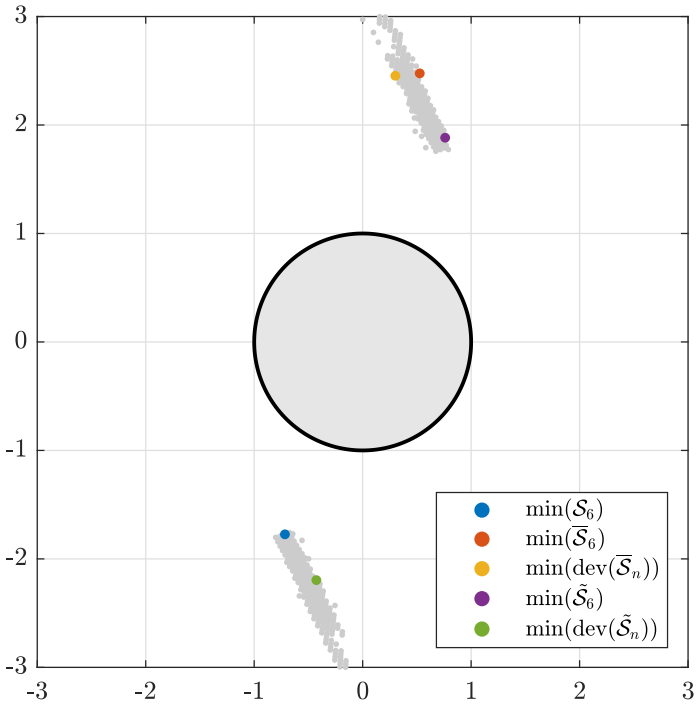

Figure B.1: Minima associated to different indices.

However, upon visual inspection it was verified that the initial conditions associated to the minima of the new indices do not exhibit a regular trajectories. Such behaviour is the reason behind $\mathcal{S}$ being used to define the region of interest.

B.2 Fixed-fixed approximation

The current section reports the results obtained by applying the technique described in Section 4.3.1 to the limit case of $\delta t_0 = 0.5$ days considering the left extreme. As done in Section 5.1.1 the results show the representation of the state vector (Figure B.2), the approximation error (Figure B.3) and the trajectories in EME2000 (Figure B.4) and RPF (Figure B.5) reference frames. By considering Figures B.4 and B.5 it is evident that although the error reported in Figure B.3 is significantly larger, the trajectory is approximated with discrete accuracy.

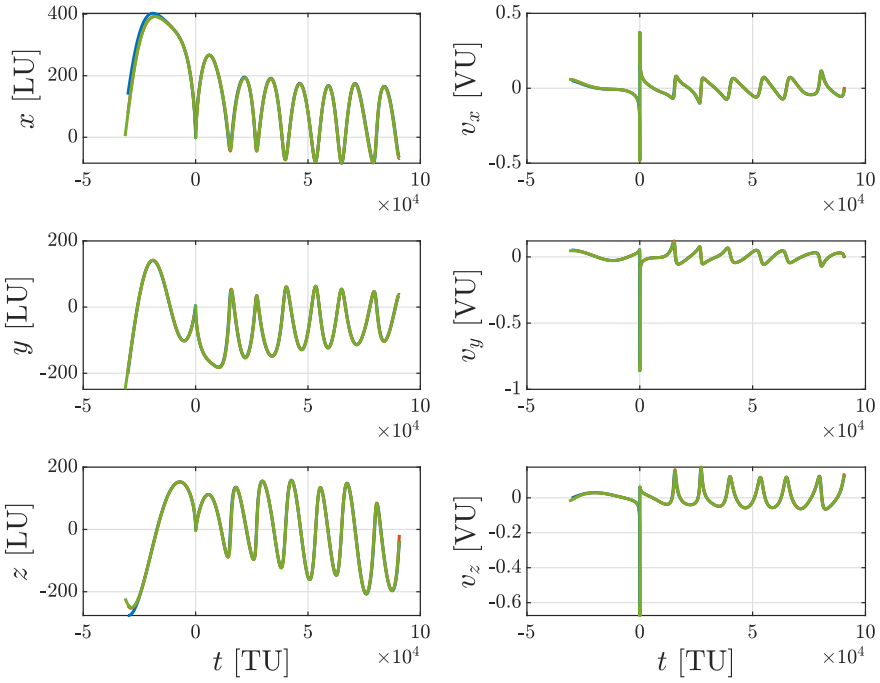

Figure B.2: State vectors for $\varphi_{t_0}^t$ (blue), $\varphi_{t_0+\delta t_0}^t$ (green), and $\tilde{\varphi}_{t_0+\delta t_0}^t$ (orange) for $\delta t_0 = 0.5$ days.

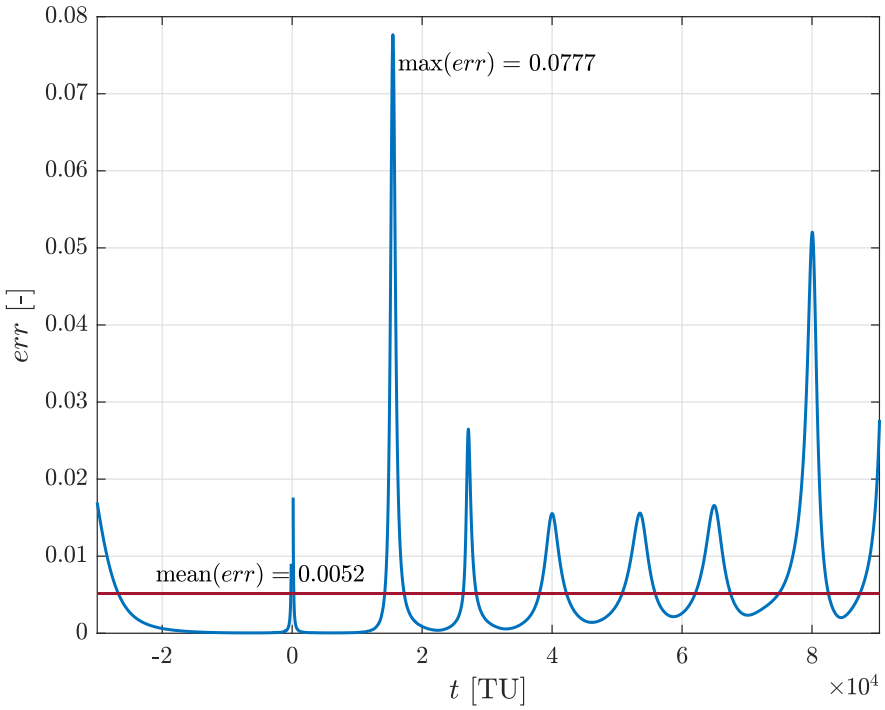

Figure B.3: L^2-norm and mean value of the approximation error for $\delta t_0 = 0.5$ days.

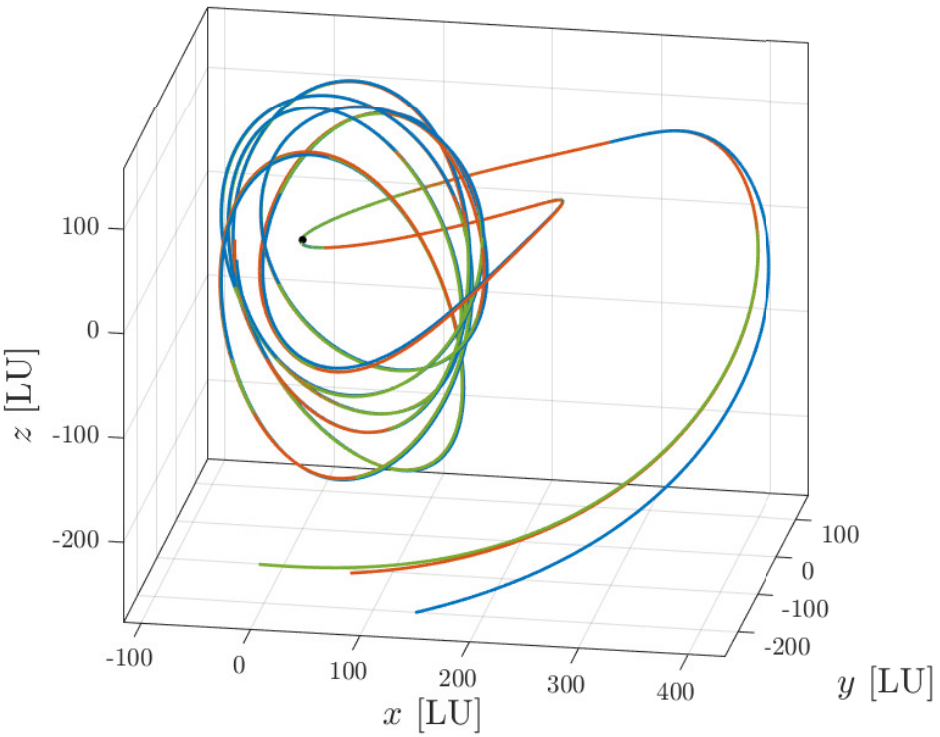

Figure B.4: Trajectories in EME2000 for $\varphi^t_{t_0}$ (blue), $\varphi^t_{t_0+\delta t_0}$ (green), and $\tilde{\varphi}^t_{t_0+\delta t_0}$ (orange) for $\delta t_0 = 0.5$ days.

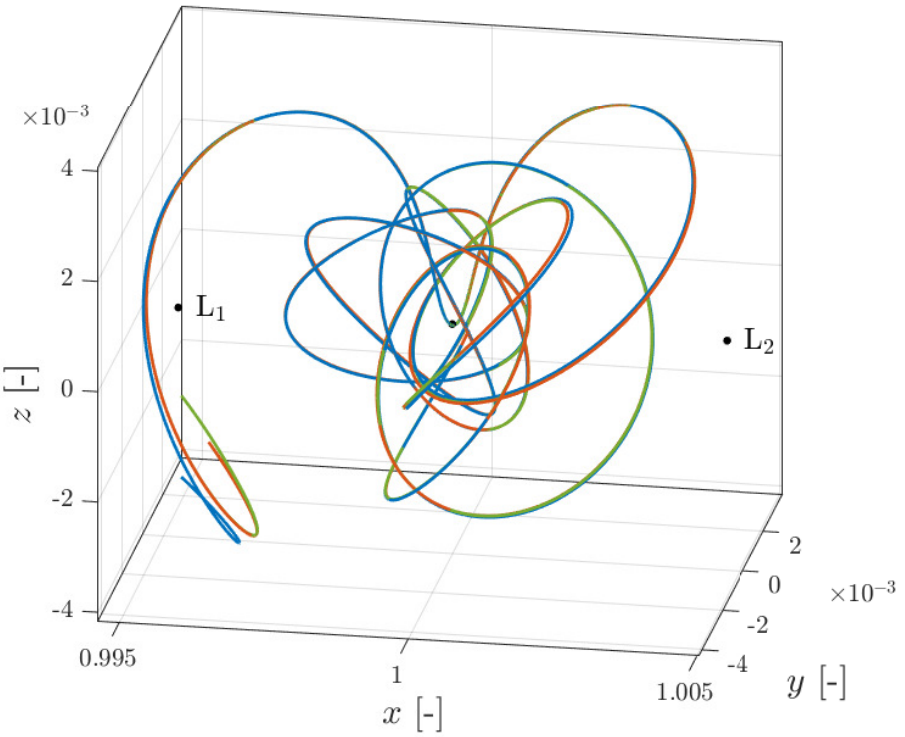

Figure B.5: Trajectories in RPF for $\varphi^t_{t_0}$ (blue), $\varphi^t_{t_0+\delta t_0}$ (green), and $\tilde{\varphi}^t_{t_0+\delta t_0}$ (orange) for $\delta t_0 = 0.5$ days.

B.3 Fixed-varying approximation

The current section reports the results obtained by applying the technique described in Section 4.3.2 to the limit case of $\delta t_0 = 0.5$ day as built from the left extreme of the time interval. As done in Section 5.2.1 the results show the representation of the state vector (Figure B.6), the approximation error (Figure B.7) and the trajectories in EME2000 (Figure B.8) and RPF (Figure B.9) reference frames. By considering Figures B.4 and B.5 it is evident that although the error reported in Figure B.3 is significantly larger, the trajectory is approximated with discrete accuracy due to the average error being limited.

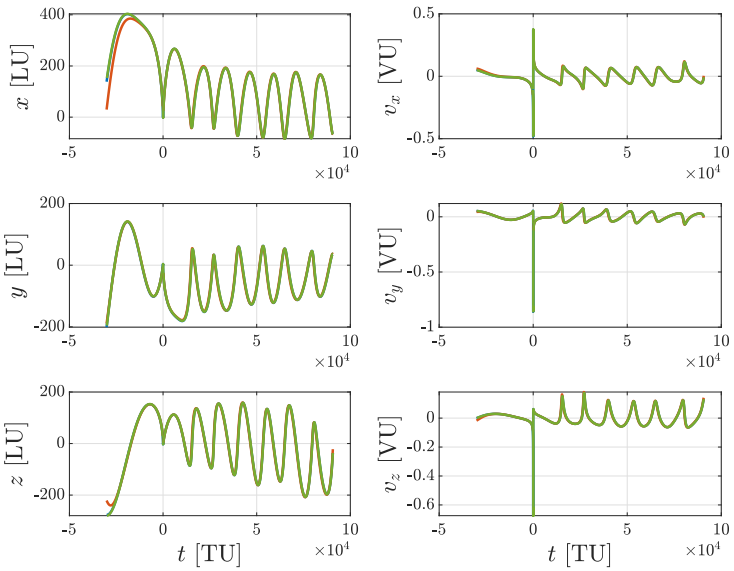

Figure B.6: State vectors for $\varphi^t_{t_0}$ (blue), $\varphi^t_{t_0+\delta t_0}$ (green), and $\tilde{\varphi}^t_{t_0+\delta t_0}$ (orange) for $\delta t_0 = 0.5$ days.

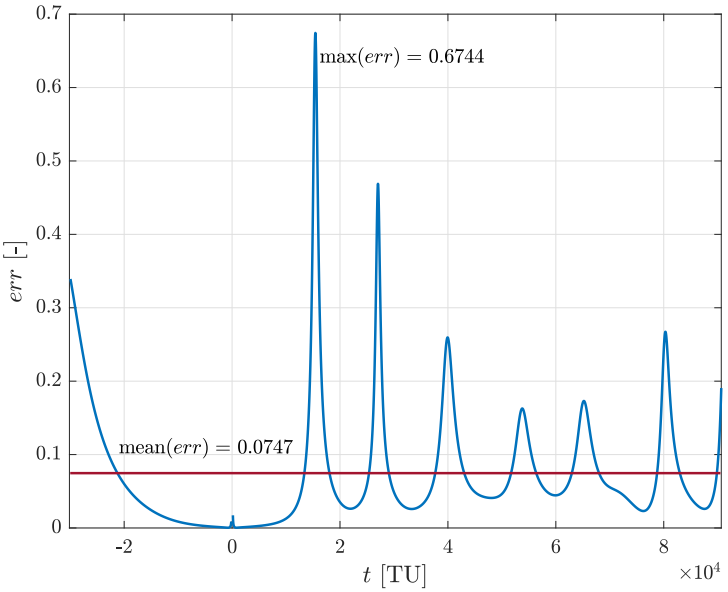

Figure B.7: L^2-norm and mean value of the approximation error for $\delta t_0 = 0.5$ days.

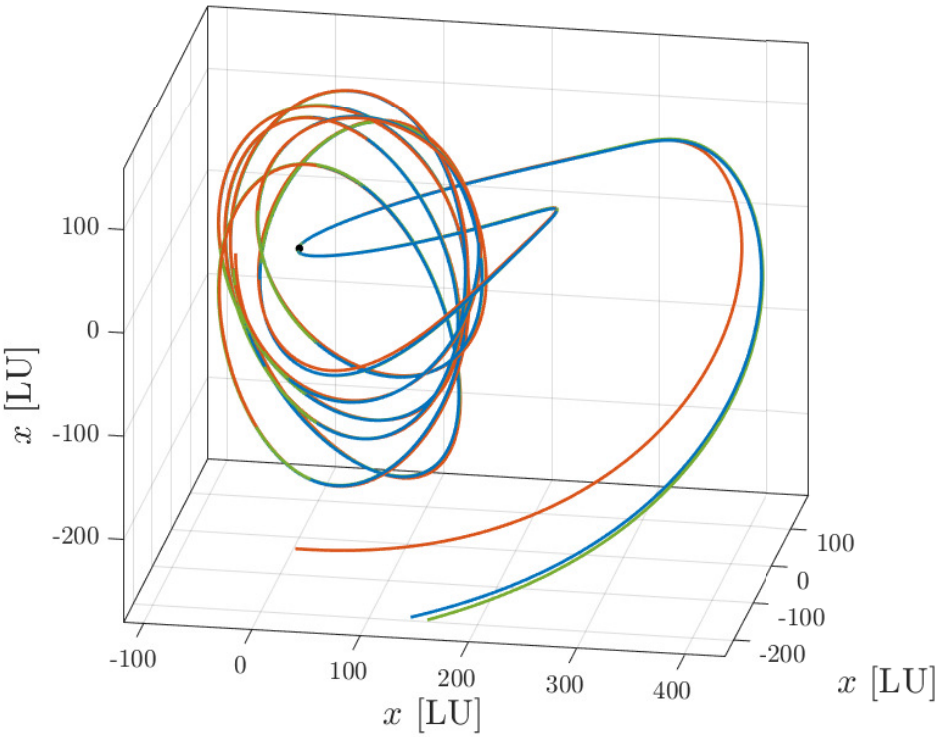

Figure B.8: Trajectories in EME2000 for $\varphi_{t_0}^t$ (blue), $\varphi_{t_0+\delta t_0}^t$ (green), and $\tilde{\varphi}_{t_0+\delta t_0}^t$ (orange) for $\delta t_0 = 0.5$ days.

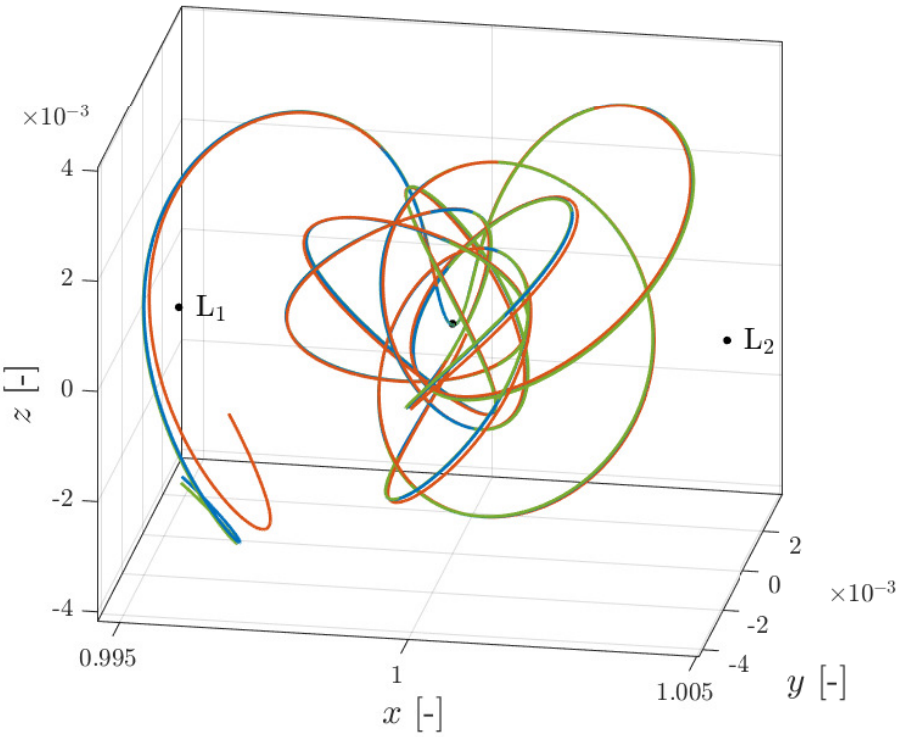

Figure B.9: Trajectories in RPF for $\varphi_{t_0}^t$ (blue), $\varphi_{t_0+\delta t_0}^t$ (green), and $\tilde{\varphi}_{t_0+\delta t_0}^t$ (orange) for $\delta t_0 = 0.5$ days.

B.4 Varying-varying approximation

The current section reports the extended results of the algorithm propagating the region both in space and time, shown in Figure B.10.

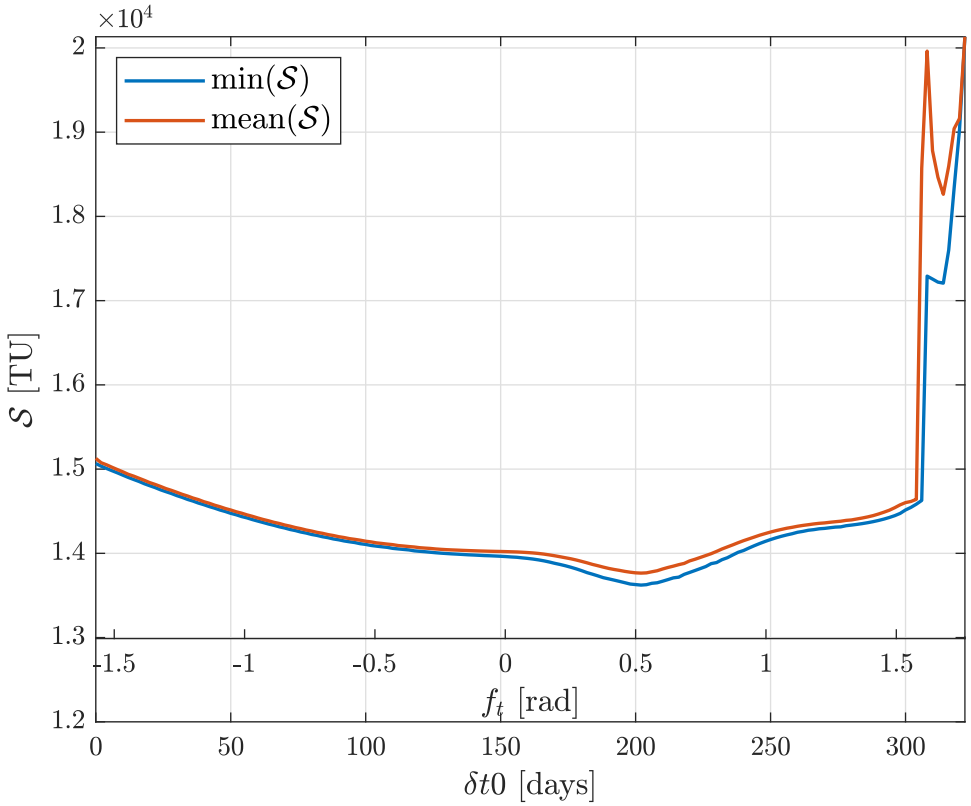

Figure B.10: Complete representation of minimum and average Stability Index.

It is worth mentioning that the values of $\mathcal{S}$ computed in the time interval [304, 322] days are erratic due to the region containing few highly unstable capture trajectories, as can be seen in Figure B.11. In fact, the algorithm stopped at $\delta t_0 = 324$ days because of the verification of the first criterion listed in Section 4.3.

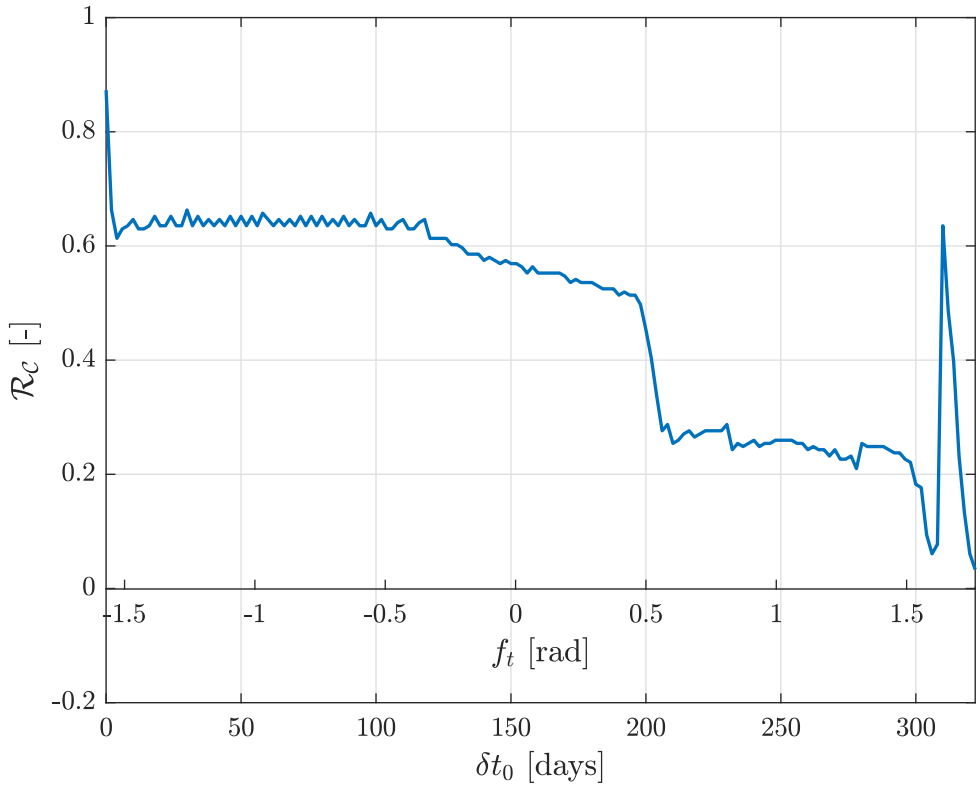

Figure B.11: Evolution in time of the Capture Ratio $\mathcal{R}_\mathcal{C}$ within the region.

This section also reports the results obtained by applying the technique described in Section 4.3.3 to the limit case of $\delta t_0 = 0.5$ day considering the left extreme. As done in Section 5.3.1 the results show the representation of the state vector (Figure B.12), the approximation error (Figure B.13) and the trajectories in EME2000 (Figure B.14) and RPF (Figure B.15) reference frames. By considering Figures B.14 and B.15 it is evident that although the error reported in Figure B.13 is significantly larger, the trajectory is approximated with discrete accuracy.

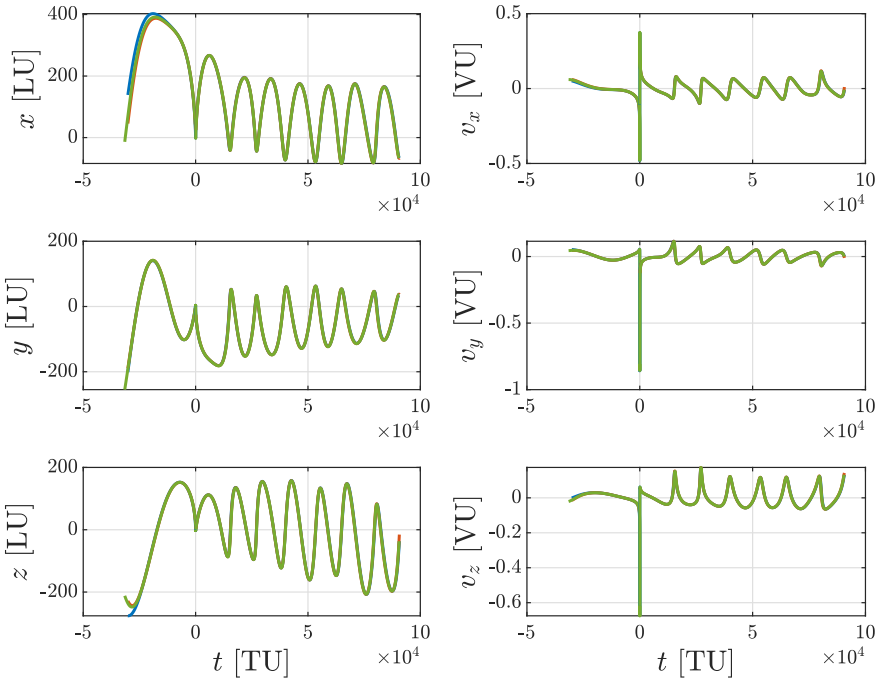

Figure B.12: State vectors for $\varphi^t_{t_0}$ (blue), $\varphi^t_{t_0+\delta t_0}$ (green), and $\tilde{\varphi}^t_{t_0+\delta t_0}$ (orange) for $\delta t_0 = 0.5$ days.

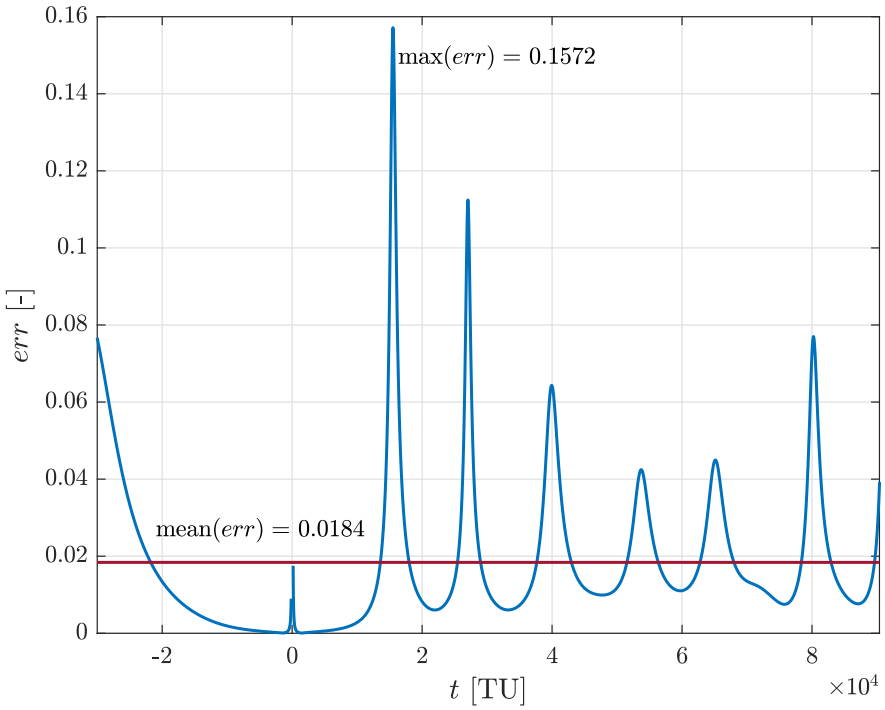

Figure B.13: L^2-norm and mean value of the approximation error for $\delta t_0 = 0.5$ days.

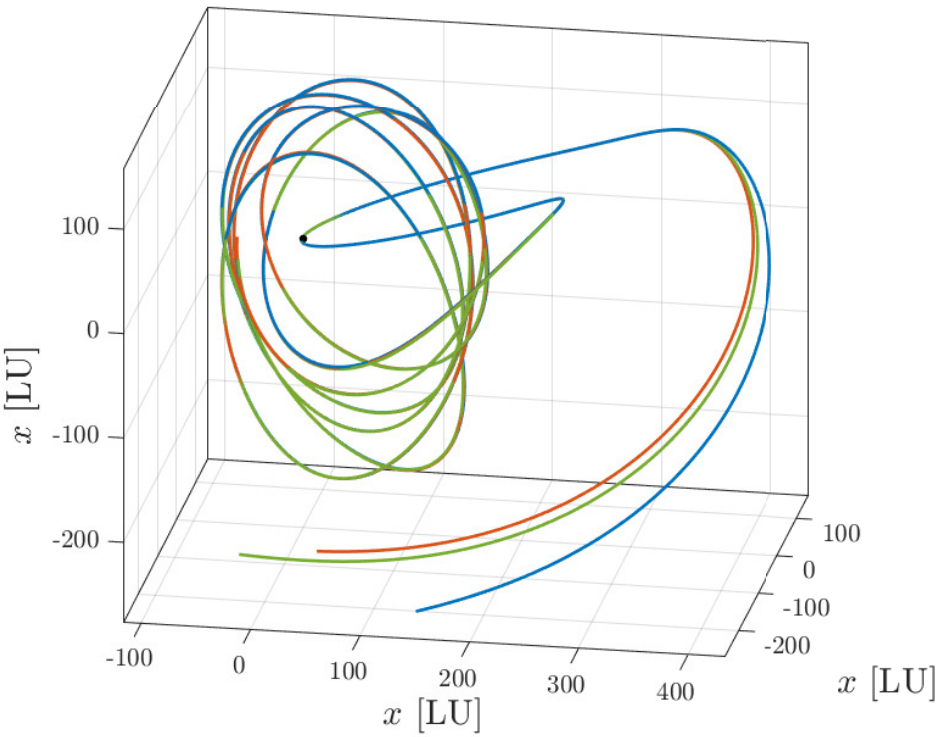

Figure B.14: Trajectories in EME2000 for $\varphi^t_{t_0}$ (blue), $\varphi^t_{t_0+\delta t_0}$ (green), and $\tilde{\varphi}^t_{t_0+\delta t_0}$ (orange) for $\delta t_0 = 0.5$ days.

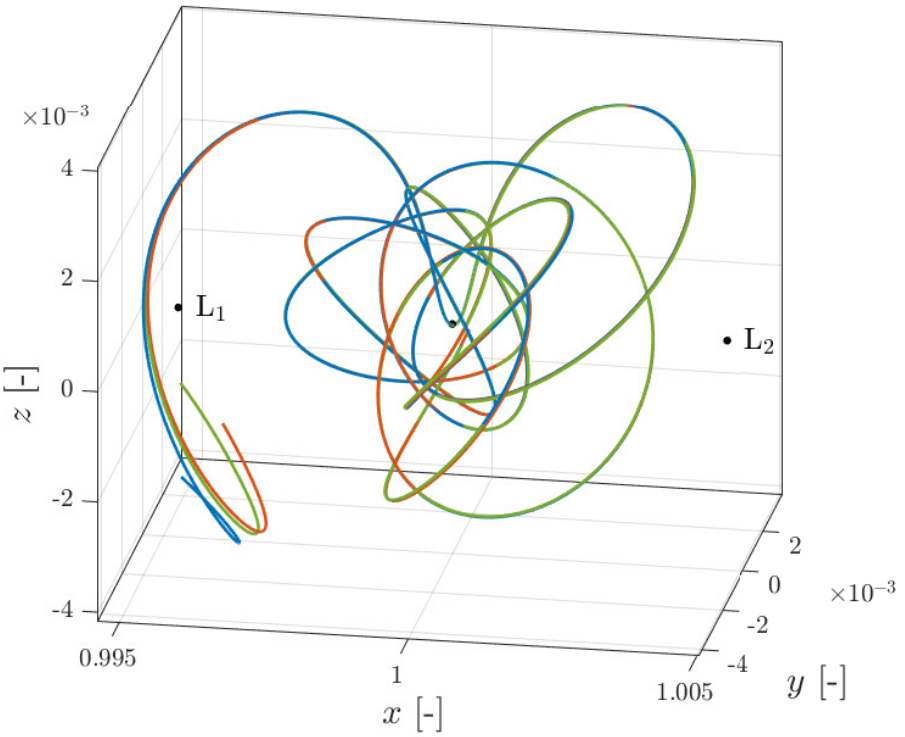

Figure B.15: Trajectories in RPF for $\varphi^t_{t_0}$ (blue), $\varphi^t_{t_0+\delta t_0}$ (green), and $\tilde{\varphi}^t_{t_0+\delta t_0}$ (orange) for $\delta t_0 = 0.5$ days.

Bibliography

[1] C. Acton, N. Bachman, B. Semenov, and E. Wright. "A look towards the future in the handling of space science mission geometry". In: *Planetary and Space Science* 150 (2018), pp. 9–12. DOI: 10.1016/j.pss.2017.02.013.

[2] C. H. Acton Jr. "Ancillary data services of NASA's navigation and ancillary information facility". In: *Planetary and Space Science* 44.1 (1996), pp. 65–70.

[3] G. Aguiar, F. Topputo, et al. "A Technique for Designing Earth-Mars Low-Thrust Transfers Culminating in Ballistic Capture". In: *7th International Conference on Astrodynamics Tools and Techniques (ICATT)*. 2018.

[4] B. A. Archinal, M. F. A'Hearn, E. Bowell, A. Conrad, G. J. Consolmagno, et al. "Report of the IAU working group on cartographic coordinates and rotational elements: 2009". In: *Celestial Mechanics and Dynamical Astronomy* 109.2 (2011), pp. 101–135. DOI: 10.1007/s10569-010-9320-4.

[5] R. H. Battin. *An introduction to the mathematics and methods of astrodynamics*. Aiaa, 1999, pp. 388–390.

[6] E. Belbruno. *Fly me to the moon: an insider's guide to the new science of space travel*. Princeton University Press, 2007.

[7] E. Belbruno, M. Gidea, and F. Topputo. "Weak stability boundary and invariant manifolds". In: *SIAM Journal on Applied Dynamical Systems* 9.3 (2010), pp. 1061–1089. DOI: 10.1137/090780638.

[8] E. Belbruno, F. Topputo, and M. Gidea. "Resonance transitions associated to weak capture in the restricted three-body problem". In: *Advances in Space Research* 42.8 (2008), pp. 1330–1351. DOI: 10.1016/j.asr.2008.01.018.

[9] G. Cruz Chambel de Aguiar. "Earth–Mars low-thrust transfers with ballistic capture and real-Solar-System dynamics". In: *M.Sc. Thesis* at Delft University of Technology (2017).

[10] D. A. Dei Tos, R. P. Russell, and F. Topputo. "Survey of Mars ballistic capture trajectories using periodic orbits as generating mechanisms". In: *Journal of Guidance, Control, and Dynamics* 41.6 (2018), pp. 1227–1242. DOI: 10.2514/1.G003158.

[11] D. A. Dei Tos and F. Topputo. "High-fidelity trajectory optimization with application to saddle-point transfers". In: *Journal of Guidance, Control, and Dynamics* 42.6 (2019), pp. 1343–1352. DOI: 10.2514/1.G003838.

[12] M. Farazmand and G. Haller. "Computing Lagrangian coherent structures from their variational theory". In: *Chaos: An Interdisciplinary Journal of Nonlinear Science* 22.1 (2012). DOI: 10.1063/1.3690153.

[13] F. García and G. Gómez. "A note on weak stability boundaries". In: *Celestial Mechanics and Dynamical Astronomy* 97.2 (2007), pp. 87–100. DOI: 10.1007/s10569-006-9053-6.

[14] N. Hyeraci and F. Topputo. "Method to design ballistic capture in the elliptic restricted three-body problem". In: *Journal of guidance, control, and dynamics* 33.6 (2010), pp. 1814–1823. DOI: 10.2514/1.49263.

[15] R. Jehn, S. Campagnola, D. Garcia, and S. Kemble. "Low-thrust approach and gravitational capture at Mercury". In: *18th International Symposium on Space Flight Dynamics*. Vol. 548. 2004, p. 487.

[16] W. S. Koon, M. W. Lo, J. E. Marsden, and S. D. Ross. "Low energy transfer to the Moon". In: *Celestial Mechanics and Dynamical Astronomy* 81.1 (2001), pp. 63–73. DOI: 10.1023/A:1013359120468.

[17] Z.-F. Luo and F. Topputo. "Analysis of ballistic capture in Sun–planet models". In: *Advances in Space Research* 56.6 (2015), pp. 1030–1041. DOI: 10.1016/j.asr.2015.05.042.

[18] Z.-F. Luo and F. Topputo. "Capability of satellite-aided ballistic capture". In: *Communications in Nonlinear Science and Numerical Simulation* 48 (2017), pp. 211–223. DOI: 10.1016/j.cnsns.2016.12.021.

[19] Z.-F. Luo and F. Topputo. "Mars orbit insertion via ballistic capture and aerobraking". In: *Astrodynamics* (2021), pp. 1–15. DOI: 10.1007/s42064-020-0095-4.

[20] Z.-F. Luo, F. Topputo, F. Bernelli-Zazzera, and G.-J. Tang. "Constructing ballistic capture orbits in the real Solar System model". In: *Celestial Mechanics and Dynamical Astronomy* 120.4 (2014), pp. 433–450. DOI: 10.1007/s10569-014-9580-5.

[21] M. Manzi. "A flow-informed strategy for ballistic capture trajectory design". In: *M.Sc. Thesis* at Delft University of Technology (2019).

[22] O. Montenbruck, E. Gill, and F. Lutze. *Satellite Orbits: Models, Methods, and Applications*. Vol. 55. 2. 2002. DOI: 10.1115/1.1451162.

[23] A. Parkash. "Application of Lagrangian Coherent Structures to the computation and understanding of ballistic capture trajectories". In: *M.Sc. Thesis* at Delft University of Technology (2019).

[24] J. Parker. "Establishing a network of lunar landers via low-energy transfers". In: *24th AAS/AIAA Space Flight Mechanics Meeting, Santa Fe, New Mexico*. 2014, pp. 26–30.

[25] D. Romagnoli and C. Circi. "Earth–Moon weak stability boundaries in the restricted three and four body problem". In: *Celestial Mechanics and Dynamical Astronomy* 103.1 (2009), pp. 79–103. DOI: 10.1007/s10569-008-9169-y.

[26] S. C. Shadden, F. Lekien, and J. E. Marsden. "Definition and properties of Lagrangian coherent structures from finite-time Lyapunov exponents in two-dimensional aperiodic flows". In: *Physica D: Nonlinear Phenomena* 212.3-4 (2005), pp. 271–304. DOI: 10.1016/j.physd.2005.10.007.

[27] C. Short, K. Howell, and X. Tricoche. "Lagrangian coherent structures in the restricted three-body problem". In: *Proceedings of 21st AAS/AIAA Space Flight Mechanics Meeting, New Orleans, Louisiana, Paper No. AAS*. 2011, pp. 11–250.

[28] C. R. Short. "Flow-informed strategies for trajectory design and analysis". In: *Ph.D. Thesis* at Purdue University (2016).

[29] F. Topputo and E. Belbruno. "Computation of weak stability boundaries: Sun–Jupiter system". In: *Celestial Mechanics and Dynamical Astronomy* 105.1 (2009), pp. 3–17. DOI: 10.1007/s10569-009-9222-5.

[30] F. Topputo, E. Belbruno, and M. Gidea. "Resonant motion, ballistic escape, and their applications in astrodynamics". In: *Advances in Space Research* 42.8 (2008), pp. 1318–1329. DOI: 10.1016/j.asr.2008.01.017.

[31] M. Vergaaij and J. Heiligers. "Time-optimal solar sail heteroclinic-like connections for an Earth-Mars cycler". In: *Acta Astronautica* 152 (2018), pp. 474–485. DOI: 10.1016/j.actaastro.2018.08.008.